Enabling Tools for Biological Analysis: Technologies for the Study of Protein Dynamics, Detection and Interaction

by

Moshiur Mekhail Anwar

B.A. Physics, University of California at Berkeley (1998)
M.S. EECS, University of California at Berkeley (2001)

Submitted to the Department of Electrical Engineering and Computer Science
in partial fulfillment of the requirements for the degree of

Ph.D. in Computer Science and Engineering

at the

MASSACHUSETTS INSTITUTE OF TECHNOLOGY

September 2007

Author . . . .
Department of Electrical Engineering and Computer Science
August 31, 2007

Certified by. . . . .
Paul Matsudaira
Professor
Thesis Supervisor

Accepted by . . . .
Arthur C. Smith
Chairman, Department Committee on Graduate Students

Table of Contents

Table of Figures

Acknowledgements

First and foremost, I'd like to thank my advisor, Prof. Matsudaira, for his continuous support and guidance. My thesis committee (and their groups) has given me valued advice, and I'd like to express my gratitude to Prof. Freeman and Prof. Sarpeshkar for their help and advice. Prof. Boser, at UC Berkeley, has enabled me to complete this project with support both in terms of advice, encouragement, and by facilitating the fabrication of the chips via National Semiconductor.

I'd like to thank the members of the Matsudaira lab. In particular, Lera, Yelena, and Guichy have been very helpful with my experiments in molecular biology and biochemistry. Winston, Mike and Barney have given helpful suggestions, and I appreciate their support.

I'd also like to especially thank my parents who have made this all possible, with their unrelenting support. I dedicate this thesis to them.

To my sister and friends, especially Tony, Nilim, Erich and Jackie, I thank you for always being there.

Abstract

The study of proteins in biological systems requires a comprehensive approach: investigating dynamics, interaction and identification. This thesis will examine several technological approaches we have developed to address these needs. To enable the study of the dynamics of biological systems, we have developed a method for using atomic force microscopy (AFM) to image motion on an angstrom scale with microsecond time resolution. As proteins move, diffuse, or are actively trafficked within the cellular environment, they interact with other biological molecules. Protein microarrays offer a high-throughput method of investigating these protein interactions, but their use has largely been hindered by the need to clone and purify thousands of proteins. We have developed a novel technique to pattern proteome-scale microarrays using a cellular lysate, whereby all relevant proteins are synthesized with the correct post-translational modifications. Additionally, we have integrated the identification of proteins with quantitative mass spectrometry (SILAC). Using these arrays we have probed changes in the phosphorylation state of cells in response to activation of the Erb1 and Erb2 receptors. Using our microarray platform we were able to further probe the phosphoproteome for proteins that have multiple post-translational modifications. The widespread use of protein, DNA and small molecule microarrays has been limited in clinical and diagnostic settings due to the cost of microarray readers. Therefore, we have developed an optics-free integrated circuit-based microarray imaging chip that is compatible with existing (optics-based) microarray protocols. By eliminating optics, and developing the reader using integrated circuit technology, the cost can be significantly reduced. The reader is powered by a single sine wave, enabling a wireless interface. We use this reader to detect a biotin-streptavidin interaction using standard microarray procedures.

Thesis Supervisor: Paul Matsudaira

Title: Professor, Department of Biology and Biological Engineering

Introduction

Proteins and small molecules are the effectors of physiologic action, and their function is regulated far beyond what can be solely described by gene expression. Proteins can affect their environment by exhibiting movement, interacting with other proteins, small molecules, and DNA and changing function in response to post-translational modifications. This makes it crucial to have a global understanding of which proteins are active, and how they function, interact and affect their environment. This thesis develops tools and techniques that enable novel analysis of protein dynamics, detection and interaction.

We begin at the protein level, and introduce a method to image biological motion. Proteins size is on the order of nanometers, with movement on the order of angstroms. We have developed a novel technique using atomic force microscopy to image motion with angstrom level spatial resolution, and microsecond time resolution. We then move to analyze how these proteins interact with each other, specifically via μarray analysis. We introduce a novel technique of patterning a protein μarray, and integrate this with quantitative mass spectrometry. The wide spread use of these techniques is often limited by the access to instrumentation. We introduce a platform for optical detection, which can be coupled with both microarray detection as well as *in-vivo* sensors.

In Appendix 1: Microsecond Time-resolved Atomic Force Sensing Mapping, we use Atomic Force Microscopy to image motion on the angstrom scale. Typically used for static images, AFM can achieve angstrom resolution in the Z dimension, and at least nanometer resolution in the lateral direction. The contribution of this work is extending the ability of the AFM to gather time-resolved images while retaining its spatial resolution. We accomplished this by implementing a stroboscopic method and looking at periodic motion. We demonstrated this on a microfabricated oscillation grid. This work was done in conjunction with Prof. Itay Rousso (Weizmann), and portions have been previously published (Rousso 2005).

In Chapter 1: Patterning Proteome-Scale μArrays, turn our focus to high-throughput methods of assaying protein-protein interactions. We developed a novel method of patterning and analyzing protein microarrays. Traditionally, the use of protein microarrays has been restricted by the need to purify thousands of individual proteins. We developed a μarray stamping technique allowing for proteins to be stamped and also subjected to biochemical analysis. The technique leverages both the strengths of microarrays as well as of mass spectrometry.

In Chapter 2: Protein μ-Stamping: Analyzing Changes in the Hela Phosphoproteome in Response to Epidermal Growth Factor, we demonstrate the utility of this technique by looking at changes in the phosphoproteome of Hela cells in response to Epidermal Growth Factor (EGF). Additionally, by patterning the proteins in a μarray format, we are able to screen the interaction of several molecules against the proteome. In this example, we looked at additional post-translational modifications, Ubiquitin and ISG.

In Chapter 3: Protein µ-Stamping: Quantifying Changes in the Phosphoproteome in Breast Cancer Epithelial Cells in Response to Heregulin, we integrate the protein µstamping technique with quantitative mass spectrometry. Using the protein µstamping technique we are able to pattern the phosphoproteome, and visualize changes both in the phosphoproteome as well as additional post-translational modifications. By growing the cells in SILAC media, we are able to quantify the differential protein expression via mass spectrometry.

In order to expand the use of protein and small molecule µarrays, we develop a CMOS-based optical reader in which no lenses or optical filters are required. By significantly reducing the cost of µarray readers, applications such as diagnostics and screening can be more ubiquitous. In Chapter 4: Design and Testing of a CMOS µArray Reader we detail the design and testing of an optical array imager. The imager is powered by a single sine wave, making it applicable for wireless applications. In Chapter 5: An Optics-Free CMOS µArray Reader we demonstrate the utility of the array reader in reading a prototype protein µarray. In Chapter 6: Wireless Interface, we demonstrate the ability to power and receive data wireless from the sensor using an external antenna.

Chapter 1: Patterning Proteome-Scale µArrays

Abstract: Systems-level analysis of biological organisms requires a comprehensive method of high throughput analysis from the start of the information pathway (i.e. DNA) to the effectors of physiological action (i.e. protein and small molecules). DNA µarrays have been well developed and characterized, but protein and small molecule arrays have not been widely implemented. Protein microarrays offer an optimal medium with which to probe changes in a system by simultaneously looking at thousands of protein changes, interactions, and modifications in a high throughput format. Unfortunately, the use of protein µarrays has been limited by the difficulty in synthesizing tens of thousands of individual proteins. This chapter presents a novel technique for patterning a proteome-scale µarray using a cellular lysate. Unlike traditional protein arrays, where proteins must be purified, we utilize a cellular lysate where all relevant proteins are pre-synthesized. This obviates the need for synthesis and purification of proteins, while encompassing all of the potential binding targets for the ligand(s) in question. We accomplish this by separating proteins on an SDS-PAGE gel, and diffusively transferring a minute amount of protein onto a microarray substrate, leaving the vast majority of the protein in the gel, for further analysis. The protein binding assay is performed on the patterned µarray, and the corresponding spatial position on the gel is extracted from the gel and identified via mass spectrometry. We have demonstrated this technique by

identifying a single protein within a cellular lysate. In the subsequent chapters, we expand upon this technique to look a the state changes of cells simulated with EGF and Heregulin by looking at changes in the phosphoproteome, as well as due to post-translational modifications by Ubiquitin and ISG. This technique can be used for rapid screening and identification of protein classes, binding partners and post-translational modifications.

Background:

µArrays offer a high throughput method of analyzing large numbers of samples, in a rapid-high throughput fashion, with minimal reagents. This makes them an ideal platform for obtaining a global view of complex biological systems. making them ideal for assaying entire complex biological systems. DNA µarrays are the most ubiquitous application of this technology, are widely used in research, clinical and industrial applications. Despite the extensive information they provide, the effectors of physiological action are proteins and small molecules. DNA µArrays are limited to determining gene expression data, but unfortunately, this is not always reflective of protein expression (S. P. Gygi 1999). Furthermore, post-translational modifications can be crucial to protein function. Protein and small molecule arrays offer a more direct method to elucidate the physiological changes in a biological system than DNA alone.

There are two general types of protein arrays: identification arrays and interaction arrays. Identification arrays seek to determine the contents of a complex sample, and are analogous to DNA µArrays. They function by patterning proteins (typically antibodies) that bind to specific (known) targets. A sample containing a mixture of proteins is introduced to the array, and by identifying the spots to which the sample binds, the identity of the components can be determined. Additionally, multiple samples can be labeled with spectrally distinct fluorophores and hybridized to the same array, allowing comparison of relative differences.

Interaction arrays are geared towards determining the binding partners for a specific protein or small molecule. They are developed by patterning known proteins on the array, and seeing which of those the target protein bind to. The focus of this method is the fabrication of interaction arrays. Understanding a protein's binding partners and interactions gives vital insight into protein pathways, as well as facilitates identifying binding targets for drug discovery.

Immunoprecipitation represents the traditional method to identify a target's binding partners, as associations can be done within cells or in a lysate under native conditions. There are several methods of analyzing the components obtained by immunoprecipitation, and the choice depends upon the information one is seeking. When looking for the presence of a specific target, western blotting (Scofield 2006) can be used. The limitation of this technique is that one cannot discover unknown associations. When taking a shotgun approach to determining protein associations, mass spectrometry can be used to identify the contents of the immunoprecipitate. Although an effective tool, the sensitivity of a mass- spectrometer decreases when analyzing complex samples, making it advantageous to assay a fractionated or isolated sample. Therefore, a method is needed to identify and isolate the key components of an immunoprecipitate to be analyzed. A μarray-based platform would enable a high throughput method of isolating the protein interactions of interest.

Protein μarrays are created by synthesizing and purifying proteins, and then spotting them on a substrate. The substrate is typically a chemically modified slide enabling attachment through either electrostatic interactions (polylysine, nitrocellulose, aminosilane) or covalent chemistry (aldehyde). There have been several efforts directed towards synthesizing and patterning the proteome. MacBeath et al (Schreiber 2000) generated a large scale protein microarray by printing proteins in a predetermined location on the array, similar to construction of DNA microarrays. Zhu et al (H. Zhu 2001) expressed and purified 5800 yeast proteins to identify what proteins bound to a specific target.

To eliminate the need for synthesizing and patterning proteins, a cellular lysate can be used. A cellular lysate is an ideal choice because it represents all relevant proteins to the system, already synthesized and with the proper post-translational modifications. Far-westerns and immunoprecipitation take advantage of this fact by binding the target to proteins within a cellular lysate on either a substrate or solution, respectively. Both of these methods lack the advantages of microarrays: being able to visualize results in a high-throughput fashion, the use of multiple samples for differential analysis, and the use of minimal reagent volumes. In the case of far-westerns, it is difficult to identify the proteins that are bound as the protein is attached to a membrane. With immunoprecipitation, the identity of the proteins that bind to a target can be determined via mass spectrometry, but further analysis in an array or substrate-based platform cannot be accomplished.

This chapter describes a novel method of patterning protein microarrays using a cellular lysate that retains the advantages of µarrays while preserving the versatility of biochemical assays.

Experimental

To address the difficulties of patterning protein microarrays, we introduce a novel technique of protein stamping that combines the advantages of microarray technology (small, multiple samples) with the utility of mass spectrometry to identify novel proteins, enabling high-throughput screening on a proteome-wide scale. We utilize a cellular lysate, which encompasses the entire proteome of interest. The array is patterned by separating the proteins by size via standard gel electrophoresis, and then allowing the proteins to diffusively transfer to a chemically functionalized (aminosilane) microarray slide. This results in a patterned microarray slide. A similar approach has been used to transfer proteins to nitrocellulose for a standard western assay (Scofield 1997). Our technique transfers protein to a glass (insulating) substrate, and so standard methods of fluid flow (wicking) or current flow (electrophoresis) do not apply. We have characterized the transfer technique and show that it is diffusion based, and illustrate the effects of transfer time and concentration on sensitivity. A key advantage of this technique is that the vast majority of the protein is remains in the gel, and therefore can be subjected to analysis by mass spectrometry (or to pattern additional arrays). By using a 1D gel, the technique is kept simple and rapid, but the method can be easily extended to a 2D gel.

Theory and Mechanism of Transfer

Unlike a western blot, where proteins are moved by an electric field coupled with a current, protein µstamping relies on diffusive transfer. In a Western blot, an electric field is applied to the gel, with the electrodes in contact with the buffer. The electric field causes both the ions in solution and the negatively charged proteins to move towards the electrodes. The movement of the ions, and the subsequent oxidation/reduction at the respective electrodes, causes a current to flow, maintaining the electric field. The proteins move toward the positive electrode and are trapped in the nitrocellulose or PVDF membrane. Typically, all of the proteins in the gel are transferred to the membrane.

In transferring protein from a gel to a glass slide, current does not flow through the glass slide because it is an insulator. Unlike the situation in a standard Western blot, when the electric field acts on the ions and moves them to the electrodes, ions in µstamping are not oxidized or reduced because they do not come in contact with the electrodes. In contrast, they accumulate near the edges of the gel, screening the electric field. Consequently, no electric field is maintained in the gel, and the proteins can only move via diffusion.

This principle is illustrated in Figure 1, where a lysate is run on an SDS gel and then diffusively transferred to a functionalized slide. The gel is placed on a glass slide, and an electric field is applied. The electric field creates a charge depletion region (with high electric field), but it only extends on the order of the Debye length (< 1 nm) into the gel. Therefore, no protein is subject to the electric field, and the transfer shall be dependent solely on diffusion and independent of applied electric field.

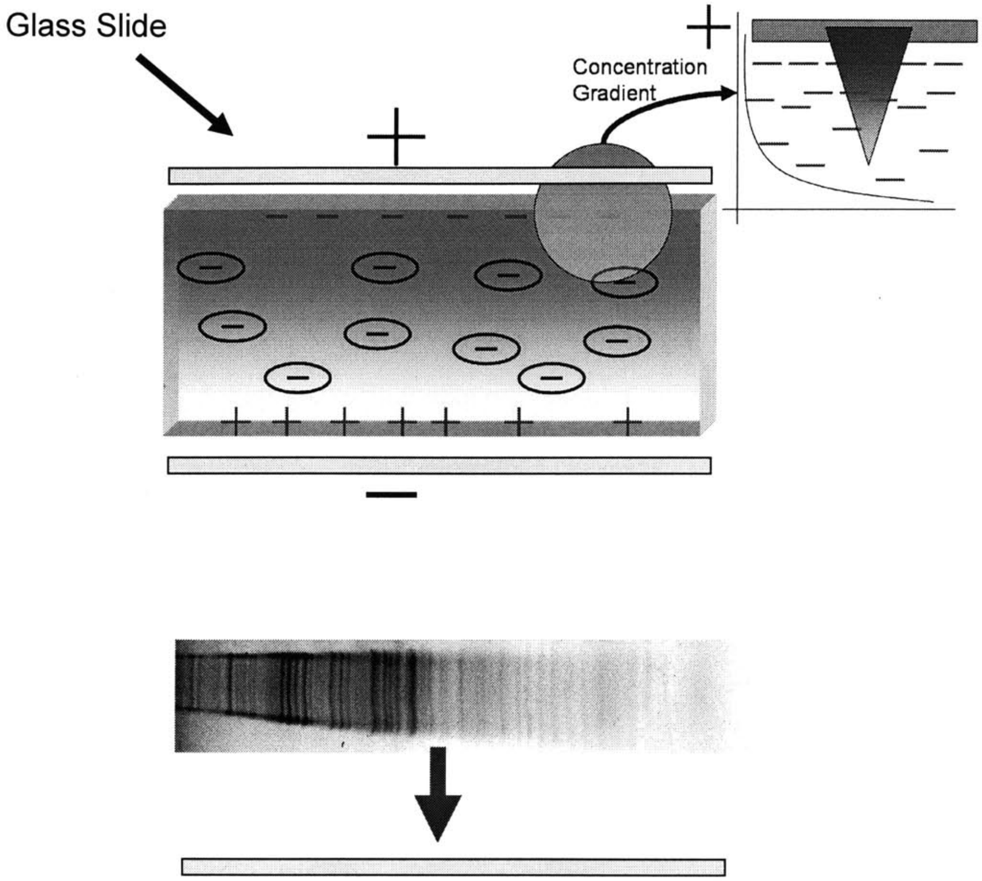

Figure 1

A cellular lysate is separated via standard gel electrophoresis. The gel is placed on a functionalized glass slide, and proteins are allowed to diffuse onto the slide. An applied electric field will generate a screening charge-sheet of ions, with the electric field penetrating on the order of the Debye length, which is < 1 nm. Therefore, there is no electric field in the gel, and proteins travel solely by diffusion.

To demonstrate this technique, we ran a Biorad blue ladder on a Biorad 10% SDS PAGE gel. We then transferred for 2 hours, and scanned both the gel (Typhoon) and the slide (Axon). The results are shown in Figure 2. There is an exact correspondence between the gel and slide. Furthermore, the gel is scanned after the transfer, showing that nearly all of the protein remains in the gel.

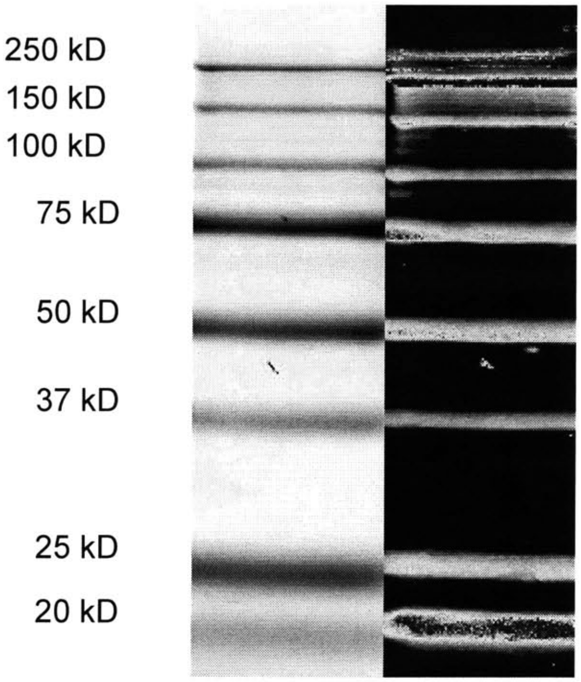

Figure 2: Fluorescent Ladder Transfer

A BioRad Blue protein ladder was run on a 10% SDS acrylamide gel and diffusively transferred to an aminosilane slide. The slide was scanned with the Axon 4000B microarray scanner, and the gel was scanned with the Typhoon fluorescent scanner after transfer. There is a direct spatial correspondence between the protein in the gel and the slide. Furthermore, the vast majority of the protein remains in the gel.

From the lack of electric field (and resulting current flow), we expect only diffusive transfer. Consequently, there should be no effect due to applied voltage, and we expect the amount of protein transferred to increase linearly with time and concentration. To test these assumptions, we ran serial dilutions of Alexa 555 Ovalbumin (Invitrogen), from 0.3 µg to 19 pg, on a 1mm, 15 well 10% Tris glycine gel (Invitrogen), under denaturing conditions (Tris-Glycine-SDS Buffer, pH 8). The gels were transferred for 30 minutes under various voltages (0V, 50V) (Figure 3). The slides were scanned with the Axon 4000B (Gain = 600) and the amount of protein transferred was quantified by summing the total fluorescence for each band in MATLAB. The results show an increase in transfer rate as a function of both length of transfer time, and concentration. Additionally, there is no effect on transfer due to the applied electric field.

The protein transferred versus time for each concentration was fit to a first order exponential (Figure 4), which indicates that the protein transfer follows first order kinetics in binding to the slide, and eventually reaches an equilibrium state. Proteins in higher concentration can obtain maximal binding in about 2 hours, while proteins of low quantity can take much longer.

$$F(t) = F_0\left(1 - \exp\left(\frac{-t}{\tau}\right)\right)$$

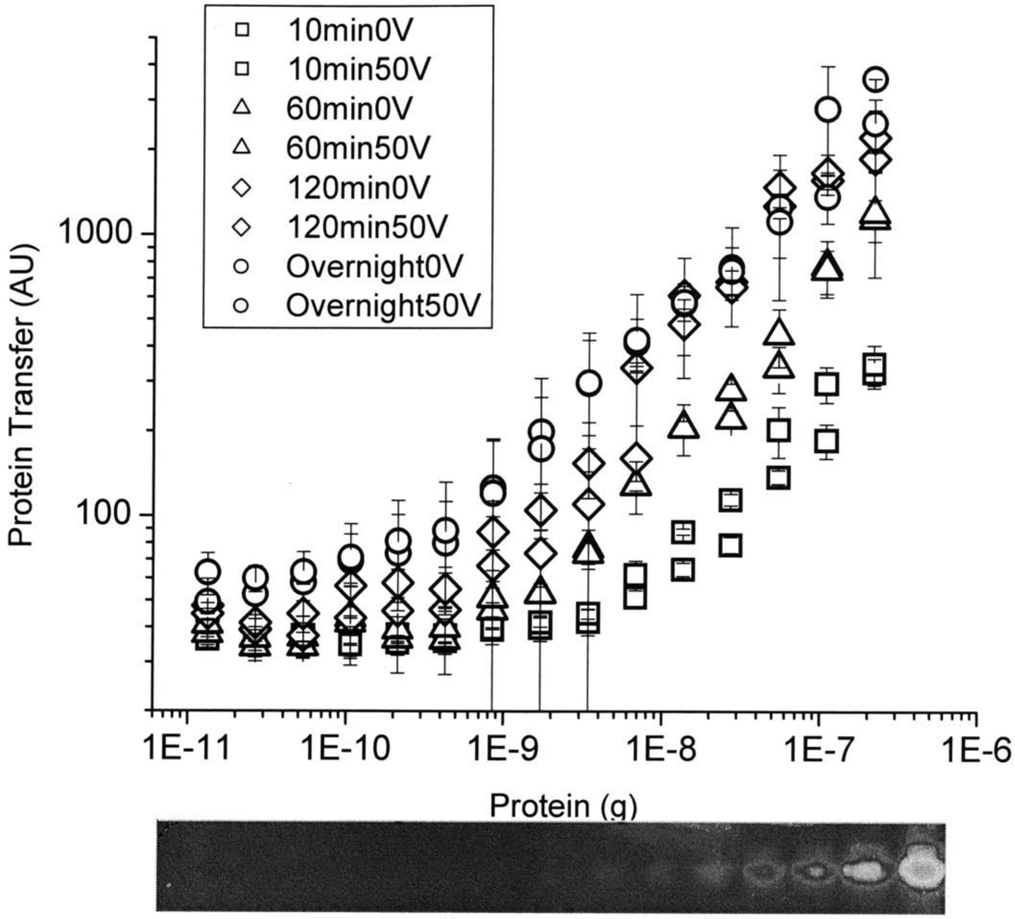

Figure 3: Transfer versus Protein Concentration

Serial dilutions of Alexa 555 Ovalbumin (from 300 ng to 19 pg) were run on a 1 mm, 10% SDS polyacrylamide gel. The gels were transferred to the slide under 0 and 50 Volts, for various times (10 min, 60 min, 120 min, and overnight 12 hours). The slides were scanned, and the intensity of each band was quantified in MATLAB. A sample slide scan is shown below the plot. The graph illustrates that there is no difference in transfer with 50V or 0V. Furthermore, there is an increase in transfer with increasing concentration and transfer time.

Since the rate of transfer is concentration dependent, for the same sample amount, the transfer efficiency can be increased by decreasing the thickness of the gel. Figure 5 shows increasing transfer as the gel is thinner. There is a disproportionate drop in transfer efficiency with a 1.5 mm gel. This is likely due to the protein not being evenly distributed throughout the thickness of the gel, but rather concentrating in the center.

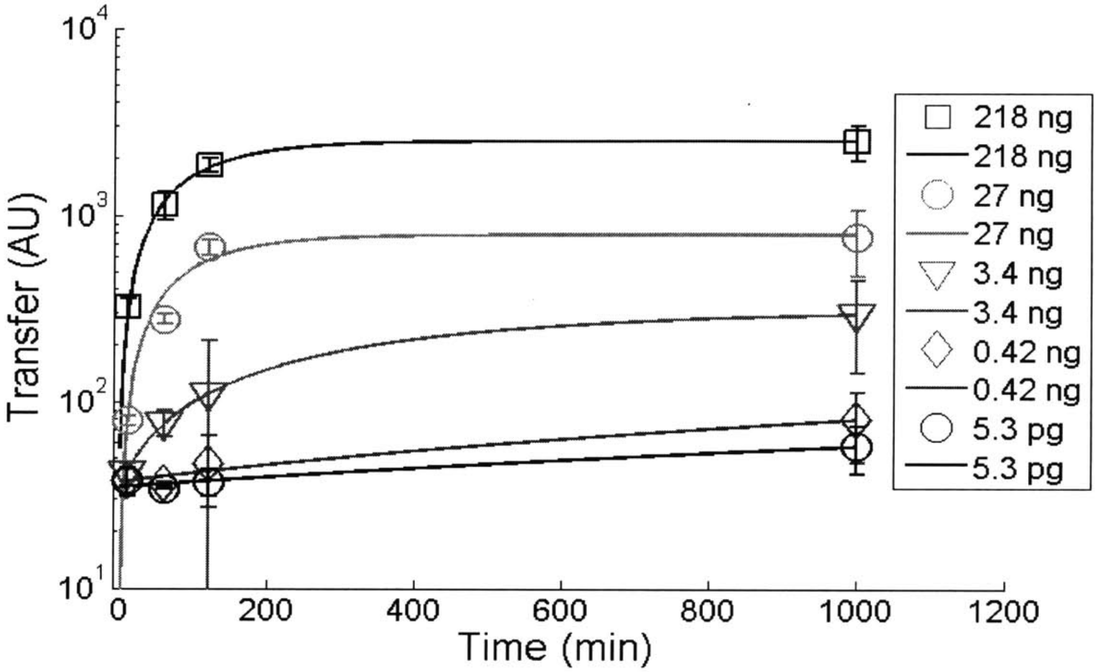

Figure 4: Protein Transfer Versus Time.

The transfer intensity for various concentrations is plotted as a function of time. The curves are first order exponential, indicating that they follow simple diffusive kinetics, eventually reaching equilibrium with the slide.

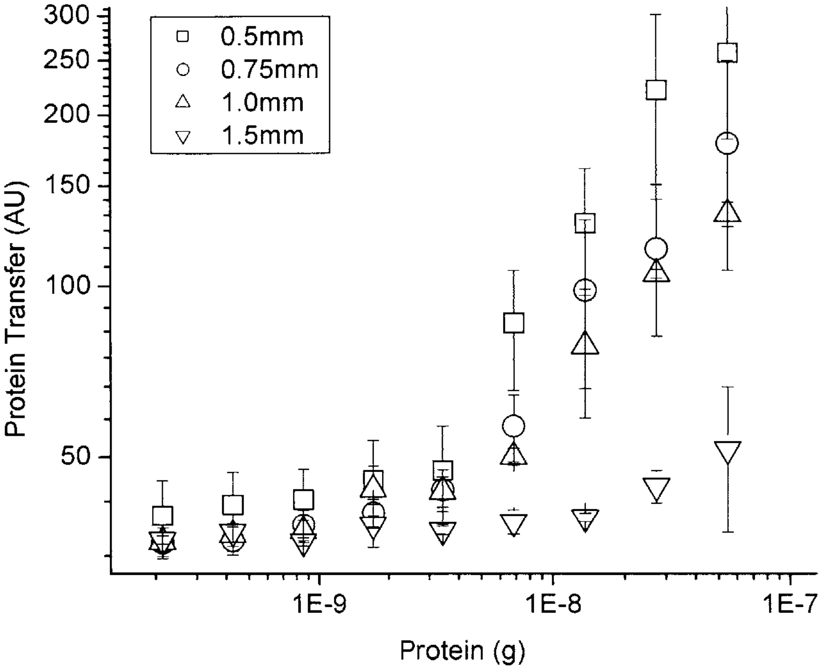

Figure 5: Protein Transfer versus Gel Thickness

Identical amounts of protein (serially diluted) were run in varying thickness of 10% acrylamide gels (0.5 mm, 0.75 mm, 1.0 mm, 1.5 mm). The thinner gels resulted in a greater transfer efficiency. This is consistent with the diffusive model, as the concentration of protein will be increased in a thinner gel.

Western Blots

To apply this technique to identifying protein-protein interactions, we demonstrate that it can be used in a traditional western blot, with two key advantages: (1) that nearly all of the protein remains in the gel for further analysis, and (2) only a small (50 µl) amount of antibody is needed for the assay.

This can be crucial when probing with a rare protein, or involved in high-throughput screening, where many slides may be assayed.

We measure the detection efficiency by using biotinylated BSA, (Sigma) probed with Streptavidin Cy3 (Zymed). Gels (Tris-Glycine, 15 well, 1mm Invitrogen) were run in triplicate with serial dilutions of biotin-BSA ranging from 10 ug to 100 pg. Gels were transferred for 30 minutes, and blocked with 5% BSA in PBS. After washing (PBS), a 1:2000 dilution of streptavidin Cy3 was added for 1 hour. The slides were washed and imaged with the Axon 4000B scanner. Bands were quantified and plotted (with standard deviation, n = 3) in Figure 6. There is a 10 ng detection limit after 30 minutes.

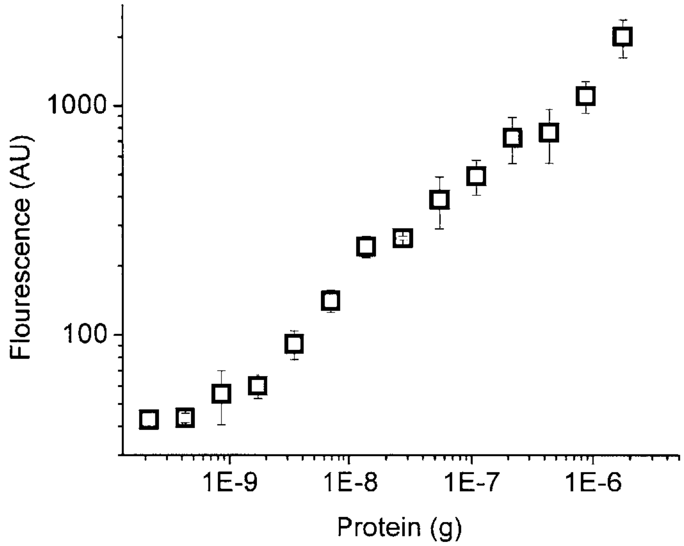

Figure 6: Biotin BSA Transfer

Serial dilutions of biotinlylated BSA were run on a 10% gel and transferred to an aminosilane slide for 30 minutes. The slides were blocked and hybridized with Streptavidin Cy3 for 1 hour. The slides were washed and scanned in the Axon

4000B scanner. The minimum detection limit was 10 ng of biotin BSA after 30 minutes.

To further probe the detection limit, and illustrate the fact that protein remains in the gel after a western blot, we directly compared a western transfer using our novel µstamping techniques, and a traditional western blot. Figure 7 shows the comparison of a western blot with the transfer method. Serial dilutions of 1mg/ml (5 µl) biotin BSA were run in a 10% SDS gel and transferred for 1 hour or overnight to a slide, or for 40 min at 80 mA to nitrocellulose. The Western blot was developed with avidin-HRP and ECL Plus (Amersham), and imaged on film (Kodak). 300 pg is easily seen on the western, where as the detection limit on the slide is about 10-20 ng for 1 hour, and down to 300 pg for over night. Very little protein is left in the gel after the western blot, whereas virtually all of the protein remains in the gel after the transfer procedure. Although for low amounts the Western blot is more sensitive at shorter time scales, by allowing the transfer to continue overnight, similar detection levels can be achieved. Figure 7 shows the comparison of a western blot with the transfer, for serial dilutions of biotin BSA down to 19 pg. A detection limit of 150 pg is achieved with the Western blot, while 19 pg can be seen with an overnight transfer. Thus the detection limit can be even lower for the microarray transfer method, although the transfer time is increased. Nonetheless, regardless of the amount transferred, the vast majority still remains in the gel. The protein that remains in the gel allows for further biochemical analysis.

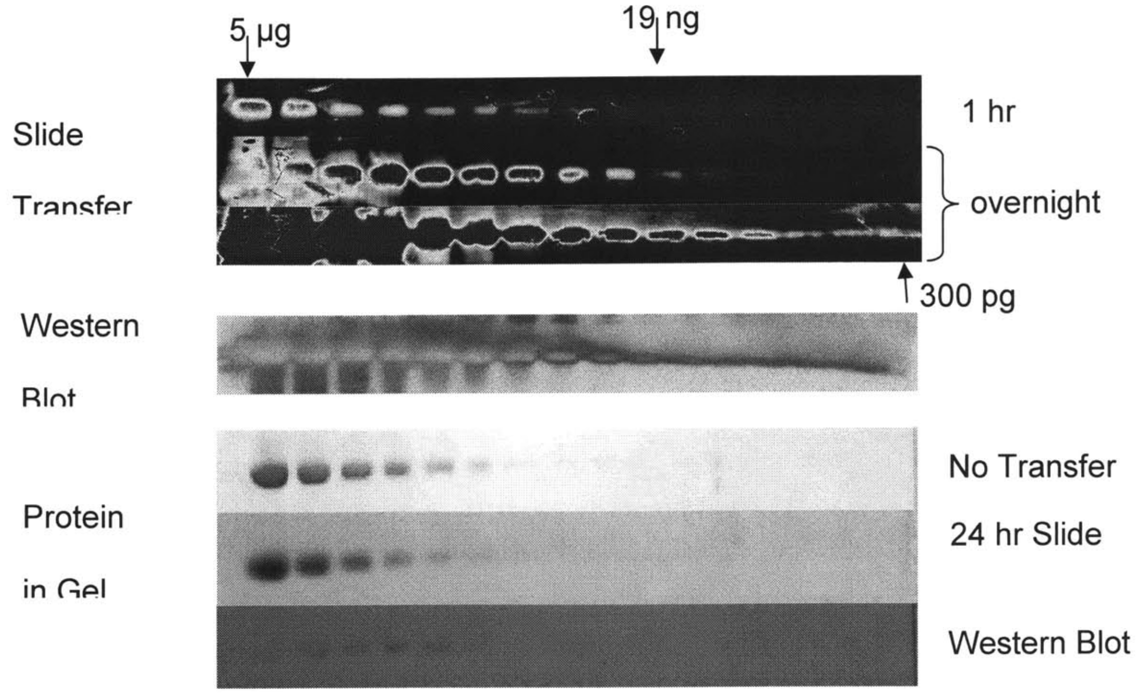

Figure 7: Western Blot versus Transfer

Serial dilutions of biotin BSA were run on identical SDS gels (10%) and either diffusively transferred for 1 hour or overnight to an aminosilane slide, or transferred via western blot to nitrocellulose. Slides were processed as previously described. The western blot was blocked in BSA/Tw, and incubated in Streptavidin HRP. The blot developed using ECL Plus (GE Biosciences). After 1 hour, 19 ng could be detected on the diffusive blot, and after overnight transfer, 300 pg could be detected. Although the transfer time is significantly slower than with a Western Blot, the majority of the protein remains in the gel after transfer, enabling subsequent analysis.

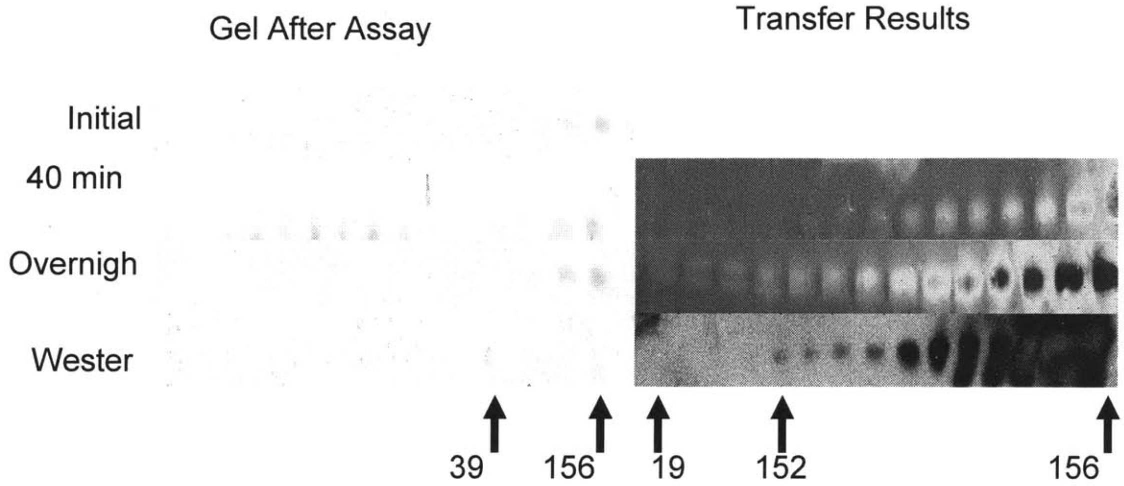

Figure 8: Western Blot Comparison (Low Concentration)
To further probe the detection limits with respect to western blots, we were able to detect 19 pg after overnight transfer using the diffusive method.

Identifying Protein-Protein Interactions in a Complex Mixture

The primary advantage to this technique is the ability to identify novel proteins and interactions in a µarray format. This is accomplished by identifying the location of a binding event on the slide and then correlating it to the location in the gel, where the protein remains. To demonstrate this, we detect biotinylated BSA within a HeLa cell lysate. In Figure 9, lane 1, 100 ng of Biotin BSA was added to a HeLa cell lysate and run on a 10% SDS mini-gel, along with a fluorescent ladder. In lane 2, a ladder is run (Kaleidoscope, BioRad), with bands fluorescent in the Cy3 and Cy5 channels. The gel was transferred for 1 hour, and blocked in 5% BSA in PBS for 3 hours at room temperature. The slide was washed three times in PBS and spun dry. 60 µl of Cy3 Streptavidin (Zymed) was added under a coverslip and incubated at room temperature in a humid chamber for 1 hour. The slide was washed 3 times in PBS, spun dry and imaged (Axon 4000B). The raw images are show in Figure 9. A band can be clearly seen in the lysate at the approximate molecular weight of BSA (66kd). The images are filtered in MATLAB using a Wiener filter, and thresholded. The processed images are shown in Figure 10. The fluorescent intensity on the slide is plotted as a function of position, and the peaks are identified. The plot (Figure 11) shows the Cy5 bands in blue, and the Cy3 bands in red.

The Cy3 band, indicating where the streptavidin bound is excised from the gel and half of the band is subjected to mass spectrometry (ABI QSTAR). The results (MASCOT) are shown in Table 1. The results include Albumin (ALB Protein), but also include several other proteins in the band. Reasonable assumptions regarding binding partners can eliminate several of the candidates. To specifically identify the target protein, and allow the process to remain high throughput and unbiased, we further isolate the protein by eluting the proteins from the remaining ½ band (via diffusion) into PBS, and immunoprecipitate with streptavidin coated beads. The protein is removed from the beads by incubating the beads in 6 M Guanidine-HCL, and identified with mass spectrometry. The results are shown in Table 2. The results clearly identify the target protein (excluding contaminants keratin and trypsin).

Raw Image: Biotin BSA in Hela Lysate

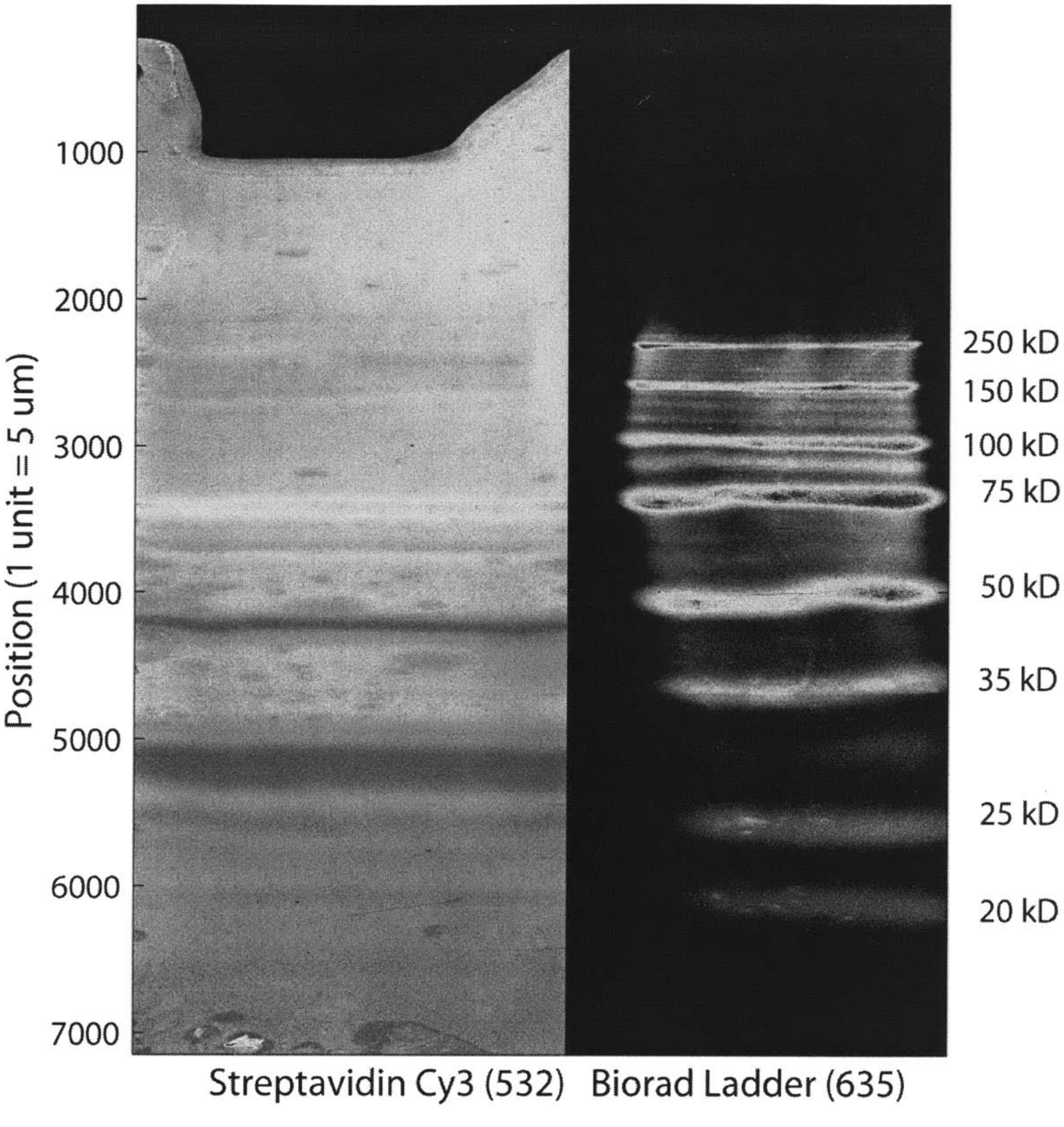

Figure 9: Hela cell lysate with Biotin BSA (Raw Image).

The raw scan image from the gel transfer, showing the Cy3 (Streptavidin) channel on the left, and the Cy5 (BioRad ladder) on the right.

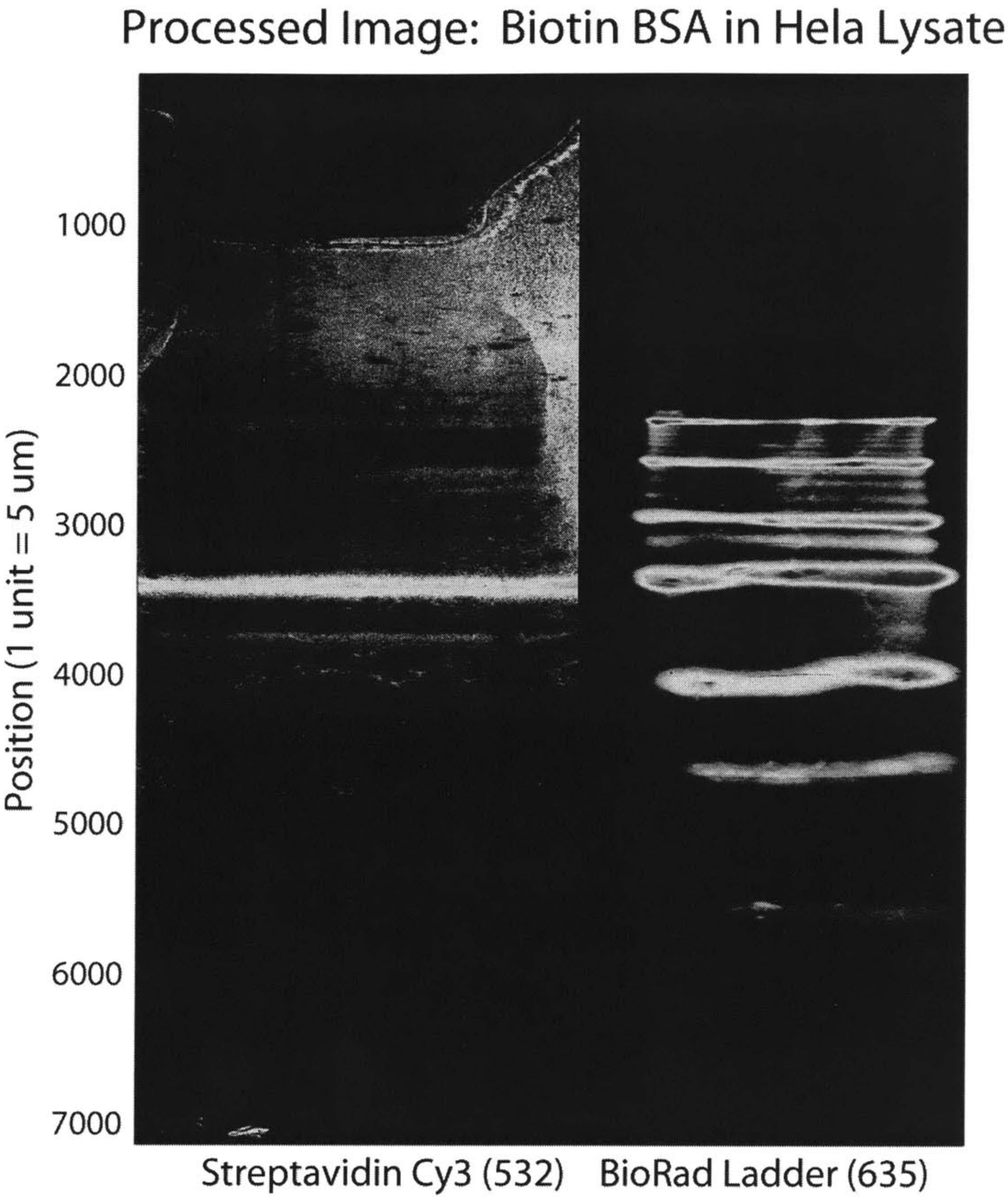

Figure 10: Hela cell lysate with Biotin BSA (processed image).

The processed (filtered and threshold) image, clearly showing the Cy3 (Streptavidin) band.

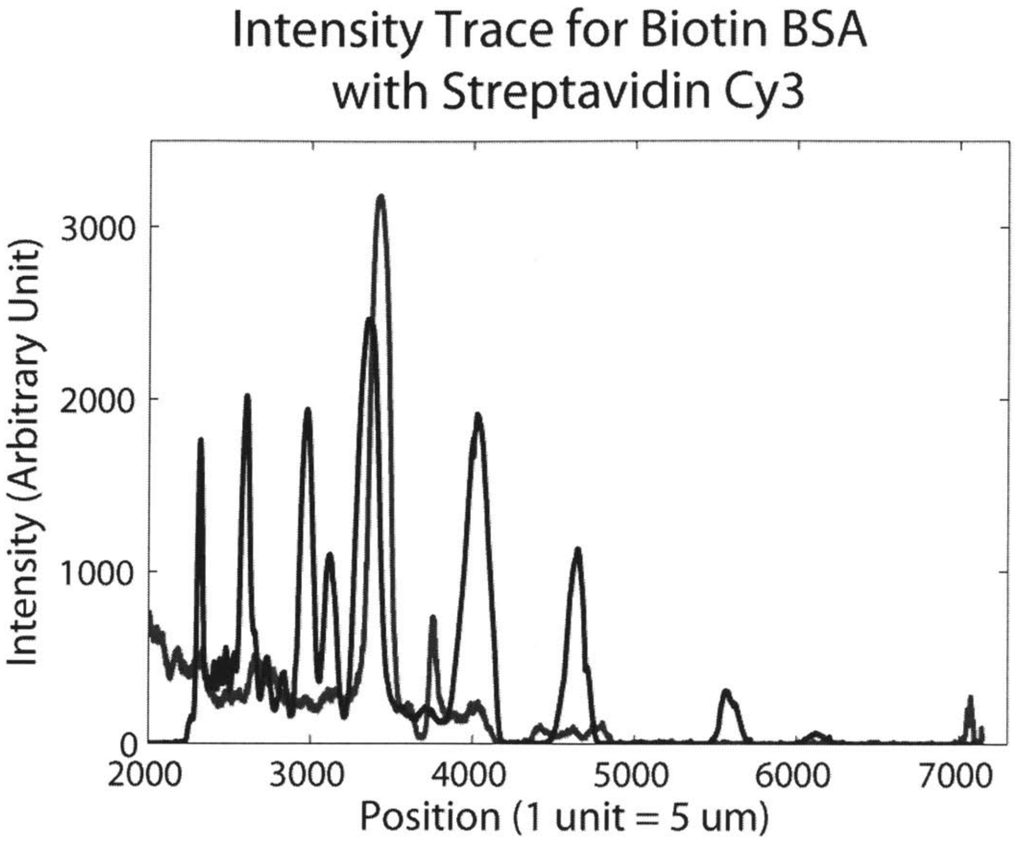

Figure 11

This is the trace (average across the horizontal axis) of the ladder (blue) and the Cy3 Streptavidin (red). The bands (from left to right) are 250 kD, 150 kD, 100 kD, 75 kD, 50 kD, 37 kD and 25 kD The Cy3 peak is to the right of the 75 kD band, indicating that its molecular weight is less than 75 kD. The corresponding area on the gel was excised and analyzed with mass spectrometry

Protein Description	**MOWSE Score**	**Protein Mass**	**Protein Coverage**
(P11142) Heat shock cognate 71 kD protein (Heat shock 70 kD protein 8)	448	71082	34.8

(Q59EJ3) Heat shock 70kDa protein 1A variant (Fragment)	328	78018	29.5
(Q8N1C8) Heat shock 70kD protein 9B (Mortalin-2) (Fragment)	287	74093	17.9
(P29401) Transketolase (EC 2.2.1.1) (TK)	229	68519	28.3
(P17066) Heat shock 70 kD protein 6 (Heat shock 70 kD protein B~)	224	71440	13.8
(P02545) Lamin-A/C (70 kD lamin) (NY-REN-32 antigen)	203	74380	31.5
(Q6FG89) G22P1 protein	202	70114	24
(P34931) Heat shock 70 kD protein 1L (Heat shock 70 kD protein 1-like) (Heat shock 70 kD protein 1-Hom) (HSP70-Hom)	201	70730	19
(P26038) Moesin (Membrane-organizing extension spike protein)	170	67761	24.5
(P11940) Polyadenylate-binding protein 1 (Poly(A)-binding protein 1) (PABP 1)	147	70854	20.4
(Q2KHP4) Hypothetical protein	141	72492	16.6
(P20700) Lamin-B1	114	66522	20.7
(P04843) Dolichyl-diphosphooligosaccharide--protein glycosyltransferase 67 kD subunit precursor (EC 2.4.1.119) (Ribophorin I) (RPN-I)	112	68641	15.2
(P08133) Annexin A6 (Annexin VI) (Lipocortin	99	76037	24.6

VI) (P68) (P70) (Protein III) (Chromobindin-20) (67 kD calelectrin) (Calphobindin-II) (CPB-II)			
(O60506) Heterogeneous nuclear ribonucleoprotein Q (hnRNP Q) (hnRNP-Q) (Synaptotagmin-binding, cytoplasmic RNA-interacting protein) (Glycine- and tyrosine-rich RNA-binding protein) (GRY-RBP) (NS1-associated protein 1)	98	69788	14.3
(Q12931) Heat shock protein 75 kD, mitochondrial precursor (HSP 75) (Tumor necrosis factor type 1 receptor-associated protein) (TRAP-1) (TNFR-associated protein 1)	93	80345	14.2
(Q9BV64) HNRPR protein (Heterogeneous nuclear ribonucleoprotein R)	90	71456	11.3
(Q6NUR7) Villin 2 (Ezrin)	83	69313	13.1
(P35241) Radixin	83	68635	8.7
(Q15582) Transforming growth factor-beta-induced protein ig-h3 precursor (Beta ig-h3) (Kerato-epithelin) (RGD-containing collagen-associated protein) (RGD-CAP)	81	75261	3.7
(Q9UJU1) Cytovillin 2 (Fragment)	73	16294	22
(Q96AE4) Far upstream element-binding protein 1 (FUSE-binding protein 1) (FBP) (DNA helicase	71	67602	10.1

V) (HDH V)			
(P13667) Protein disulfide-isomerase A4 precursor (EC 5.3.4.1) (Protein ERp-72) (ERp72)	70	73229	6.7
(Q5D0D7) ALB protein	69	73881	6.9
(Q8IW48) SDHA protein	56	57283	11
(P52272) Heterogeneous nuclear ribonucleoprotein M (hnRNP M)	55	77618	5.2
(Q0JS26) Hypothetical protein PDLIM5 (Fragment)	50	54370	1.8
(Q96I24) Far upstream element-binding protein 3 (FUSE-binding protein 3)	49	61944	1.4
(P03951) Coagulation factor XI precursor (EC 3.4.21.27) (Plasma thromboplastin antecedent) (PTA) (FXI) [Contains: Coagulation factor XIa heavy chain; Coagulation factor XIa light chain]	48	72116	1.9
(Q03252) Lamin-B2	48	67762	2.7
(Q9NTK6) Hypothetical protein DKFZp761K0511	46	85189	4.5
(Q14683) Structural maintenance of chromosome 1-like 1 protein (SMC1alpha protein) (Sb1.8)	45	143771	3.8
(P29966) Myristoylated alanine-rich C-kinase	43	31576	5.7

substrate (MARCKS) (Protein kinase C substrate, 80 kD protein, light chain) (PKCSL) (80K-L protein)			
(P17844) Probable ATP-dependent RNA helicase DDX5 (EC 3.6.1.-) (DEAD box protein 5) (RNA helicase p68)	42	69618	10.1
(Q59F66) DEAD box polypeptide 17 isoform p82 variant (Fragment)	42	81701	4.3
(Q16630) Cleavage and polyadenylation specificity factor 6 (Cleavage and polyadenylation specificity factor 68 kD subunit) (CPSF 68 kD subunit) (Pre-mRNA cleavage factor Im 68 kD subunit) (Protein HPBRII-4/7)	40	59344	2.5

Table 1: Proteins from Extracted Gel Band

Protein Description	**MOWSE Score**	**Protein Mass**	**Protein Coverage**
(Q8IUK7) ALB protein	60	46442	3.8

Table 2: Proteins from immunoprecipitated Gel band.

Conclusion

The high throughput analysis of protein and small molecules is essential for assaying biological systems. µArrays offer an ideal platform to accomplish this, but are limited by the need to generate thousands of proteins and small molecules. We have developed and demonstrated a novel technique to pattern proteome scale µarrays and uniquely identify binding partners. This technique allows high throughput visualization of protein binding interactions. By patterning a proteome-scale microarray, we gain many of the advantages of traditional microarrays, such as assaying multiple samples simultaneously as well as the use of minimal reagents. Furthermore, with our technique precious samples can be analyzed by patterned the array, which still retaining the vast majority of protein for further analysis and experimentation.

References

H. Zhu, M. B., R. Bangham, D. Hall, A. Casamayor, P.Bertone, N. Lan, R. Jansen, S. Bidlingmaier, T. Houfek, T. Mitchell, P. Miller, R. A. Dean, M. Gerstein, M. Snyder (2001). "Global Analysis of Protein Activities Using Proteome Chips." Science **293**(5537): 2101-2105.

S. P. Gygi, Y. R., B. R. Franza, R. Aebersold (1999). "Correlation between protein and mRNA Abundance in Yeast." Molecular and Cellular Biology **19**(3): 1720-1730.

Schreiber, G. M. a. S. L. (2000). "Printing Proteins as Microarrays for High-Throughput Function Determination." Science **5485**(289): 1760-1763.

Scofield, B. T. K. a. R. H. (1997). "Western Blotting." J. Immunol. Method **205**: 91-94.

Scofield, B. T. K. a. R. H. (2006). "Western Blotting." Methods **38**(4): 283-293.

Chapter 2: Protein μ-Stamping: Analyzing Changes in the Hela Phosphoproteome in Response to Epidermal Growth Factor

Abstract

Protein μarrays are a tool that can enable high throughput analysis of protein interactions. As discussed in previous chapters, the main difficulty in implementing protein μarrays lies in generating the thousands of proteins necessary to fabricate an array representative of the proteome. In this chapter, we use the protein stamping technique to fabricate an array of the phosphoproteome of Hela cells treated with Epidermal Growth Factor (EGF). We accomplish this by immunoprecipitating the phosphoproteins in the HeLa cell lysate, and patterning them on a μarray substrate. By patterning the phosphoproteome, we can rapidly screen and identify specific changes, as well as probe the array with various target proteins. We demonstrate this by probing the Hela phosphoproteome for further post-translational modifications, specifically ubiquitin-like proteins Ubiquitin and ISG-15. Using our technique, we are able to identify regions of proteins that have either changed phosphorylation states, or undergone multiple post-translational modifications. We can then subject these areas to mass spectrometry to identify the proteins of interest.

Background

We have previously demonstrated the ability to pattern a proteome-scale µarray using a cellular lysate that has key advantages in terms of obviating the need for protein synthesis and being able to simultaneously assay multiple samples with small reaction volumes. We expand on this technique by demonstrating its use in determining the post-translational state of a proteome. There are known to be about 30,000 genes, yet the proteome is considered to have a 10 to 100 fold higher complexity (Walsh 2006). This complexity can be achieved by manipulation at the transition from gene to protein, as well as after the protein is synthesized. Our focus here is the later, termed post-translational modifications.

Post-translational modifications play a key role in developing accurate and representative protein µarrays. Recombinant proteins derived from bacteria or other systems may lack crucial post-translational modifications. These modifications can govern how a protein functions, what it binds to, and what biochemical pathways are active. The proteins within a cellular lysate have the proper post-translational modifications (unlike recombinant proteins) and therefore, it is advantageous to use a cellular lysate to pattern µarrays.

The phosphoproteome was chosen as it represents a key mode of intracellular signaling. Changes in the phosphoproteome state (i.e. proteins becoming phosphorylated by kinases, or dephosphorylated by phosphatases) can reflect the internal activity of the cell, and identify activated or deactivated pathways. As with most all biological processes, there is a feedback system that maintains balance, consisting of kinases (~ 500) and phosphatases (~ 150). Kinases typically transfer a phosphoryl group from ATP (occasionally GTP), and consist of three main types depending on the amino acid they phosphorylate: tyrosine, threonine, and serine.

Assaying the phosphoproteome, or changes thereof requires isolating all phosphorylated proteins (G. Manning 2002; Mann M 2002; Scott B. Ficarro 2002). This is typically done via immobilized metal affinity columns (IMAC), where metal cations bind anionic phosphopeptides, or via immunoprecipitation where beads are coated with antibody that binds to the phosphorylated proteins. Recent efforts have combined the purification of phosphopeptides with SILAC, a method by which proteins incorporated isotope labeled amino acids, to determine changes in the phosphoproteome (J. Olsen 2004).

To demonstrate our technique, we select a subset of the phosphoproteome: proteins with phosphorylated tyrosines. Tyrosines compose the smallest fraction of phosphoproteins (pS:Pt:Py → 1800:200:1 (Mann M 2002), and highly specific antibodies are available commercially. Although a small fraction of the total protein phosphorylation, phosphorylated tyrosines represent a significant component of cellular signaling. Of the 500 total kinases, 91 are protein tyrosine kinases (G. Manning 2002)) and these kinases are responsible for 10% of the phoshoprotein activity in cells (Walsh 2006).

The studies of the phosphoproteome have thus far been limited to identification and comparison of changes (i.e. treated vs. untreated). Our technique seeks to expand on this, by allowing not only a comparison the state of the phosphoproteome, but the ability to pattern the phosphoproteome as a μarray, and conduct subsequent assays. For our example, we look at proteins with multiple post-translational modifications. Typically, a specific protein is probed for, or a modification on a target protein is assay. Here we demonstrate the ability to look at two additional post-translational modifications (limited only by the number of colors on our scanner). As a general technique, any interactome could be patterned, and any microarray assay could be done on that interactome. Determining post-translational modifications on a proteome scale can be accomplished via mass-spectrometry (Jensen 2003), but is not efficient when large number of proteins are scanned within the same sample. This limits the accuracy of mass spectrometry in determining post-translational modifications in high throughput applications. Protein sample complexity can be reduced by immunoprecipitation. Using SILAC (J. Olsen 2004) followed the phosphorylation of EGFR as a function of time. A similar immunoprecipitation approach was taken by Peng et al (Junmin Peng 2003) to determine proteins in yeast that were Ubiquitinylated. His-6 tagged Ubiquitin was incorporated onto proteins, and then separated using a nickel column, and over 1000 proteins were identified, with the modification confirmed on 77 proteins during mass spectrometry.

Ubiquitin and Ubiquitin-like proteins (UBL) are a family of post-translational modifications that are responsible for a variety of functions, from signaling to protein degradation. The Ubiquitin family differs from other post-translational modifications in that the modification is another protein. In the case of Ubiquitin and ISG-15, two closely related modifiers, they are 8 kD and 15 kD respectively.

Ubiquitin can functionalize a protein either in a tandem of 4 monomer. Recently, mono-ubiquitinylation has been found on a wide variety of proteins including histones and plasma membrane receptors. Unlike polyubiquitinylation, monoubiquitinylation is involved in signaling pathways, such as the internal trafficking of membrane receptors. Thus, ubiquitylation can be responsible for a wide range of modifications to a proteins function.

Experimental

Materials and Methods

Lysis Buffer

- 20 mM Tris (pH 7.5)
- 150 mM NaCl
- 1 mM EDTA
- 1 mM EGTA
- 1% Triton X-100
- 2.5 mM Sodium pyrophosphate
- 1 mM b-Glycerolphosphate
- 1 mM Na3VO4
- Roche Protease Inhibitor Tablet
- 1 μM LLnL

3X Sample Buffer

- 187.5 mM Tris-HCl (pH 6.8 at 25°C)
- 6% w/v SDS
- 30% glycerol
- 150 mM DTT
- 0.03% w/v bromophenol blue

Hela cells are grown in 10% FBS (Atlas) in DMEM (Cellgro) supplemented with 1% Penicillin and Streptomycin antibiotics (Cellgro). Cells are grown to 80% confluence in 15 cm dishes. Cells are washed twice in PBS and serum starved for 24 hours in DMEM with penicillin/streptomycin. EGF is added at a concentration of 200 ng/ml for 5 minutes and 2 hours. Cells are then washed twice in ice cold PBS and lysis buffer is added for 5 minutes while the cells were rocked on ice. Cells were then scraped and sonicated 4 times for 5 seconds. Lysates were then spun for 20 minutes at 14,000 rpm at 4C. The supernatant was removed and placed in a test tube. 50 µl of anti-phosphotyrosine agarose beads was added to the lysates and incubated for 24 hours at 4C.

The lysates with beads were then spun at 10,000 rpm for 30 seconds and the supernatant is removed. The beads were resuspended in 500 µl of lysis buffer and washed 4 times. The beads were then mixed in 30 µl of 3X sample buffer and vortexed for 30 seconds. The mixture was centrifuged (room temperature) for 30s at 10,000g and heated at 95C for 5 minutes. The sample buffer was then loaded on to a Biorad 1mm minigel (10%). Neighboring lanes were loaded with 1.25 ul of Biorad Blue Ladder (Biorad). The gels were run for 30 minutes at 25 V (15 mA, constant voltage), and then at 50 V (25 mA) 2 hours at room temperature.

The gels are then removed and air dried for 10 minutes. Aminosilane slides without barcodes (Corning) are placed on the gels and put in a humid chamber overnight (17 hours). The slides are removed and blocked in 5% BSA (Sigma) in TBS for 3 hours at room temperature. The gels are cut into 2 mm slices and the bands are placed in a 96 well plate and frozen. The slides are then submerged in antibody solution. The antibody solution consists of a 1:100 dilution of Alexa Flour 660 Py20 anti-Tyrosine Phosphatase (Santa Cruz Biotechnology), Alexa Flour 488 anti-Ubiquitin (Santa Cruz Biotechnology), and ISG-15 conjugated to Alexa Flour 532 (Santa Cruz Biotechnology). The slides are incubated overnight at 4C on a rocker. Slides are washed 3 times in tris-buffered saline (TBS) for 5 minutes and then spun dry on a slide mini-centrifuge (Telechem). Slides are scanned in an Axon 4000A four-channel scanner at 5 um resolution with 4 line averaging. Scans are recorded for 488, 532 and 660 nm channels, and saved as TIF files.

Image Processing

The images are imported into MATLAB, and processed. First, regions containing air bubbles are eliminated. These can be visualized as circles with low fluorescence, surrounded by a ring of high fluorescence. Next, pixels which saturate the detector are eliminated. Finally, the image if filtered with a Wiener filter (low pass). The resulting image is averaged to obtain the trace.

Results

Cellular lysates were taken from HELA cells treated with EGF for 0, 5 and 120 minutes as previously described. The lysates were immunoprecipitated with anti-phosphotyrosine beads, run on an SDS gel and transferred to a chemically functionalized slide. The patterned microarrays of the HELA phosphoproteomes were probed with anti-phosphotyrosine, anti-Ubiquitin and anit-ISG15 antibodies. The raw images are shown in Figure 12. The filtered images are shown in Figure 13. The results can be more clearly seen when looking at the sum traces (Figure 14, Figure 15, Figure 16).

The control state (no EGF treatment) is shown in Figure 14. The Ubiquitin and ISG traces closely follow each other, and this is likely due to the similar nature of the structure of both Ubiquitin and ISG. The phosphorylation state is described by the red curve, indicating the intensity of the proteins patterned (which correlates to their concentration in the immunoprecipitate). Upon activation with EGF, there is a drastic change in the phosphoproteome. Several higher-molecular weight (75kD – 100 kD) proteins show greater expression (i.e.

phosphorylation) than in the un-stimulated state. After 2 hours of treatment, the phosphoproteome largely returns to baseline.

This technique allows the researcher to quickly identify regions of change. The areas of the gel that exhibit changes in the phosphoproteome can be subjected to mass spectrometry, as the majority of the protein still remains in the gel. Additionally, once the phosphoproteome is patterned, the μarray can be probed with other targets. In this experiment, we investigated proteins with multiple post-translational modifications. The phosphoproteomes of the three conditions were screened with anti-Ubiquitin and anti-ISG antibodies. Several regions were identified with proteins that were both phosphorylated and Ubiquitinylated. These regions were extracted and subjected to mass spectrometry.

Conclusion

Using the protein μstamping technique, we have demonstrated the ability to pattern a protein array, and use the array to both image the state of the proteome as well as conduct assays with multiple targets. In the experiment shown in this chapter, we have patterned the phosphoproteome of Hela cells under varying treatments with EGF (0, 5 and 120 minutes). The changes in the phosphoproteome are easily identified by imaging the patterned μarray. These changes represent the proteins of interest when evaluating this signaling pathway. The vast majority of the protein sample is retained in the polyacrylamide gel, and can be easily extracted for further analysis, such as by mass spectrometry. Additional analysis of the phosphoproteome can be undertaken since the phosphoproteome has been patterned as a μarray. Limited only by the color resolution of the scanner, multiple ligands can be probed. In this situation, we use the array to visualize proteins with multiple post-translational modifications. We identify several proteins that are both phosphorylated and Ubiquitinylated.

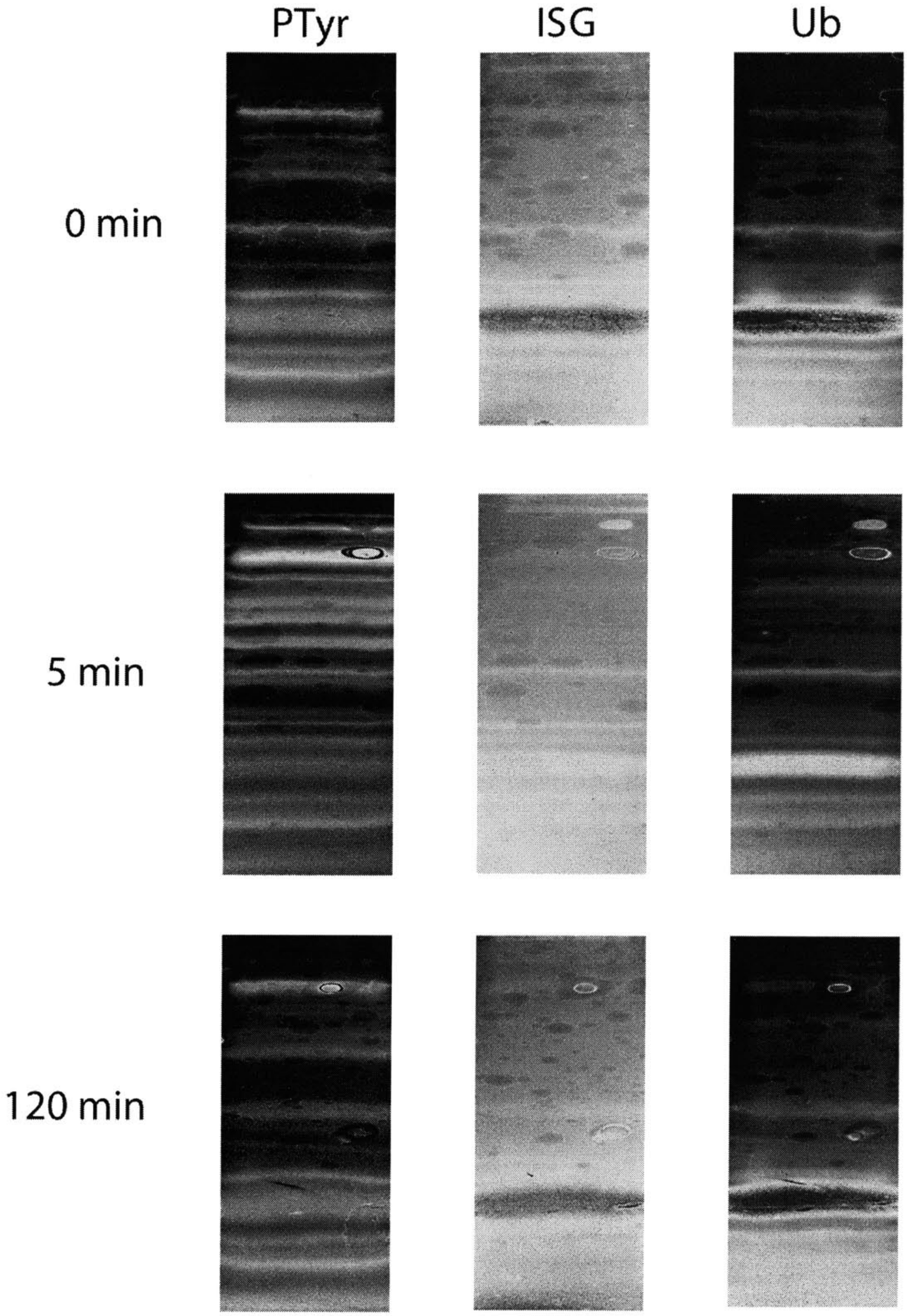
PTyr
ISG
Ub
0 min
5 min
120 min

Figure 12: Raw Images from Gel Transfer

The raw images from three time points (0, 5 and 120 minutes) of EGF treatment to serum-starved Hela cells. The phosphoproteome has clear changes at the 5 minute time point, which revert to the original state at 2 hours. Additionally post-translational modifications, Ubiquitin and ISG, are seen in the accompanying images. Due to the structural similarity of Ubiquitin and ISG, the antibody binding overlaps.

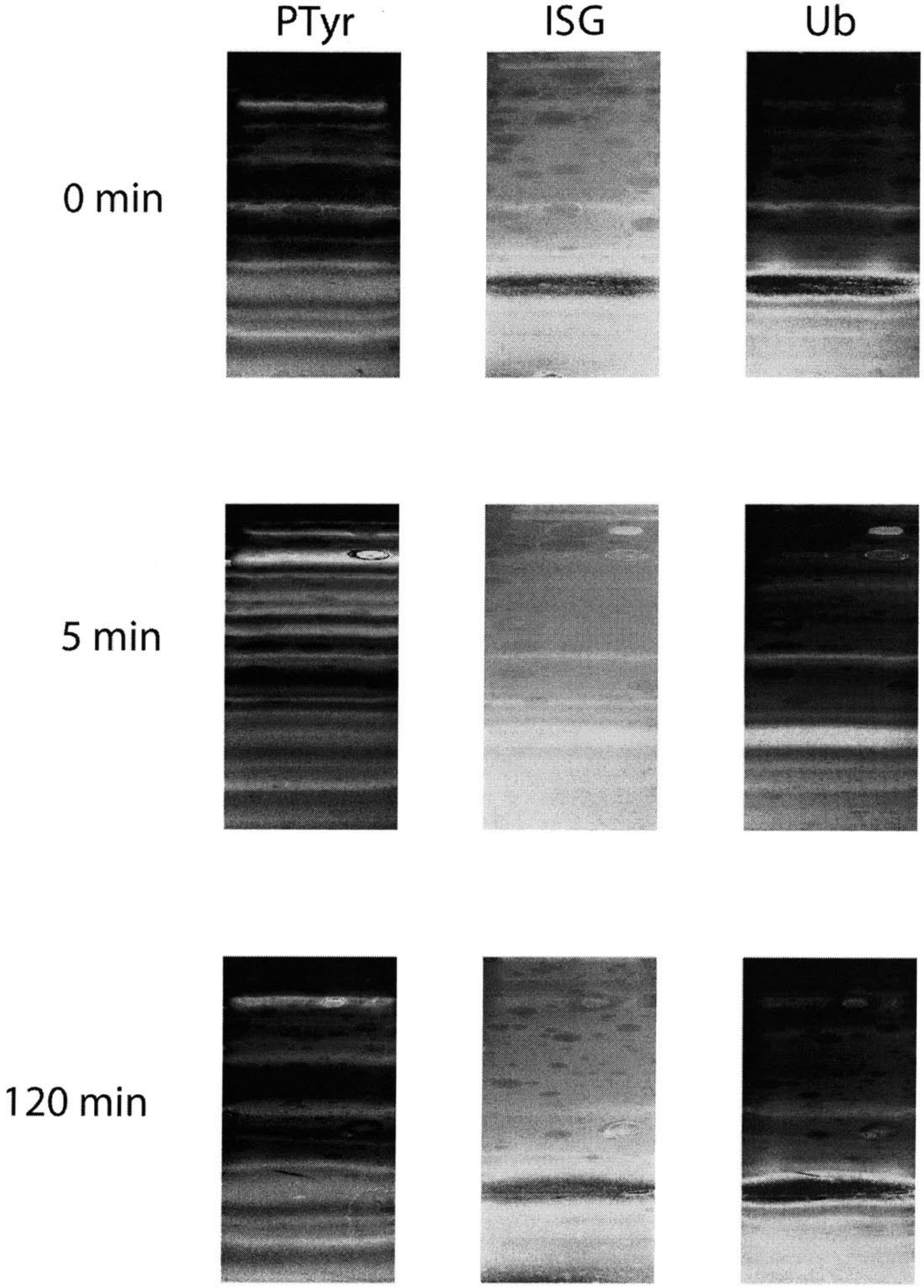
PTyr
ISG
Ub
0 min
5 min
120 min

Figure 13: Filtered Images

The processed images.

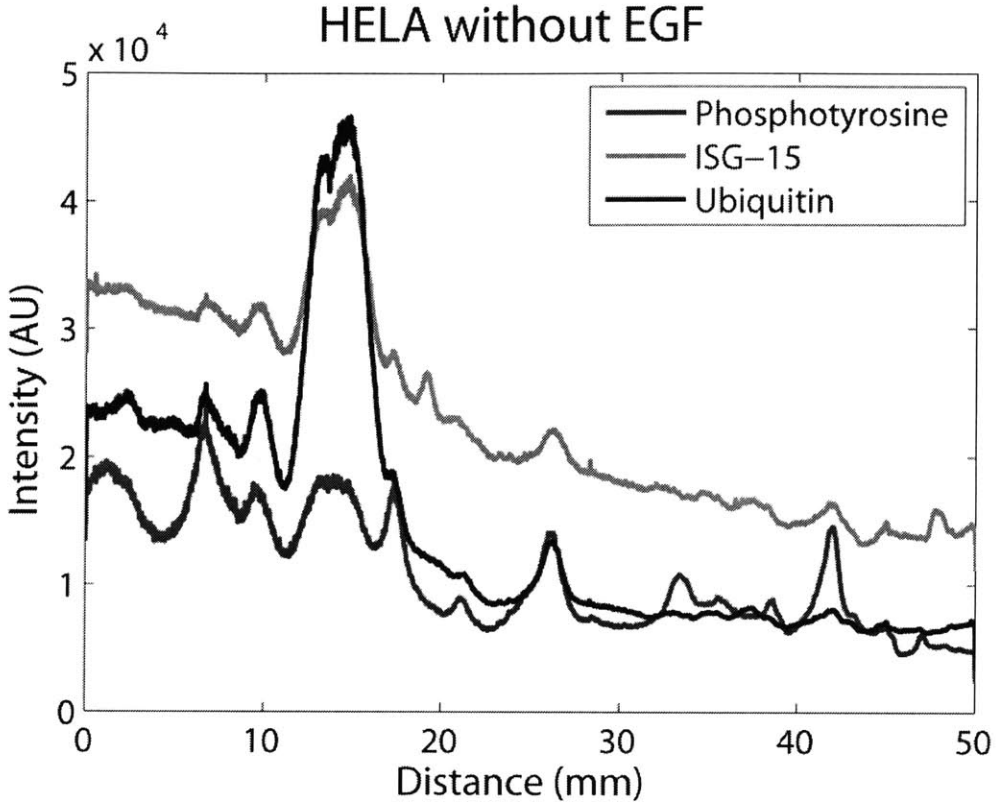

Figure 14: 0 minute EGF Hela

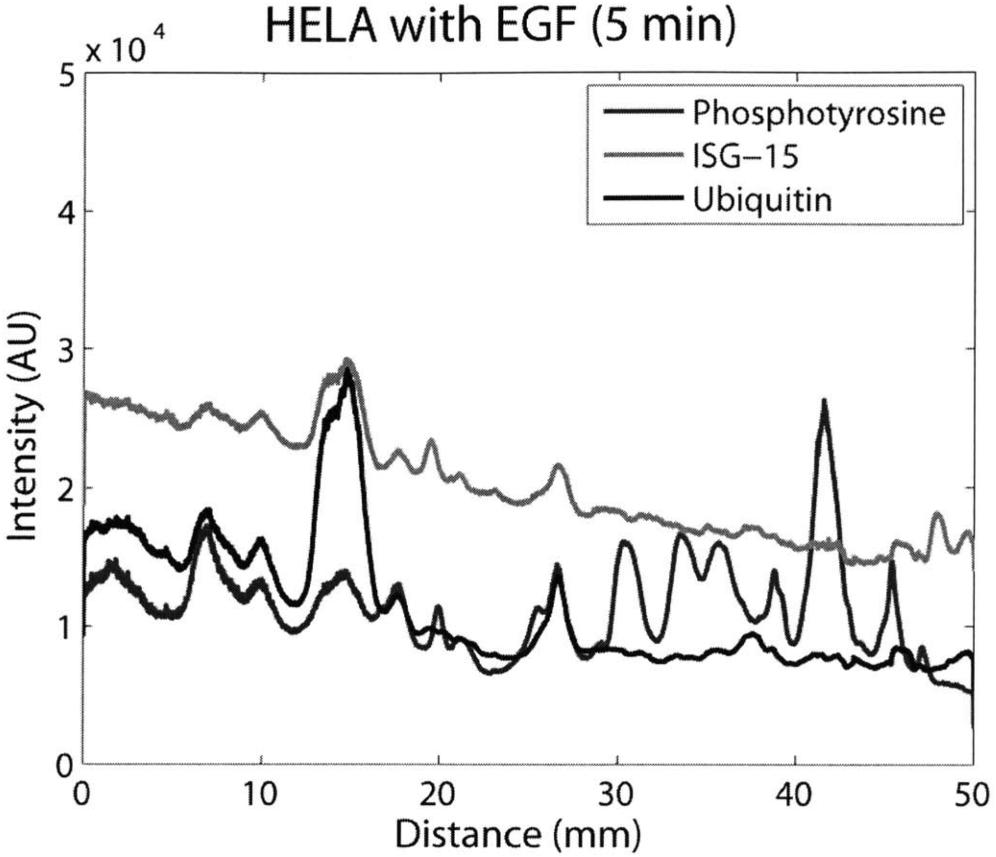

Figure 15: 5 minute EGF treatment

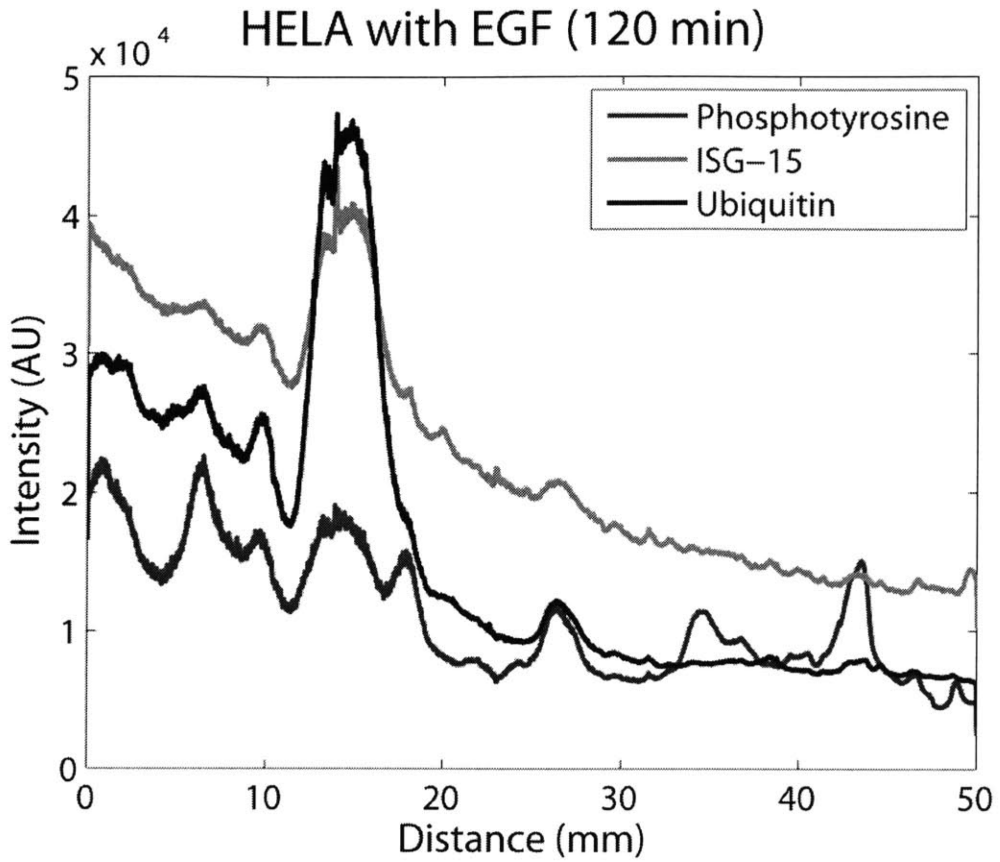

Figure 16: 120 minute Hela Treatment

References

Ando, T., N. Kodera, et al. (2003). "A high-speed atomic force microscope for studying biological macromolecules in action." Chemphyschem **4**(11): 1196-202.

Ando, T., N. Kodera, et al. (2001). "A high-speed atomic force microscope for studying biological macromolecules." Proc Natl Acad Sci U S A **98**(22): 12468-72.

Barbaro, M. B., A.; Raffo, L.; (2006). A charge-modulated FET for detection of biomolecular processes: conception, modeling, and simulation. IEEE Transactions on Electron Devices.

Binnig, G., C. F. Quate, et al. (1986). "Atomic force microscope." Phys. Rev. Letts. **56**: 930-933.

Chen Xu, J. L., Yijin Wang, Lu Cheng, Zuhong Lu, M. Chan (2005). "A CMOS-compatible DNA microarray using optical detection together with a highly sensitive nanometallic particle protocol." IEEE Electron Device Letters **26**(4): 240-242.

Claudio Stagni, C. G., Luca Benini, Bruno Ricco, Sandro Carrara, Christian Paulus, Meinrad Schienle, Roland Thewes (2007). " A Fully Electronic Label-Free DNA Sensor Chip." IEEE Sensors Journal **7**(4): 577-585.

D. Baselt, G. U. L., M. Natesan, S.W. Metzger, P.E. Sheehan and R.J. Colton (1998). "A biosensor based on magnetoresistance technology." Biosensors and Biotechnology **13**: 731.

Eltoukhy, H. S., K.; Gamal, A.E. (2006). "A 0.18-/spl mu/m CMOS bioluminescence detection lab-on-chip." IEEE Journal of Solid-State Circuits **41**(3): 651-662.

G. Manning, D. B. W., R. Martinez, T. Hunter, S. Sudarsanam (2002). "The Protein Kinase Complement of the Human Genome." **298**: 1912-1934.

Goldsbury, C., J. Kistler, et al. (1999). "Watching amyloid fibrils grow by time-lapse atomic force microscopy." J Mol Biol **285**: 33-39.

Guthold, M., M. Bezanilla, et al. (1994). "Following the assembly of RNA polymerase-DNA complexes in aqueous solutions with the scanning force microscope." Proc Natl Acad Sci USA **91**: 12927-12931.

Gygi SP, R. B., Gerber SA, Turecek F, Gelb MH, Aebersold R (1999). "Quantitative analysis of complex protein mixtures using isotope-coded affinity tags." Nature Biotechnology **17**(10): 994-999.

H. Zhu, M. B., R. Bangham, D. Hall, A. Casamayor, P.Bertone, N. Lan, R. Jansen, S. Bidlingmaier, T. Houfek, T. Mitchell, P. Miller, R. A. Dean, M. Gerstein, M. Snyder (2001). "Global Analysis of Protein Activities Using Proteome Chips." Science **293**(5537): 2101-2105.

Haga, H., M. Nagayamam, et al. (2000). "Time-lapse viscoelastic imaging of living fibroblasts using force modulation mode in AFM." J Electron Microsc **49**: 473-481.

Hofmann, F. F., A.; Holzapfl, B.; Schienle, M.; Paulus, C.; Schindler-Bauer, P.; Kuhlmeier, D.; Krause, J.; Hintsche, R.; Nebling, E.; Albers, J.; Gumbrecht, W.; Plehnert, K.; Eckstein, G.; Thewes, R.; (2002). Fully electronic DNA detection on a CMOS chip: device and process issues. Electronic Devices Meeting, IEDM.

J. Olsen, B. B., F. Gnad, B. Macek, C. Kumar, P. Mortensen, M. Mann (2004). "Global, In Vivo, and Site-Specific Phosphorylation Dynamics in Signaling Networks." Cell **127**(3): 635-648.

Jensen, M. M. O. N. (2003). "Proteomic analysis of post-translational modifications." Nature Biotechnology **21**: 251-261.

Junmin Peng, D. S., Joshua E Elias, Carson C Thoreen, Dongmei Cheng, Gerald Marsischky, Jeroen Roelofs, Daniel Finley, & Steven P Gygi (2003). "A proteomics approach to understanding protein ubiquitination." Nature Biotechnology **21**: 921-926.

Malkin, A. J., Y. G. Kuznetsov, et al. (1996). "Incorporation of microcrystals by growing protein and virus crystals." Proteins **24**: 247-252.

Mann M, O. S., Grønborg M, Steen H, Jensen ON, Pandey A. (2002). "Analysis of protein phosphorylation using mass spectrometry: deciphering the phosphoproteome." Trends Biotechnology **20**(6): 261-268.

Mann, S.-E. O. a. M. (2007). "A practical recipe for stable isotope labeling by amino acids in cell culture (SILAC)." Nature Protocols **1**: 2650-2660.

Niroshan Ramachandran, E. H., Bhupinder Bhullar, Samuel Eisenstein, Benjamin Rosen, Albert Y. Lau, Johannes C. Walter, Joshua LaBaer (2004). "Self-Assembling Protein Microarrays." Science **305**(5690): 86-90.

Ong SE, B. B., Kratchmarova I, Kristensen DB, Steen H, Pandey A, Mann M. (2002). "Stable isotope labeling by amino acids in cell culture, SILAC, as a simple and accurate approach to expression proteomics." Molecular and Cellular Proteomics **1**: 376-386.

P-A. Besse, G. B., M. Demierre, V. Pott and R.S. Popovic (2002). "Detection of a single magnetic microbead using a miniaturized silicon Hall sensor." Applied Physics Letters **80**: 4199.

Radmacher, M., M. Fritz, et al. (1994). "Direct observation of enzyme activity with the atomic force microscope." Science **265**(5178): 1577-9.

Richard B. Jones, A. G., Jordan A. Krall and Gavin MacBeath (2006). "A quantitative protein interaction network for the ErbB receptors using protein microarrays." Nature **439**: 168-174.

Ron Bose, H. M., A. Scott Patterson, John K. Bitok, Balamurugan Periaswamy, Joel S. Bader,, Akhilesh Pandey, and Philip A. Cole (2006). "Phosphoproteomic analysis of Her2/neu signaling and inhibition." PNAS **103**(26): 9773-9778.

Ross PL, H. Y., Marchese JN, (2004). "Multiplexed protein quantitation in Saccharomyces cerevisiae using aminereactive
isobaric tagging reagents." Molecular and Cellular Proteomics **3**: 1154-1169.

Rousso, I., E. Khachatryan, et al. (1997). "Microsecond atomic force sensing of protein conformational dynamics: implications for the primary light-induced events in bacteriorhodopsin." Proc Natl Acad Sci U S A **94**: 7937-7341.

Rousso, I., E. Khatchatryan, et al. (1997). "Atomic Force Sensing of Light-Induced Protein Dynamics with Microsecond Time Resolution in Bacteriorhodopsin and Photosynthetic Reaction Centers." J Struct Biol **119**: 158-164.

Rousso, M. A. a. I. (2005). "Atomic force microscopy with time resolution of microseconds." Applied Physics Letters **86**(014101).

S. P. Gygi, Y. R., B. R. Franza, R. Aebersold (1999). "Correlation between protein and mRNA Abundance in Yeast." Molecular and Cellular Biology **19**(3): 1720-1730.

Sarpeshkar, M. O. H. a. R. (2004). "A 10-nW 12-bit Accurate Analog Storage Cell with 10-aA Leakage." Journal of Solid State Circuits **39**(11).

Schoenenberger, C. A. and J. H. Hoh (1994). "Slow cellular dynamics in MDCK and R5 cells monitored by time-lapse atomic force microscopy." Biophys. J. **67**: 929-936.

Schreiber, G. M. a. S. L. (2000). "Printing Proteins as Microarrays for High-Throughput Function Determination." Science **289**(5485): 1760-1763.

Scofield, B. T. K. a. R. H. (1997). "Western Blotting." J. Immunol. Method **205**: 91-94.

Scofield, B. T. K. a. R. H. (2006). "Western Blotting." Methods **38**(4): 283-293.

Scott B. Ficarro, M. L. M., P. Todd Stukenberg, Daniel J. Burke, Mark M. Ross, Jeffrey Shabanowitz, Donald F. Hunt, & Forest M. White (2002). "Phosphoproteome analysis by mass spectrometry and its application to Saccharomyces cerevisiae." Nature Biotechnology **20**: 301-305.

Stoffler, D., K. N. Goldie, et al. (1999). "Calcium-mediated structural changes of native nuclear pore complexes monitored by time-lapse atomic force microscopy." J Mol Biol **287**: 741-752.

Stolz, M., Stofflerm D, et al. (2000). "Monitoring biomolecular interactions by time-lapse atomic force microscopy." J Struct Biol **131**: 171-180.

Thewes, R. H., F.; Frey, A.; Holzapfl, B.; Schienle, M.; Paulus, C.; Schindler, P.; Eckstein, G.; Kassel, C.; Stanzel, M.; Hintsche, R.; Nebling, E.; Albers, J.;

Hassman, J.; Schulein, J.; Goemann, W.; Gumbrecht, W.; (2002). Sensor arrays for fully-electronic DNA detection on CMOS. IEEE International Solid-State Circuits Conference, San Francisco.

Turgut Aytur, J. F., Mekhail Anwar, Bernhard Boser, Eva Harris and P. Robert Beatty (2006). "A novel magnetic bead bioassay platform using a microchip-based sensor for infectious disease diagnosis." Journal Of Immunological Methods **314**(1-2): 21-29.

Ushiki, T., J. Hitomi, et al. (1999). "Imaging of living cultured cells of an epithelial nature by atomic force microscopy." Arch Histol Cytol **62**: 47-55.

Walsh, C. (2006). Posttranslational Modification of Proteins: Expanding Nature's Inventory, Roberts and Co. Publishers.

Chapter 3: Protein μ-Stamping: Quantifying Changes in the Phosphoproteome in Breast Cancer Epithelial Cells in Response to Heregulin

Abstract

Changes in a biological system in response to a drug, or external stimuli, are key to understanding the drugs actions, as well as potential side effects. In order to understand the system wide effects, large scale gene and protein studies must be done. Techniques (such as DNA μarrays and mass spectrometry) have the advantage of being unbiased, and in combination with new labeling techniques, can also be quantitative. Proteins are the effectors of physiologic action making mass spectrometry the preferred choice. The draw back to mass spectrometry is that the entire sample must be analyzed and that the majority of proteins may have not undergone any change. Additionally, further analysis can only be done within the mass spectrometer, and therefore the protein sample cannot be subsequently characterized by protein interactions. Protein μarrays offer an alternative, with high-throughput visualization of protein-protein interactions. In addition, multiple samples can be used simultaneously. The difficulty in generating μarrays lies in synthesizing the thousands of proteins

necessary to be representative of the proteome. A combination of the two techniques, mass spectrometry and μarrays would allow for a high-throughput tool to investigate proteome-wide changes. We demonstrate here the fabrication of proteome-scale μarrays via protein μstamping. Protein targets found on the μarray are identified via mass spectrometry, and using SILAC, the differential expression is quantified. Using this technique, the phosphoproteome of ductal breast cancer cells (T47D) are analyzed in response to Heregulin. Additionally, proteins with dual post-translational modification (Ubiquitin) are also identified.

Background

Many biological techniques focus on a specific biochemical pathway, but a global view of biological systems is needed. Many biological pathways interact, regulate, or are controlled by a variety of other proteins and small molecules in complex feedback networks. Therefore, in order to understand the change in state of in an organism, a systems biology approach is necessary. DNA μarrays have proven to be an effective tool in visualizing global changes in gene expression. Despite their success, proteins and small molecules are the end effectors of biological action, and gene expression is not necessarily indicative of protein expression (S. P. Gygi 1999).

Protein μarrays have been limited in use due to the difficulty in synthesizing proteome-scale μarrays. Efforts have been made to accomplish this (Richard B. Jones 2006), but typically this is limited to several hundred proteins. DNA is easier to manipulate and purify than protein, and Niroshan et al (Niroshan

Ramachandran 2004) leveraged this fact to create a protein μarray composed by using *in-vitro* translation of a gene library.

These technique all require fabrication of substrates, either protein or DNA. The ideal composition for a protein μarray is one in which all necessary components (defined by all potential targets that the protein or small molecule being assayed interacts with) are already synthesized. A cellular lysate meets these conditions, and provides the ideal material with which to pattern a protein μarray. Proteins within a cellular lysate have additional advantages: internal folding is guided by chaperone and may not be accurately replicated in other systems, and proteins have post-translational modifications that can be essential to protein binding, as well as provide information with regards to the state of the cell.

The use of protein lysates to probe protein-protein interactions is traditionally assayed by immunoprecipitation. Immunoprecipitation, when used in combination with mass spectrometry, can enable unbiased identification of protein-protein interactions. In order to accurately identify proteins via mass spectrometry, the sample complexity must be reduced.

In biological assays, proteins that are differentially expressed under different conditions can elucidate the pathways and networks that are affected. Ideally, only these proteins would be analyzed. Our protein μstamping technique, described in previous chapters, allows patterning of a cellular lysate based μarray, while retaining the majority of the sample for further analysis. By patterning a cellular lysate in a μarray format, changes can be easily identified, and the relevant proteins sent for identification via mass spectrometry.

Furthermore, multiple ligands can be probed against the patterned proteome, enabling a level of analysis not possible with immunoprecipitation alone.

The advent of quantitative mass spectrometry has made it possible to easily identify differential changes in protein expression. Several techniques exist for accomplishing this, and each involves labeling a sample with a marker that shifts the molecular weight by a known amount (on the order of a few Daltons). This can be detected with a high resolution mass spectrometer, and the peptides which this shifted mass are compared to the peptides of "normal" mass. The ratios are then computed, and are reflective of the relative concentrations in solution. iCAT (Gygi SP 1999) is a method that uses a biotinylated isotope tag that labels the cysteine residues in a protein. The proteins are immunoprecipitated, digested and subjected to mass spectrometry. Only peptides (and proteins) with cysteine labels are analyzed. A variation on this technique is iTRAQ (Ross PL 2004) whereby protein samples are digested, and a isotope labeled tag is added to the N-terminus of the peptide fragments. The peptide samples are then mixed together and assayed via mass spectrometry. Both of these techniques make use of labeling the cellular lysate. A third method, SILAC (Ong SE 2002), is useful when obtaining lysates form a cell culture. This method uses stable incorporation of isotope-labeled amino acids by growing cells in media with heavy (i.e. isotope labeled) amino acids. `This method achieves approximately 100% incorporation of amino acids in proteins after five cell doublings (Mann 2007).

We seek to integrate these techniques (µarrays and quantitative mass spectrometry) to identify changes in the phosphoproteome due to activation of the Her2/Neu receptor using Heregulin. This receptor plays a crucial role in breast cancer, and therefore its signaling pathways are of vital importance for clinical and scientific research. We select proteins that have a phosphorylated tyrosine to analyze because they represent the smallest fraction of the total phosphorylated proteins (pS:Pt:Py → 1800:200:1 (Mann M 2002)), reducing complexity, yet represent a significant portion of the phosphoproteins activity (Walsh 2006)).

The phosphoproteome of the Her2/Neu pathway has been studied previously (Ron Bose 2006). In this study, we use endogenously expressed Her2/Neu receptors in breast cancer epithelial cells and study the effects of Heregulin on the phosphoproteome. Furthermore, using the µstamping technique we are able to also probe additional post-translational modifications, specifically Ubiquitin.

Experimental

Lysis Buffer

20 mM Tris (pH 7.5)

150 mM NaCl

1 mM EDTA

1 mM EGTA

1% Triton X-100

2.5 mM Sodium pyrophosphate

1 mM b-Glycerolphosphate

1 mM Na3VO4

Roche Protease Inhibitor Tablet

1 μM LLnL

3X Sample Buffer

187.5 mM Tris-HCl (pH 6.8 at 25°C)

6% w/v SDS

30% glycerol

150 mM DTT

0.03% w/v bromophenol blue

Breast cancer epithelial cells (line T47D) were cultured in SILAC media (Pierce) with $^{13}C_6$ L-Lysine and $^{13}C_6$, $^{15}N_4$ L- Arginine ("heavy media") and normal DMEM with 10% Dialyzed FBS. Cells were grown for five population doublings in heavy and light media to insure incorporation of heavy amino acids. Cells were grown to confluence in 15 cm plates and serum starved for 36 hours. Cells grown in normal media were treated with Heregulin for 10 minutes and 3 hours. Cells grown in heavy media were used as the control, and not exposed to Heregulin.

Cells were then washed twice with chilled phosphate buffer saline (PBS), and 1.25 ml of lysis buffer was added. Plates were rocked on ice for five minutes, and cells were removed with a cell scraper. Cells were sonicated four times for five seconds, and spun for 30 minutes at four degrees on a table top centrifuge. The supernatant was removed and equal volumes (600 µl) of control lysate was added to each of the positive samples (10 minutes and 3 hours). To each 1.5 ml vial, 100 µl of anti-phosphotyrosine beads (Cell Signaling Technologies) was added. Beads were incubated with the lysate overnight at 4 degrees with gentle rocking. Beads were washed 4 times in lysis buffer (2 times for 30 seconds, 2 times for 5 minutes). Protein was eluted form the beads by adding 60 µl of sample buffer, vortexing for 30 seconds, centrifuging and then boiling for 5 minutes. The samples were run on a 10% SDS-polyacriylamide gel (Biorad) at 50 V (constant voltage). The gels were transferred as previously described. The slides were probed with anti-phosphotyrosine antibody (635 nm), anti Ubiquitin (488 nm) and anti-ISG (532 nm).

The results of the transfer are shown below. The raw slide images 1 and 2 (Figure 17) show transfers of mixtures of SILAC labeled control (no Heregulin treatment), and 5 and 180 minute treatments, respectively. The arrays are probed with anti-Phosphotryosine 635 (Santa Cruz Biotechnology), and anti-Ubiquitin 488 (Santa Cruz Biotechnology). The processed images are shown in Figure 18. Each time point, or slide, contains a 50/50 mixture of the treated lysate and the control lysate. This gives each image an offset equal to the control image. The relative concentrations of the control and treated are determined via mass spectrometry, as the control lysates are grown in "heavy" media, and the treated lysates are grown in normal or "light" media. The images are averaged, and the traces are shown in Figure 19. The slide images were averaged (across each channel). The highly expressed phosphorylated proteins are easily seen. Furthermore, proteins that are also modified with Ubiquitin can be visualized. Figure 20 shows a direct comparison of post-translational modification states. The states of both the phosphoproteome, as well as proteins with the additional modification of Ubiquitin, are directly compared across short and long term exposure to Heregulin. Each trace contains the sum of the expression of the control and of the treated state. The state of Ubiquitylation is largely unchanged, but the phosphorylation state shows significant differences when subjected to short and long term exposure.

Conclusion

The µstamping technique enables rapid fabrication of protein µarrays without the need for synthesizing the proteome. Using a cellular lysate, all necessary proteins are already synthesized with the appropriate post-translational modifications. Furthermore, the vast majority of protein remains available for further analysis. We integrate our array fabrication technique with the ability to quantitatively analyze differential protein expression via mass spectrometry using isotope labeled samples (SILAC). Together, this gives the researcher the tools to conduct high-throughput analysis of protein-protein interactions, and then identify and quantify changes using mass-spectrometry on the relevant proteins.

Using this technique, we have visualized the changes in the phosphoproteome of ductal breast cancer cells (T47D) in response to Heregulin. By pattering the phosphoproteome in a μarray format, we are able to probe binding to multiple targets. In this example, we use this capability to probe simultaneous post-translational modifications (Ubiquitin). We discover several proteins that are both phosphorylated and Ubiquitinylated.

5 min Heregulin / Negative Control **3 hrs Heregulin / Negative Control**

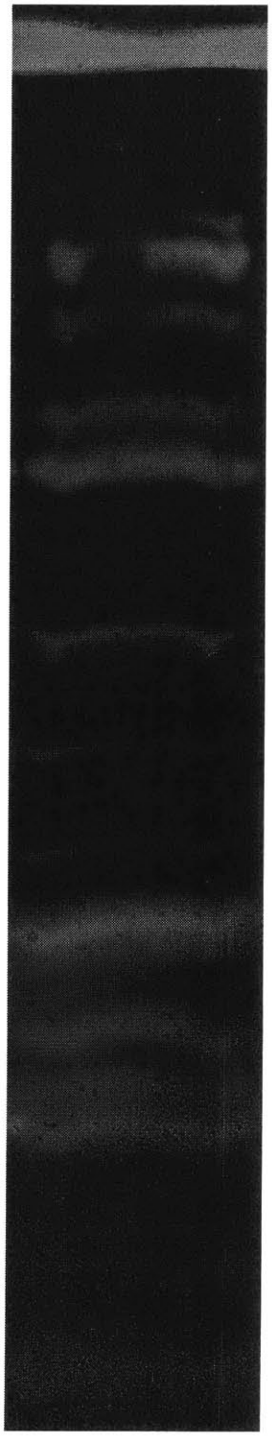

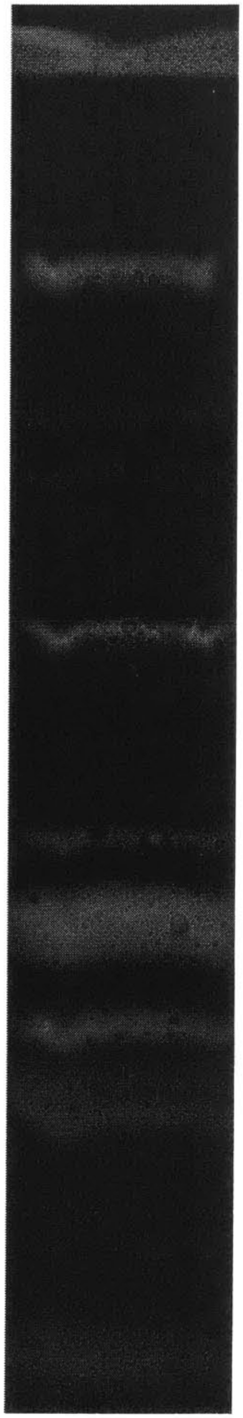

Figure 17: Slide Images from Heregulin Treated Phosphoproteome.

Slide 1 is the µstamped image from T47D (Breast Ductal Carnicoma) line treated with 5 minutes of Heregulin, mixed with control sample. The control sample is SILAC-labeled, and can be differentiated on the mass spectrometer. Slide 2 is the µstamped image from 180 minutes of treatment, mixed with SILAC-labeled control. Proteins with phosphate-labeled tyrosines are shown in red, and proteins that are also Ubiquitinylated are shown in blue.

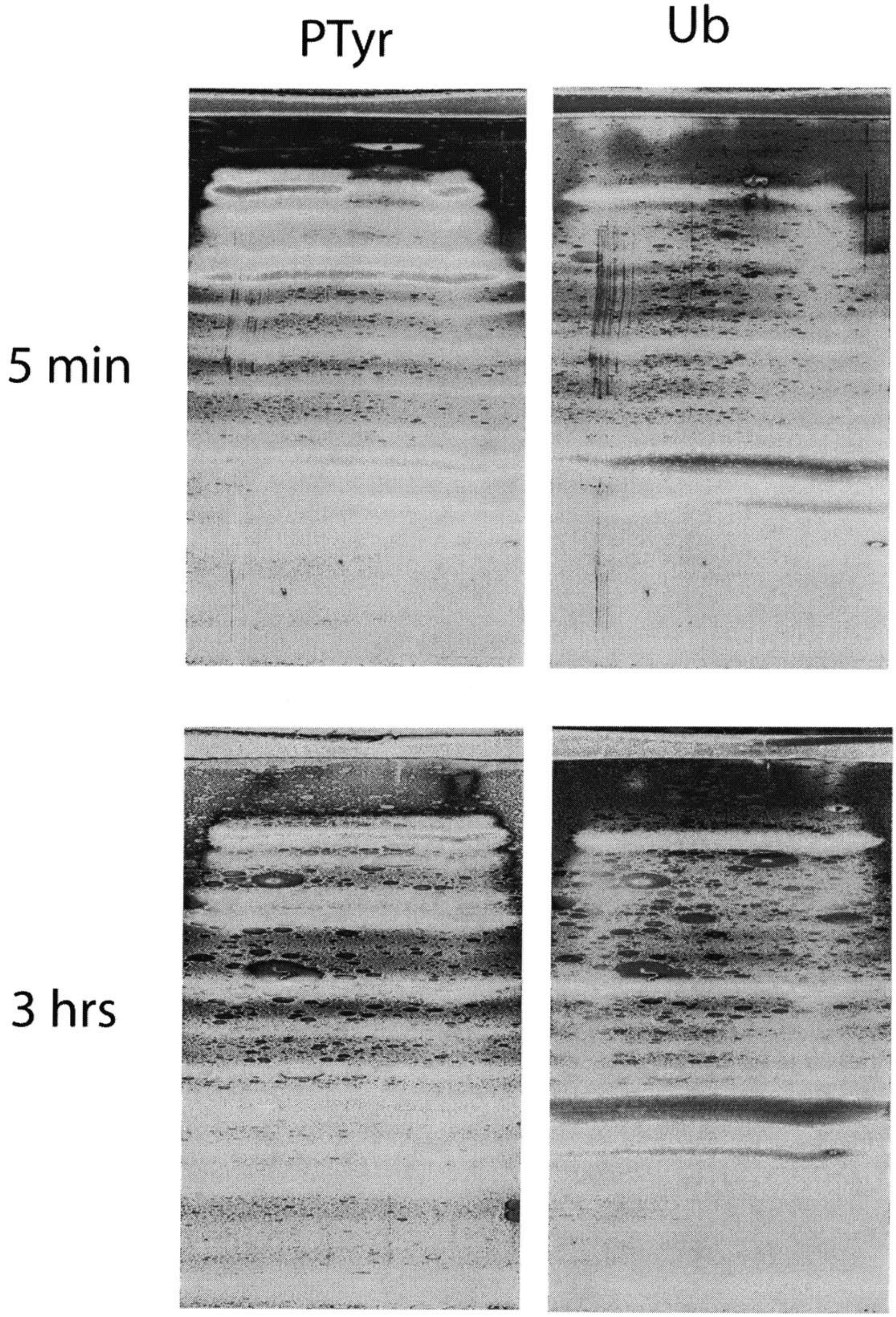

Figure 18: Processed Images

Raw images are filtered, and displayed with color/intensity map for each channel.

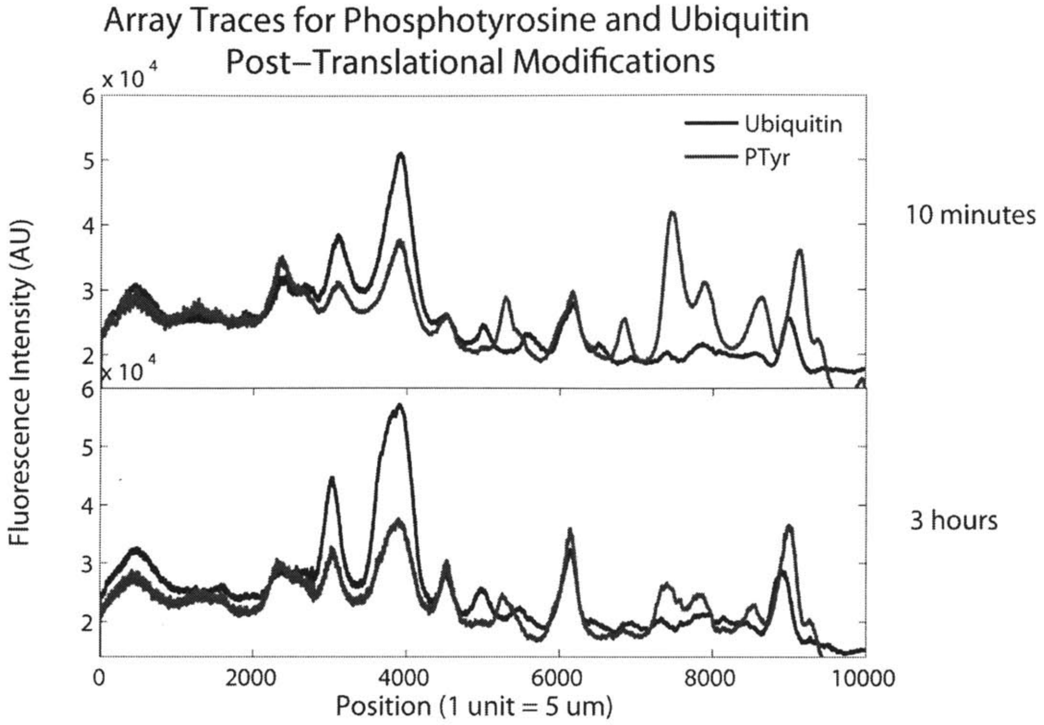

Figure 19: Averaged Traces for Post-Translational Modifications

The slide images were averaged (across each channel). The highly expressed phosphorylated proteins are easily seen. Furthermore, proteins that are also modified with Ubiquitin can be visualized.

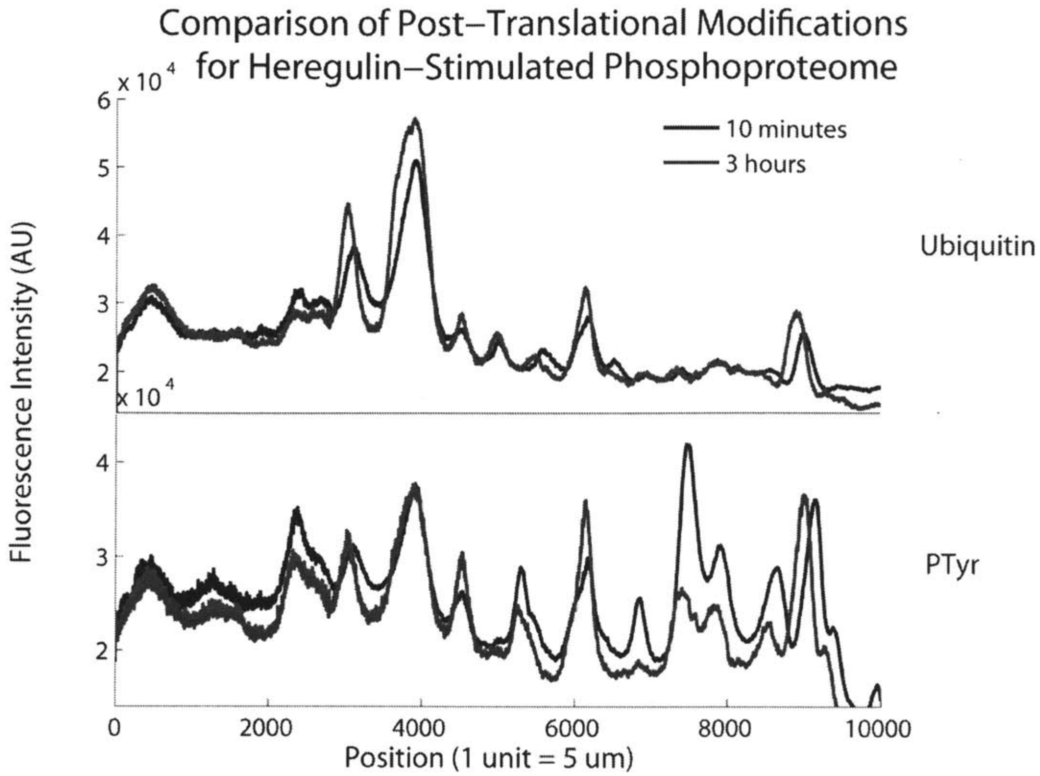

Figure 20: Direct Comparison of Post-Translational Modification States
The states of both the phosphoproteome, as well as proteins with the additional modification of Ubiquitin, are directly compared across short and long term exposure to Heregulin. Each trace contains the sum of the expression of the control and of the treated state.

References

Gygi SP, R. B., Gerber SA, Turecek F, Gelb MH, Aebersold R (1999). "Quantitative analysis of complex protein mixtures using isotope-coded affinity tags." Nature Biotechnology **17**(10): 994-999.

Mann M, O. S., Grønborg M, Steen H, Jensen ON, Pandey A. (2002). "Analysis of protein phosphorylation using mass spectrometry: deciphering the phosphoproteome." Trends Biotechnology **20**(6): 261-268.

Mann, S.-E. O. a. M. (2007). "A practical recipe for stable isotope labeling by amino acids in cell culture (SILAC)." Nature Protocols **1**: 2650-2660.

Niroshan Ramachandran, E. H., Bhupinder Bhullar, Samuel Eisenstein, Benjamin Rosen, Albert Y. Lau, Johannes C. Walter, Joshua LaBaer (2004). "Self-Assembling Protein Microarrays." Science **305**(5690): 86-90.

Ong SE, B. B., Kratchmarova I, Kristensen DB, Steen H, Pandey A, Mann M. (2002). "Stable isotope labeling by amino acids in cell culture, SILAC, as a simple and accurate approach to expression proteomics." Molecular and Cellular Proteomics **1**: 376-386.

Chapter 4: Design and Testing of a CMOS μArray Reader

Goals and Motivation

Optical detection of biological samples provides the foundation for many biological assays. A variety of biological techniques center on luminescence (luciferase assays), fluorescence (GFP, antibody labeling), and absorption (quantification, identification of DNA and Protein) – based assays. Unfortunately, current imaging technologies can be extremely expensive (limiting their use), and cannot be used in combination with fluidic environments where most biological samples exist and function. A sensitive, versatile light-sensing platform can be used in all of these areas, each encompassing a myriad of biological techniques. The application of current imaging techniques to biological applications falls short in two main categories: (1) imagers are remote: they cannot directly interface with the sample as the sample is often in a fluidic environment, (2) imaging is a serial process, hindering the development of high-throughput image-based assays.

The first point (remote imaging) prevents the sensor from directly coupling with the biological process, whether it be integrated in the cellular environment, or in the in-vitro assay itself. This directly lends itself to implantable and *in-vivo* assays. Additionally, a direct interface would allow higher sensitivity (by being close enough to gather all photons) and mitigate the need for optics. The main hurdle to this is the ability to place an imager in solution, and reduce the cost such that it can be disposable. The second task centers on developing an imager that can sensitively image in parallel. Current imagers, due to the expense of the CCD, and size of the optics, have a single imager that is moved to different locations. In high throughput assays, all steps are done in parallel until imaging, which must be done serially. Therefore, imaging is the rate limiting step. By developing an imager that can operate in parallel, where each imager can function independently, and the cost is low enough that the imagers can be easily scaled, imaging will no longer be the bottle neck for high throughput screening. This will enable large drug libraries to be screened faster, cheaper and more efficiently than with current technology.

In summary, the goals of the imager are:

- High Sensitivity
- Low Cost
- Compatible with Fluids
- Parallel Imager

Design Requirements

These goals necessitate a set of design requirement

Table 3: Design Goals

Goals	Technical Requirements
High Sensitivity	Detection of 10^{-6} lux (0.004 photons μm^{-2} s^{-} (Eltoukhy 2006))(for high sensitivity microarray applications)
Low Cost	Silicon based imager manufactured in a standard process and the elimination of optics.
Fluidic Compatibility	Wireless Interface: Allows imager to be completely sealed.
Parallel Imager	Each imaging element should be completely independent (i.e. integration time) and operate in parallel with all other imagers in array. Imager prototype should be scalable to arbitrary number of pixels.

To illustrate the utility of a sensor that encompasses these qualities, we will develop a µarray imager for use with DNA, protein and small molecule arrays.

Technical Requirements

Low Cost: Imager

In order to implement a wireless, low cost imaging sensor we utilize the CMOS (Complementary Metal Oxide Semiconductor) platform. This silicon-based technology platform is used in to manufacture all integrated circuits, covering everything from computer processors to cellular phones. Using this technology, the designer can implement virtually any computation function on-chip. Furthermore, the native manufacturing process lends itself to integrated optical sensors using exposed diodes. Therefore, we can integrate both the sensor and data analysis hardware directly on the same chip, developing a truly integrated lab-on-a-chip.

Additionally, we can integrate a wireless interface directly on chip, with an on-chip inductor, rectifier and voltage regulator as well as data transmission circuitry.

Low Cost: Optics

In order to realize both the low-cost and parallel imaging aspects, the requirement of optics must also be eliminated. This can be accomplished by placing the imaging array directly next to the sample, creating an effective numerical aperture by gathering photons before they spread. In order to enable this, packaging and bond wires must be eliminated, also necessitating a wireless interface.

The first figure shows the (MATLAB simulated) amount of light received on all pixels from a single array spot at two distances, 100 um and 500 um. The farther the array is from the surface, the less light is received, and the more spread out the light is on the imager. The second figure shows the light received from a single array spot on the pixel directly above it (blue) and the neighboring pixel. The signal to background ratio grows as the imager comes closer to the surface, reaching a value of 30 for 25 um.

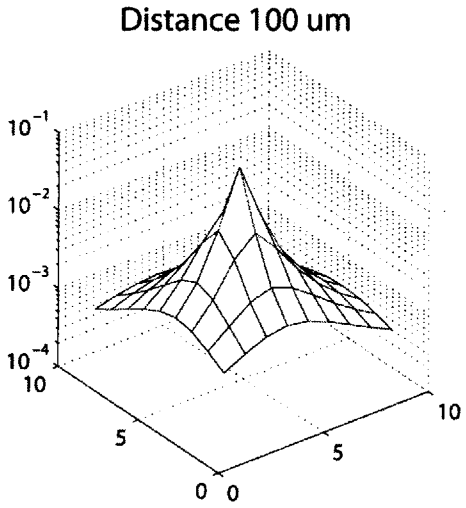
Distance 100 um

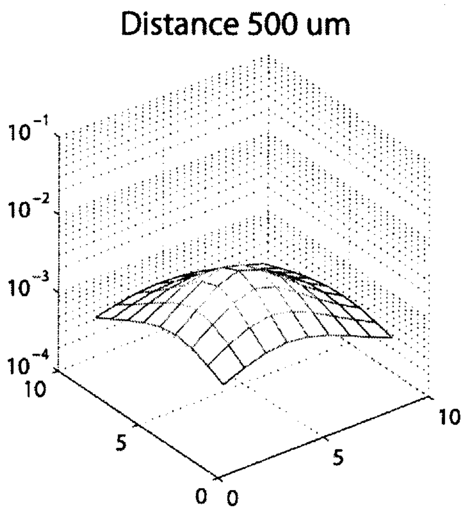
Distance 500 um

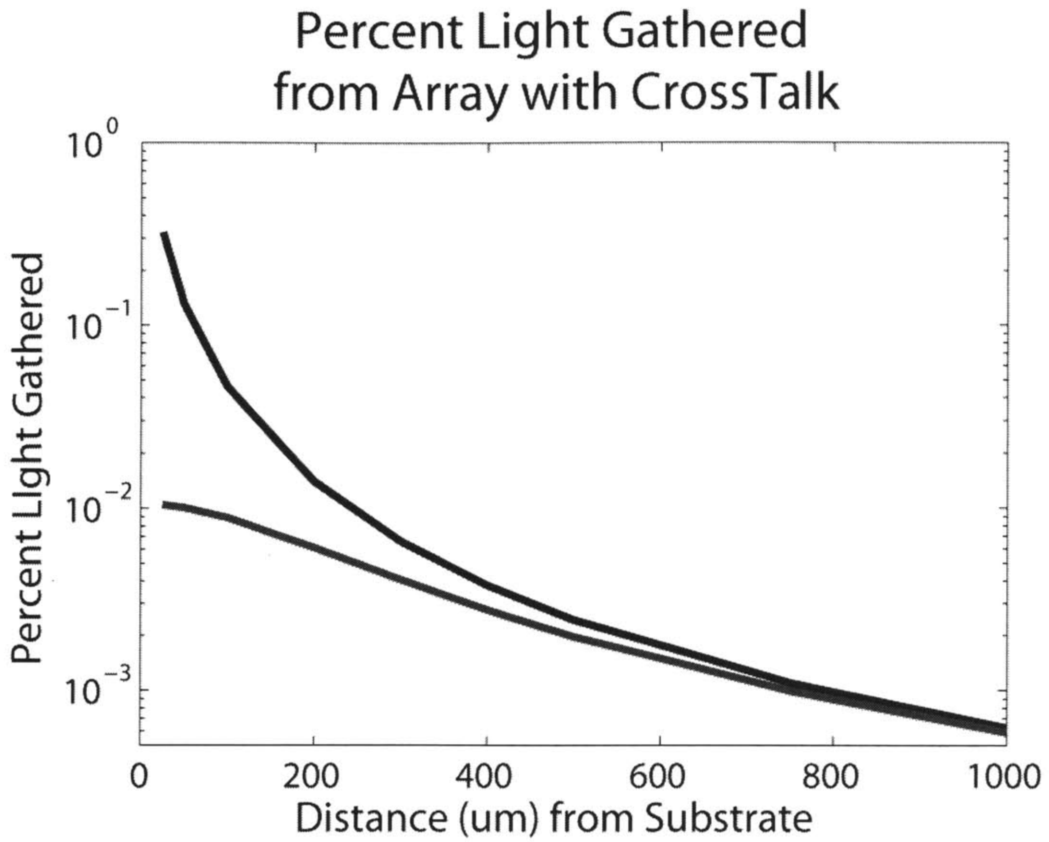

Figure 21: Effective Numerical Aperture Versus Distance

The plot shows the effect of distance of the reader from the surface of the array. As the reader gets closer to the surface, more light is received, and greater spatial resolution is achieved. .

Optical Filters

The need for optical filters can be eliminated by using the native optical selection of silicon. Short wavelengths are absorbed very close to the surface, while longer wavelengths penetrate deeper. This is quantitatively described by the absorption coefficient, shown in **Figure 22**, where the number of photons present at a given depth, *x*, is given by

$$I_{ph}(x) = I_{ph}(0)\exp\left(-x/\alpha\right)$$

where α is the absorption coefficient. A photon creates current in silicon by generating electron-hole pairs. The electrons and holes then diffuse and recombine. If an electron-hole pair is generated in a region of high electric field, they will be swept in opposite directions and generate a current. Therefore, electron-hole pairs generated in the depletion region of a p-n junction diode (i.e. a photodiode) will generate a photocurrent. The depth of the junction dictates how efficiently a given wavelength of light will be converted to electrons (i.e. the quantum yield). By choosing a photodiode with a junction depth of ~ 1um, light between the wavelengths of 500 to 800 nm is readily absorbed, while deep UV light of 200-300 nm is absorbed at the surface and does not penetrate to the junction depth. Therefore, by illuminating with ultraviolet light, and detecting emitted around 600 nm, the silicon-based imager can detect fluorescence without the need for optical filters.

The shift between absorbed light and emitted light is called the Stokes shift. For most fluorophores, this shift is on the order of 30 nm. Quantum dots are fluorescent particles whose emission spectra is governed by their physical size. Consequently, they are able to absorb any wavelength of light with a higher energy (shorter wavelength) than their emitted light, and emit light at a specified wavelength. This can lead to a Stokes shift of several hundred nanometers or more. For our purposes, we will illuminate with ultraviolet light at 280 nm, and detect light emitted in the visible spectrum (~ 600 nm).

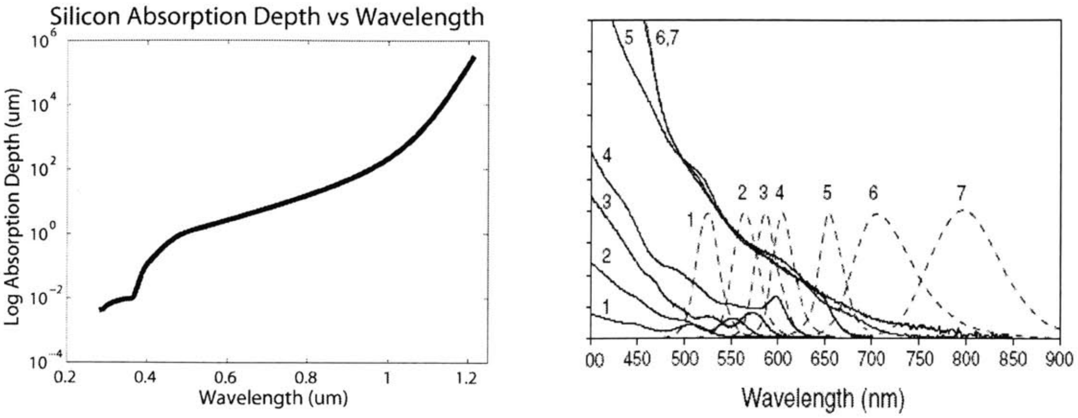

Figure 22: Silicon Absorption Coefficient and Q-dot Spectral Shift

(A) The absorption coefficient for silicon as a function of wavelength. Short wavelength (i.e. ultraviolet) light is absorbed (creating electron – hole pairs) near the surface, while longer wavelength (i.e. IR) can penetrate much further. (B) Qdots emit at a specific wavelength dictated by their physical size, regardless of the illuminating wavelength. Furthermore, the higher energy (shorter wavelength) the light is, the more readily they absorb.

Sensor Design

Design Characteristics

The goal of the design is to develop an optical sensor that is highly sensitive and suitable for microarray applications. The level of light will be on the order of the dark current. As described in the Sensor Design, each pixel will be a 1:1 match with a spot of DNA or Protein (~ 120 um in diameter). The available choices for photodiodes are shown in **Table 4: Diode Characteristics**.

Table 4: Diode Characteristics

Diode Type	Area Leakage (fA / um^2)	Perimeter Leakage (fA / um^2)	Leakage for 14,400 um^2 Diode (fA)	Junction Depth (um)	Capacitance for 14,400 um^2 Diode (pF)
N+ / Psub	0.01	0.25	264	0.18	13
N - / Psub	0.002	0.01	76.8	1.05	1.8
P + / N -	0.01	0.15	216	0.2	14.4

Pixel Architecture

The pixel architecture we chose is a standard active pixel sensor (APS) architecture, shown in **Figure 23**. This allows for the lowest power per pixel, and simplicity in operation. The downside is that the since the parasitic capacitance is scaled with the area, the gain of the signal is fixed (although the noise will decrease with increasing area). The operation of the pixel is as follows: The NMOS *Reset* transistor charges up the Photodiode (and parasitic capacitor) to $V_{DD} - V_t$. Photons, impinging on the reversed-biased photodiode generate a photocurrent, which drains charge from the parasitic capacitor. The voltage on across the photodiode is buffered by a source follower and fed into an amplifier or analog to digital converter.

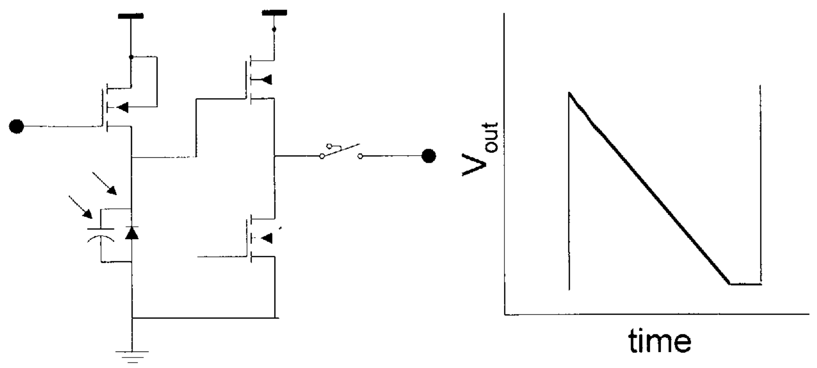

Figure 23: Standard CMOS Pixel Topology

In a standard CMOS architecture, the photodiode is reset by a transistor, and the output is buffered by a source follower. Incident light generates a photocurrent which drains charge form the parasitic capacitance of the photodiode, causing the voltage to drop. The reset transistor then can activate and raise the voltage back to V_{dd}.

$$V_{ph}(t) = V_{RST} - \frac{1}{C_{ph}} \int_0^{t_{\text{int}}} \left(I_{ph}(t) + I_{drk}\right) dt$$

The greatest signal will be generated by the photodiode witht eh lowest capacitance and dark current. For this reason we chose the Nwell - Psub diode. Alternatively, a resistor can replace the reset transistor (or in fact be the reset transistor) in which case the signal will be

$$V_{ph}(t) = V_{RST} - R_{RST}\left(I_{ph}(t) + I_{drk}\right)$$

A principle draw back of CMOS based imagers is the large dark current. In order to reduce the dark current, we implement a differential pixel, whereby one pixel is covered by metal and only generates the dark current, and the signal pixel has both the dark current and photocurrent. Ideally, the dark currents of each pixel are identical, and the differential signal represents only the photocurrent. In reality, mismatch between the two pixels (in size, doping, and capacitance) will result in the dark currents not being equal[1]. A conservative estimate will allow the mismatch in dark currents to be less than 5% of the dark current.

Additionally, the wireless interface will introduce a significant AC signal in the power supply and reference voltages generated on chip. In order to achieve a high power supply rejection ratio, a fully differential architecture will be implemented.

We also modify our pixel design to mitigate the traditional drawbacks of the standard CMOS pixel design, namely image lag (due to the reset transistor entering subthreshold during reset) and the loss of headroom. We implement the reset transistor as a PMOS instead of the traditional (area-saving) NMOS. Furthermore, to reduce charge injection and clock feed-through a dummy transistor of ½ size is mirrored to the reset transistor, and controlled by an

---

[1] Mismatch in size will not be a large contributor to the error because the ratio of dark current to capacitance will remain constant.

inverted reset signal. Finally, to reduce the leakage current as much as possible, the reset transistor is biased into accumulation by generating a separate bias for the bulk of the PMOS transistor which is several threshold voltages lower than the power supply. The schematic and layout of the pixel is shown in **Figure 24**. Due to the power restrictions of the wireless interface, only one amplifier is implemented on chip. Therefore, all pixels must be addressed serially by the amplifier and analog to digital converter. We enable two different modes of operation (selectable by cutting a top metal trace): a sampling mode whereby each pixel integrates during the same time period, and the integrated voltage is sampled onto a hold capacitor, and a continuous time readout, whereby each pixel outputs its current value.[2] The overall pixel design and layout is shown below.

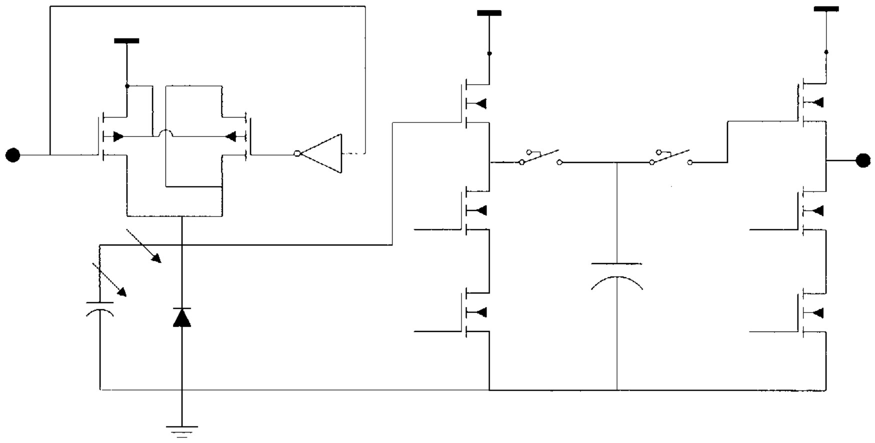

---

[2] There is also a selectable option on chip to deactivate the amplifier and connect the pixel output directly to the analog to digital converter for extremely low power operation.

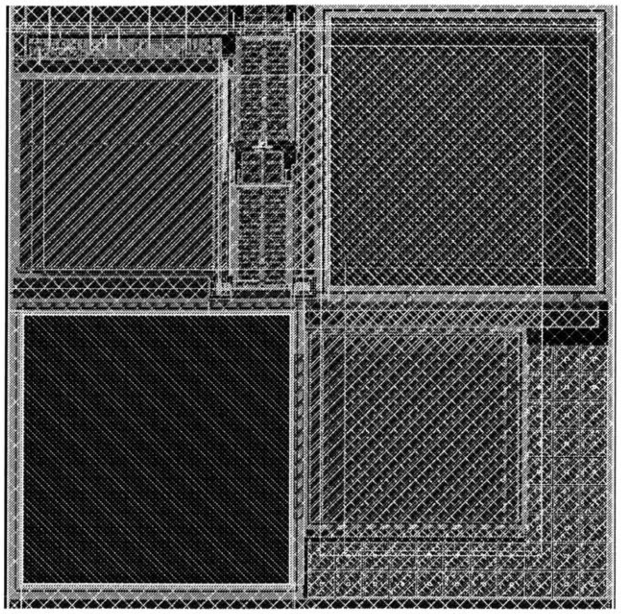

Figure 24: Pixel Design and Layout

The modified pixel design, with PMOS reset, and sample and hold. The layout is also shown, with one photodiode covered in metal.

Chip Operation

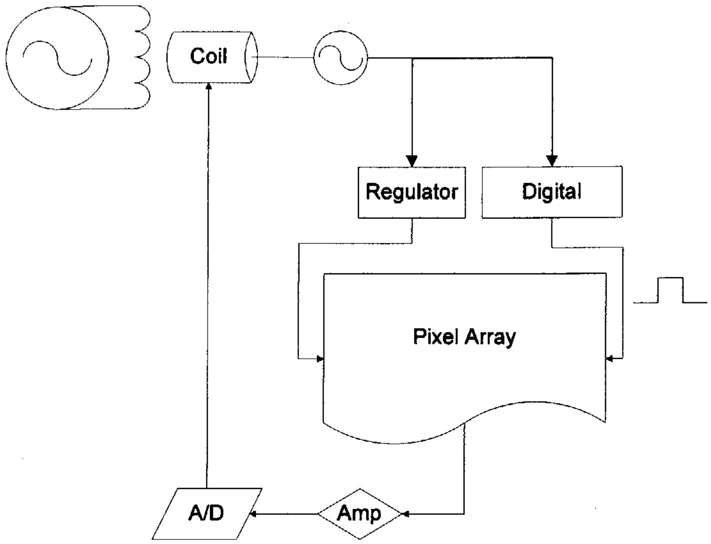

Figure 25: Circuit Operation

The overall operation of the chip (shown in **Figure 25**) is as follows. The transmitter coil sends an RF signal which is picked up by the on-chip inductor coil. This signal is rectified, and fed into a voltage regulator which supplies the power on-chip and reference voltages. The RF signal is also used to generate the digital clock, and all timing signals are derived from dividing down this clock (via D-flip-flops). The digital logic includes a decoder which serially activates each pixel for readout and connects it to the amplifier and analog to digital converter. The amplifier is a simple resistively loaded amplifier, and the analog to digital converter is a single slope converter. Each pixel is allowed to integrate until the amplifier saturates (or the common mode pixel voltage goes below a set threshold). When these limits are exceeded, the pixel is reset. This enables each pixel to set its own integration time. The analog to digital converter operates by sampling the amplifier output onto a capacitor, and then integrating current on the capacitor until the threshold voltage of an inverter is reached.

When this voltage is crossed, the value of the digital clock (12 bits) is latched into a parallel-load, serial readout register. The output is then modulated at ½ the clock frequency, and sent out on the RF coil.

The chip can operate in two modes (set by cutting a trace on the chip): simultaneous sampling and continuous sampling. In simultaneous sampling, the amplifier is deactivated while the first source follower on all pixels is activated. This samples the photodiode voltage onto the hold capacitor. During each CKSMPL = High, the second source follower of the selected pixel is turned on, and the voltage on the hold capacitor is read out, amplified, and sampled onto the analog to digital converter capacitor. When CKSMPL = Low, the source follower is shut off, and the current is integrated onto the analog to digital converter capacitor.

In continuous mode, the operation is identical except that the first and second source followers are activated at the same time on each pixel that is activated. The timing diagrams for two pixels in each scheme are shown in **Figure 26**.

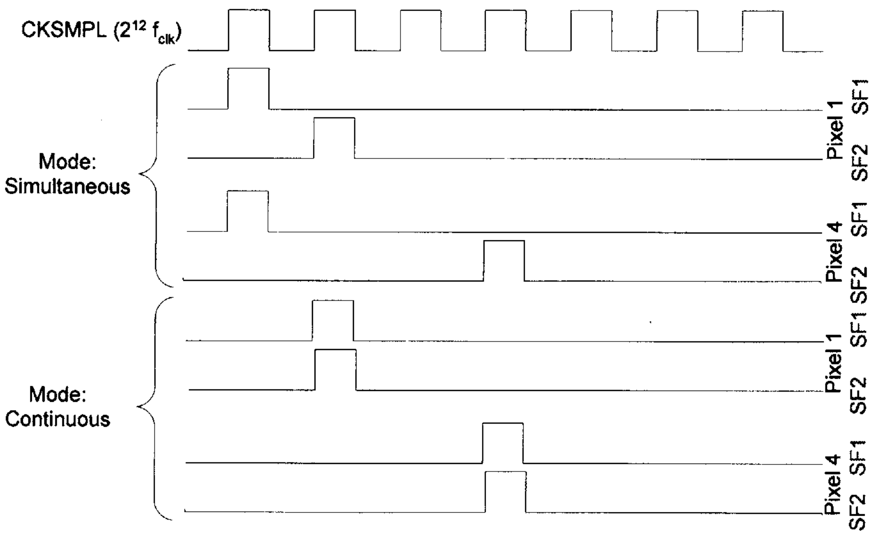

Figure 26: Pixel Timing Diagram

Amplifier

The amplifier consists of two serial, fully differential, amplifiers, each having PMOS input FETS and resistively loaded. The lack of feedback allows the amplifier to achieve a high gain and speed and low power consumption, at the cost of linearity. The output data is linearized by using the mismatched dark current as a constant current source, and sweeping the differential input voltage. This is discussed in more detail in subsequent sections.

Analog to Digital Converter

The analog to digital converter is a single slope converter. Since the analog to digital converter can only integrate for a maximum time set by an integer number of clock cycles, a constant current source will only be valid for a small range of frequencies. To allow for a wider variety of clock frequencies (i.e. integration time, and therefore dynamic range), we use a current source that is proportional to the clock. This is generated by using a switched capacitor current source, using the on-chip clock.

Wireless Interface

The wireless interface to this sensor is designed to receive power, generate the digital clock, and transmit data. We accomplish this using several metal layers to form an on-chip inductor. Furthermore, to isolate the noise of the digital circuitry from the analog circuitry, we implement two separate power supplies, each with its own inductor. The power supply consists of the inductor with a full wave rectifier, which then feeds into a voltage regulator. Bias currents and reference voltages are also generated. The clock is generated from the RF wave.

Digital Circuitry

The clock and timing circuitry is developed by generating the clock signal from the RF signal received on the inductor. This allows the clock to be controlled externally. The timing circuitry is generated by dividing the clock circuitry. The amplifier and analog-to-digital converter are cycled to each pixel by means of a decoder. The digital output is then modulated at $f_{clk}/2$, and sent out via the inductor coil

Detailed Design

The size of the photodiode is set by the μarray spots at ~ 120 μm in diameter, with a pitch of ~ 240 μm. Using an Nwell/Psub photodiode gives us a dark current of 78 fA and a capacitance of 1.8 pF.

We begin by attempting to set the resolution limit to that of the noise of the dark current. The noise generated by an integrating current is

$$V_I\left(t_{\text{int}}\right)=\frac{\sqrt{2q_e I t_{\text{int}}}}{C_{pd}}$$

(Since we are continually integrating, the reset noise appears only as an initial offset and can be factored out by subtracting subsequent output signals from the initial reset signal.) The pixel design uses a source follower to buffer the photodiode voltage, and an additional source follower to buffer the sampled output. Therefore the sources of noise from the signal to the output are: Integration noise V_{int} , source follower noise (x 2) v_{sf}, amplifier noise v_{amp}, and quantization noise v_q. The noise from each of the sources is described below.

The signal generated (assuming a constant signal) is

$$V_I\left(t_{\text{int}}\right)=\frac{I t_{\text{int}}}{C_{pd}}$$

The noise and gain for the source follower is

$$v_{sf}^2=\frac{2q_e i_{sf}}{g_m^2}$$

$$A_{sf} = \frac{1}{1 + g_m / g_{mb}}$$

The input-referred noise of the amplifier of a resistively loaded amplifier can be written as

$$v_{nRl}^2 = \frac{4\kappa_B T R_l}{A_v} = \frac{4\kappa_B T}{g_m}$$

$$v_{nFET}^2 = \frac{2}{3}\frac{4\kappa_B T}{g_m}$$

$$v_{amp}^2 = v_{nRl}^2 + v_{nFET}^2$$

The gain of the amplifier is given by

$$A_v = g_m R_l$$

Where

$$g_m = \frac{\partial I_D}{\partial V_{gs}} = \frac{2I_D}{V_{DSAT}}$$

This is valid for the region where $V_{GS} - V_T > V_{DSAT}$. The minimum noise for the amplifier can be achieved using the maximum g_m , translating to using the maximum available current. Since we are power limited, we restrict the amplifier to $40\mu A$. The common mode output voltage is given by $V_{CM} = V_{DD} - I_D R_l$, placing an upper limit on R_l, restricting the gain. A solution to this is to have two gain stages of equal gain. The first stage will have a high current to reduce noise, and the second stage will have a low current (but high output resistance) to provide additional gain at a minimal power cost. In order to further maximize the transconductance, the input FETS are large PMOS mosfets, which also reduce noise and amplifier offset. A schematic for the amplifier is shown in **Figure 27**.

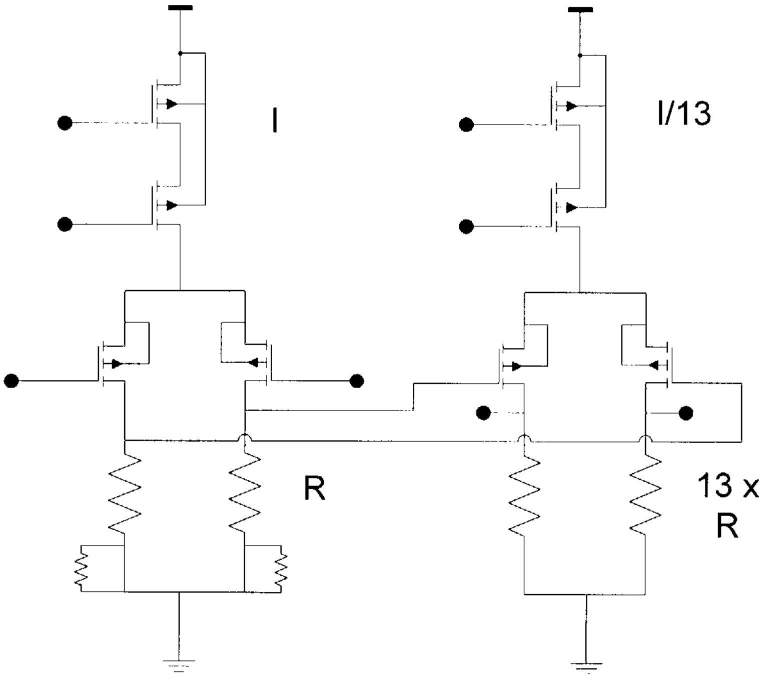

Figure 27: Amplifier Schematic

The condition for the current can be written as

$$I_{tot} = 2\times\left(A_v\alpha + \alpha\right)\times 10^{-6}A$$

where α is the unit current through each branch of the amplifier. We can then write the equations for the gain and common mode output in terms of α:

$$R_l = \frac{V_{CM}}{\alpha}$$

$$g_m = g_{m0}\times\alpha$$

For the first amplifier

$$A_v = g_m\left(A_v\alpha\right)\times R_l\left(A_v\alpha\right)$$

For the second amplifier

$$A_v = g_m\left(\alpha\right)\times R_l\left(\alpha\right)$$

g_{m0} is chosen to be 26.6 μS based on process parameters and an iteratively chosen optimum size (size limited by being in saturation with a given current). The equations can then be solved for the following parameters.

Table 5: Amplifier Parameters

Parameter	Value
α	1.4
g_{m0}	$26.5\mu S$
V_{CM}	$0.5V$
R_{l1}	$350k\Omega$
$A_{v\{1,2\}}$	13.3
R_{l2}	$27k\Omega$
g_{m1}	$500\mu S$
g_{m2}	$38\mu S$

In order to find the optimum integration time and amplifier bandwidth, we consider the noise of the system. The input referred noise of the amplifier can be written as

$$v_{ampTOT}(\alpha)^2 = v_{amp}(A_v\alpha)^2 + v_{amp}(\alpha)^2$$

where $v_{amp}^2(\alpha) = \frac{5}{3}\frac{4\kappa_B T}{g_{m0}\alpha}$.

The noise of the system can be reduced by limiting the bandwidth. This has the adverse effect of making the settling time longer, and therefore increasing the settling error. In order to ensure that the settling error does not contribute to the overall noise, the following condition must be met:

$$V_R\left(1-\exp\left(\frac{-t_s}{\tau}\right)\right)<V_{amp}\sqrt{\frac{\pi}{2\tau}}$$

Where V_{amp} is the output—referred noise density, τ is the amplifier time constant, and V_R is the output swing of the amplifier. This condition ensures that the settling error is less than the integrated noise of the amplifier. The quantization noise of the analog to digital converter is then set by making it lower than the total integrated output noise of the system.

The input referred noise of the entire system (excluding the analog to digital converter) can be written as

$$v_{IR}(\alpha,t_s)^2=\frac{v_{ampTOT}(\alpha)^2\,\frac{B(\alpha,t_s)}{2}+v_{set}(\alpha,t_s)^2+V_Q^2}{A_{vTOT}^2}+V_{\text{int}}(2n_{pix}t_s)^2+\left(\frac{V_{sf}^2}{A_{sf}^2}+\frac{V_{sf}^2}{A_{sf}^4}\right)\frac{B(\alpha,t_s)}{2}+\frac{V_n^2}{A_{sf}^2}$$

where $B(\alpha,t_s)$ is the bandwidth of the amplifier and $v_{set}(\alpha,t_s)$ is the settling error. The optimum bandwidth (or amplifier time constant) is found by minimizing the total output noise including settling error:

$$\frac{\partial}{\partial\tau}\left(v_{ampTOT}{}^2\,\frac{\pi}{2\tau}+V_R^2\exp\left(\frac{-t_s}{\tau}\right)\right)=0$$

The solution to this equation is

$$\tau(\alpha,t_s)=\frac{-t_s}{\ln\left(\frac{v_{ampTOT}(\alpha)}{V_R}\sqrt{\frac{\pi}{4t_s}}\right)}$$

and

$$B(\alpha,t_s)=\frac{\pi}{2\tau(\alpha,t_s)}$$

$v_{set}(\alpha,t_s)$ can be described as

$$v_{set}(\alpha,t_s)^2=V_R^2\exp\left(\frac{-t_s}{\tau(\alpha,t_s)}\right)$$

Although the reset noise dominates all other noise sources, we do not include it because we allow a continual integration and readout, where by we can subtract subsequent values from each other, thereby eliminating the static reset noise. Additionally, it should be noted that the noise can be reduced by averaging results. Therefore, a shorter integration time allows more samples in a given period. Since the signal to noise ratio increases as the root of the number of samples, we assign a figure of merit to our input noise:

$$v_{IRFOM}^2 = v_{IR}\left(\alpha, t_s\right)^2 \sqrt{\frac{t_s}{t_0}}$$

Using these criteria we can determine the values for the components of our system. To determine the optimum α and t_s, these equations are iteratively solved and the resulting parameters are shown below in **Table 6**.

Table 6: Amplifier Parameters

Parameter	Value
α	1.4
g_{m0}	$26.5\mu S$
V_{CM}	$0.5V$
R_{I1}	$350k\Omega$
$A_{v\{1,2\}}$	13.3

R_{l2}	$27k\Omega$
g_{m1}	$500\mu S$
g_{m2}	$38\mu S$
C_{A2D}	$37pF$
τ	$13\mu s$
A_{sf}	0.84
A_v	88
t_s	$0.125ms$

With these parameters, the (input-referred) noise calculations are shown in **Table 7**.

Table 7: Noise

Parameter	Noise Density	Integrated Noise
v_{amp}	$22\frac{nV}{\sqrt{Hz}}$	$2.2\mu V$
v_{sf}	$14\frac{nV}{\sqrt{Hz}}$	$2.7\mu V$
v_{sf}	$12\frac{nV}{\sqrt{Hz}}$	
V_Q		$5.5\mu V$

V_{int}	$6.8\mu V$

Power Supply

The power supply for the circuit utilizes an on-chip inductor, fabricated from metal 3 to metal 5, with approximately 20 turns, and a 3.5 mm diameter. Using an on-chip inductor allows for a fully integrated solution, reducing cost and simplifying packaging. Additionally, it eliminates the need for bond wires to an external inductor. Unfortunately, the inductor characteristics are extremely poor. The coil has a very high impedance (~ 1.5 kOhm) and a high parasitic capacitance. The effects of these can be seen when looking at the model for the inductor, shown in **Figure 28**. The high coil resistance acts as a resistive divider for the circuit, and the high capacitance results in coupling to the substrate, further diverting power from the circuit.

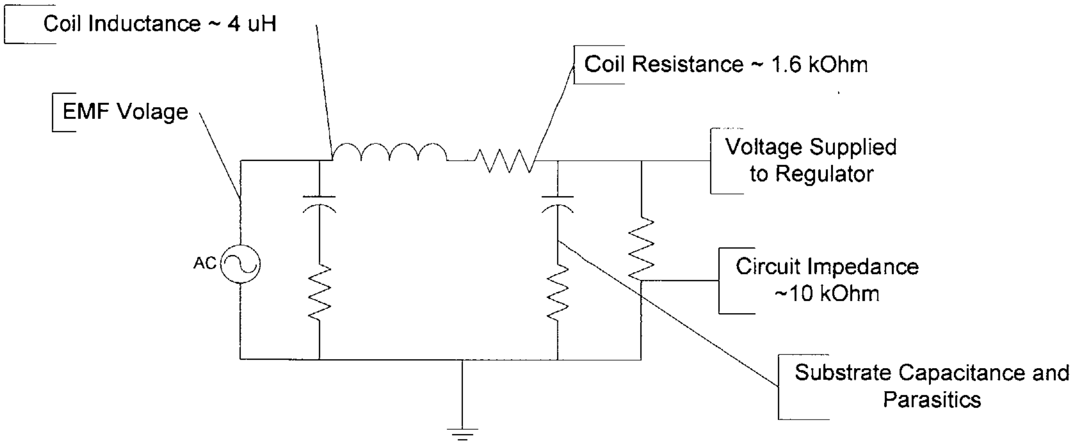

Figure 28: On-Chip inductor properties

The coil connects to a half wave rectifier (**Figure 29**), which then supplies a voltage regulator. The rectifier consists of an P+/NWell diode, which feeds onto a poly-poly capacitor as well as a high-voltage NMOS capacitor. The poly-poly cap allows the voltage to build up until the regulator is greater than the threshold voltage of the NMOS capacitor.

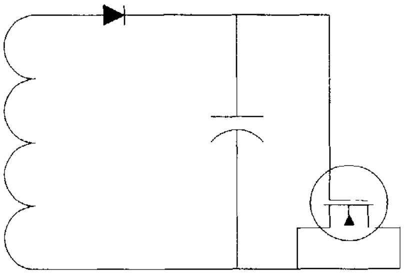

Figure 29: Rectifier

The output of the rectifier feeds into the voltage regulator. The regulator consists of a bias tree, which provides the pixel reset voltage and the regulator bias. The pixel is biased independently of the regulated voltage to put the transistor into accumulation in order to reduce leakage. The regulator is designed to provide a voltage of about 1.6V. The schematic is shown in **Figure 30**.

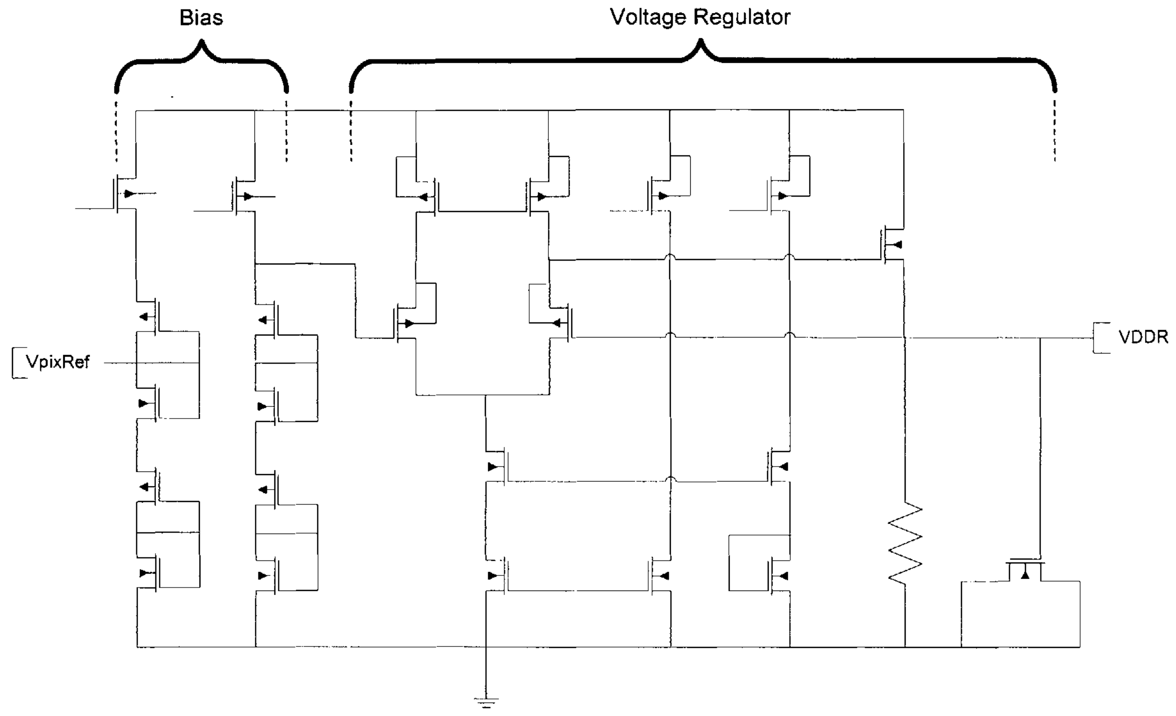

Figure 30: Voltage Regulator

Figure 31 shows the regulator voltage as a function of AC voltage (from 0 to 2*Amplitude). The regulator keeps the voltage at approximately 1.6 V when the power received is sufficient, or in excess.

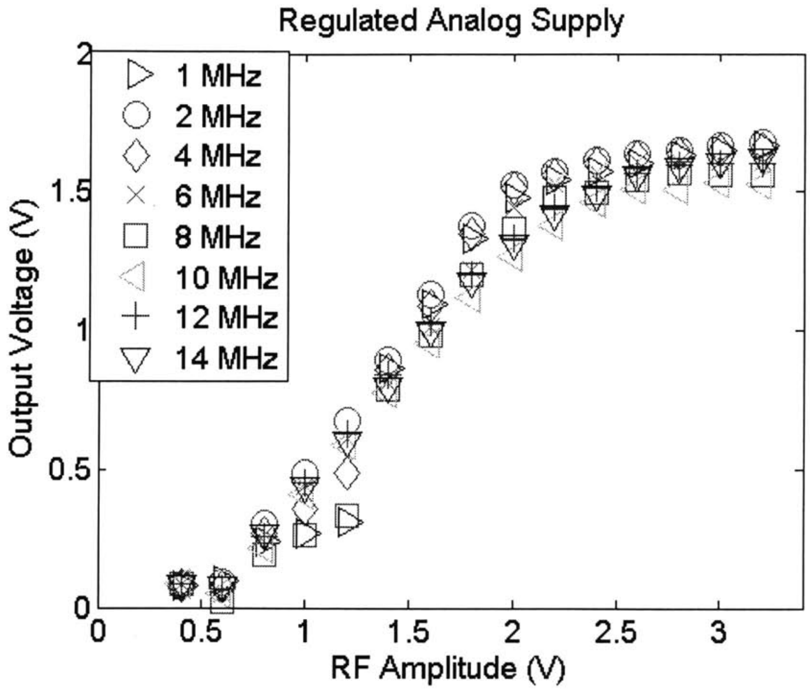

Figure 31: Rectified Voltage Versus RF Amplitude

The on-chip inductor was connected to a function generator and a sine wave of various frequencies and amplitidues applied. The regulated voltage is shown.

The regulated and rectified voltages as a function of RF power (current through transmitting inductor) are shown in **Figure 32**

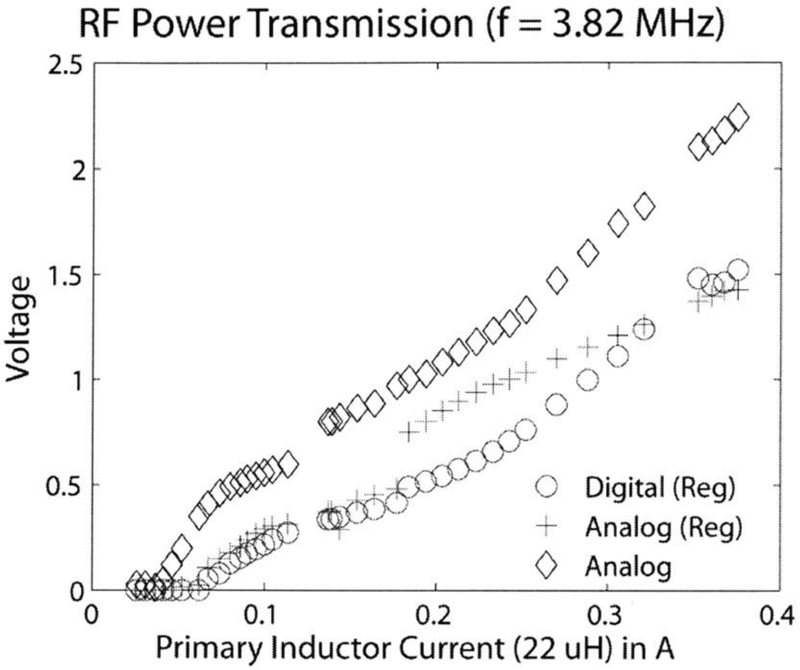

Figure 32: Rectified and Regulated Voltage from Wireless Power Transfer

Analog Response to Light

To observe the analog response to light, we pin out the pixel outputs (V_{out}, V_{out_Ref}), and the amplifier outputs (AmpOut1, AmpOut2). **Figure 33** shows the results. The reference voltage (V_{out_Ref}) stays relatively constant, as the pixel is covered by metal and is shielded from light. The light sensing pixel's output, V_{out}, decreases with time, and is proportional to the intensity of light. [3]

---

[3] The photodiodes parasitic capacitance is not constant, but varies with the reverse bias. This variation is small at the operating reverse bias, and is ignored. The variation occurs because the depletion region width is dependent on the reverse bias voltage. The capacitance can be written as

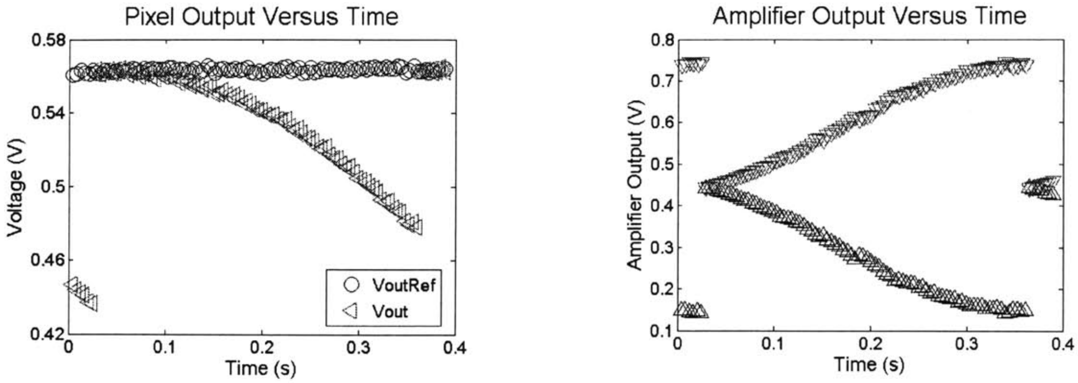

Figure 33: Analog Pixel and Amplifier Output

The amplifier output is non-linear, but the differential value increases with increasing light. The pixel resets when the amplifier output gets more than a few hundred microvolts away from the common mode output. This feature allows the pixel to continue integrating until the amplifier output saturates, ensuring that even for weak signals, the integration time is long enough. Furthermore, the data

---

$$C = \frac{\varepsilon_s}{x_d}$$

$$x_d = \sqrt{\frac{2\varepsilon_s}{q}\left(\frac{1}{N_A} + \frac{1}{N_D}\right)(\varphi_i - V_a)}$$

V_a is the reverse bias voltage, and, assuming that the amount of light is constant, and the conversion of photons to electrons is proportional to the depth of the depletion region, is still output at a constant rate, so that changes in intensity as a function of time can still be acquired.

Digital Output

The analog to digital converter is a single slope converter (**Figure 34**). After sampling the amplifier output onto the capacitor (which also bandwidth limits the noise of the amplifier and source followers), it then charges the capacitor to a threshold voltage level. The time it takes for this charging to occur is then recorded from the global clock. The converter is a 12 bit differential converter, resulting in 2 12 bit output streams. The clock is generated from the input RF signal and is divided down using standard D-flip flops. The clock signal is loaded into a series of registers which then output the information.

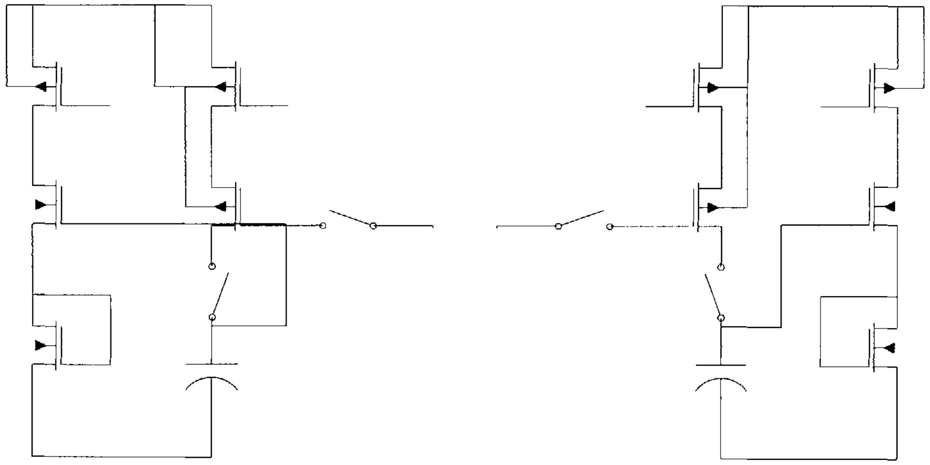

Figure 34: Analog to Digital Converter Schematic

The output of the amplifier is sampled onto the hold capacitor, which, coupled with the output resistance of the second stage amplifier, forms the bandwidth limiting pole of the system. The switch is then opened, and the current source charges the capacitor until it reaches the threshold voltage of the following stage, which connects to a series of inverters. As mentioned earlier, in order to allow variable clock frequencies to be used, the current source is designed to be proportional to the clock frequency. This is accomplished by using a switched-capacitor circuit as shown in **Figure 35**.

In order to increase dynamic range and allow the operation frequency to be selected after circuit fabrication, the analog to digital converter must be made frequency independent. To accomplish this, the bias current is made to be proportional to the clock frequency. The analog to digital integration time is defined by a number of clock cycles:

$$T_{A2D} = \frac{2^{nbits}}{f_{clk}} = \frac{C_{A2D} V_R}{I_{A2D}}$$

Therefore, if the current is proportional to the clock frequency, a change in frequency will not affect the converters dynamic range.

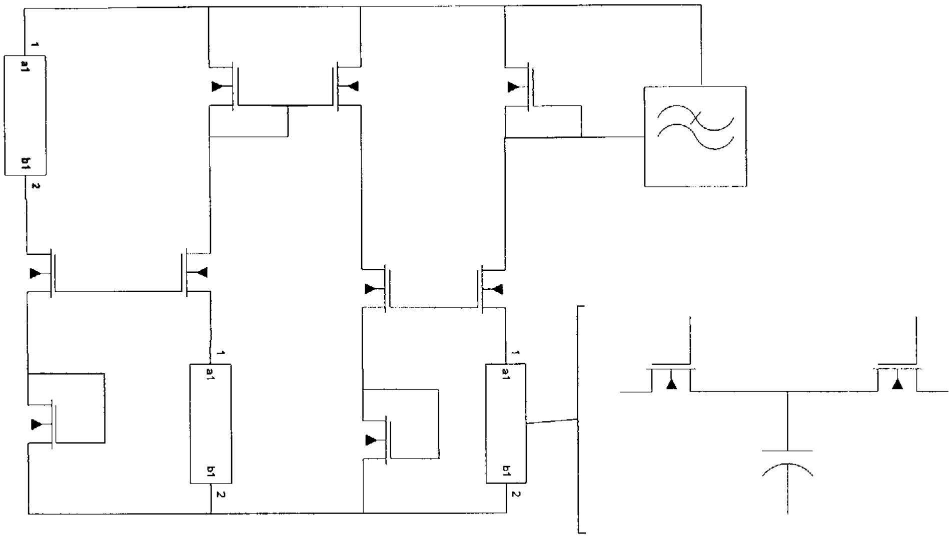

Figure 35: Integrating Current Generator for Analog to Digital Converter

The current is set by charging and discharging a capacitor with the frequency set by the clock frequency. The output bias voltage is low pass filtered through three sequential RC filters, and the current is then mirrored and routed to the analog to digital converter.

The results of the converter are shown below. These results were measured by powering the chip with a 0 to 4V peak-peak sign wave at 1,2,4, and 8 MHz. The results for 1 and 8 MHz are shown below (**Figure 36**), with the residuals from a linear fit.

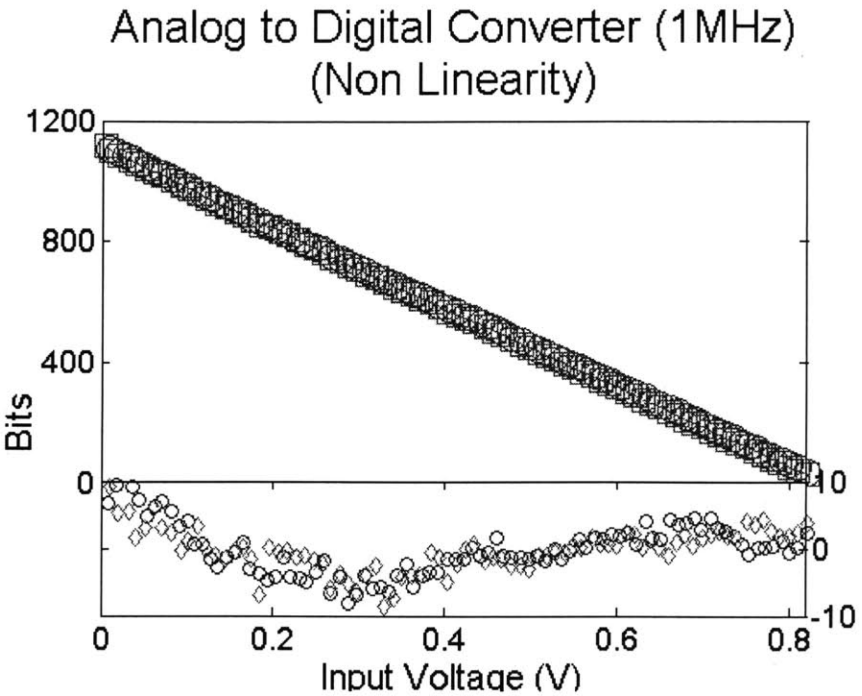

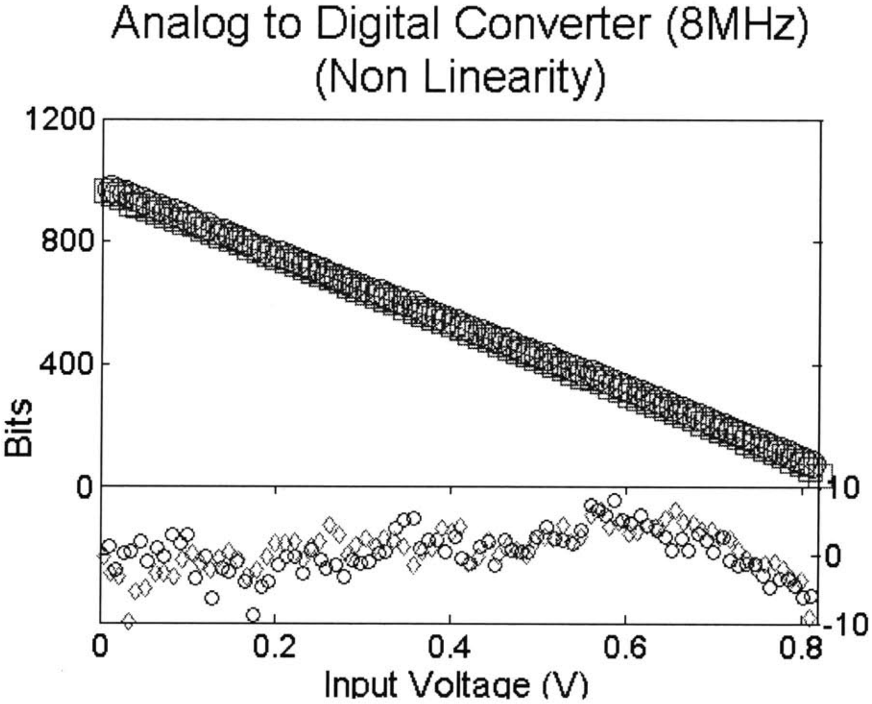

Figure 36: Analog to Digital Converter.

The analog to digital converter output is shown for 1 and 8 MHz, with residuals for a linear fit.

The analog output can be compared to the digital output as shown in **Figure 37**.

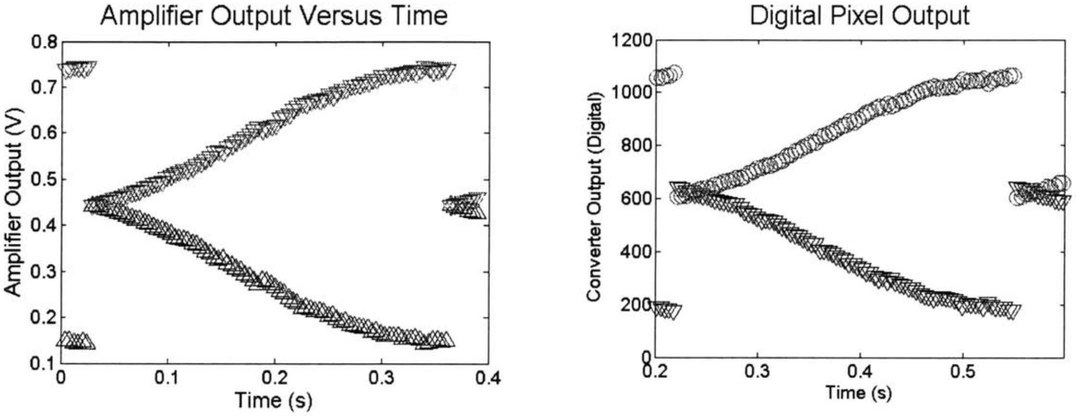

Figure 37: Analog and Corresponding Digital Outputs

Variable integration

One of the key features of the design is the ability for each pixel to define its own integration time. This is accomplished by letting the pixel integrate until the amplifier output (or the pixel value) crosses a threshold voltage. The pixel is then reset. The reset circuitry will reset when the output of the amplifier saturates, or the common mode voltage goes too low. The schematic and resulting output is shown in the following figure .

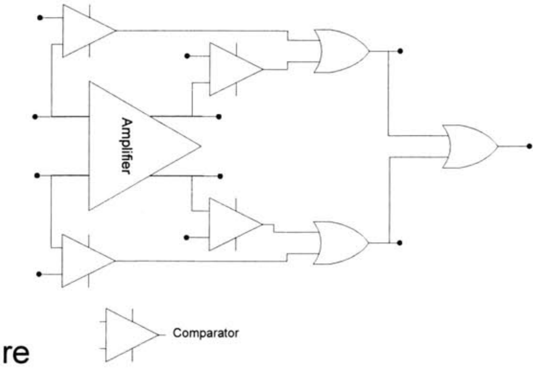

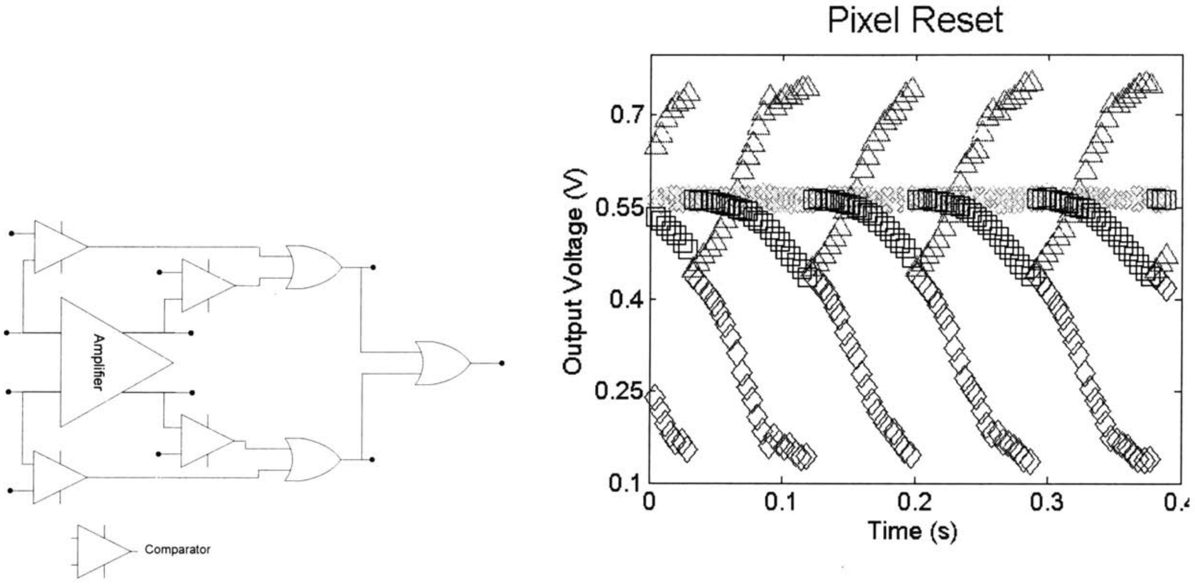

Figure 38: Reset Schematic and Output

Detailed Pixel Operation and Analysis

Photons impinging on the photodiode generate a current. This current is converted to a voltage by passing through impedance, typically either a resistor or a capacitor (**Figure 39**). In the traditional CMOS photodiode architectures, a reset transistor is present in the "off" state ($V_{gs} = 0$), and the photodiode drains current from a parasitic capacitor. The arrangement is in fact an R-C circuit, with a characteristic time constant. The resistance is given by the variation in subthreshold leakage with changing source voltage (for NMOS reset),and the capacitor is typically the parasitic capacitance of the photodiode. When measuring extremely small numbers of photons, the sub-threshold leakage of the transistor is not negligible. When a transistor is in weak inversion the current is given by

$$I_{DS} = I_0 \frac{W}{L} \exp\left(\frac{-\kappa V_{TS}}{\phi_t}\right) \exp\left(\frac{\kappa V_{GS}}{\phi_t}\right)\left(1 - \exp\left(\frac{-V_{DS}}{\phi_t}\right)\right).$$

Aside from process dependent parameters, the leakage current can be decreased by sizing the transistor with a small W/L ratio, increasing the threshold voltage (via applying a bulk voltage – applicable only for PMOS), and decreasing the gate voltage with respect to the bulk/source.

For a given bias, there is only so much current that the transistor can provide. For typical CMOS imagers, such as with cameras, the photocurrent is larger than the leakage current, and therefore the current is drawn from the parasitic capacitance.

In our application we are measuring extremely low levels of light, and we cannot ignore the subthreshold leakage processes of the transistors. In the design depicted here, we use a PMOS device, and this gives us the possibility of biasing the transistor into accumulation. O'Halloran and Sarpeshkar (Sarpeshkar 2004) showed that when subthreshold conduction is eliminated (i.e. the transistor is biased well into accumulation), the source/bulk diode dominates the leakage. This can be mitigated by sufficiently reverse biasing the source-bulk junction. This is an option in future generations of this device.

The gate is biased at approximately $2V_t$ above the bulk and source, which are tied together. A dummy NMOS transistor of ½-size is placed to counter charge injection and clock feed-through. If the current drawn by the photodiode is less than the amount of current that can be supplied by the leakage, the transistor will function as a resistor. Since the source to bulk voltage is fixed at zero, the current can only change as a result of changing drain to bulk voltage. The signal change can be described as $\Delta V_{out} = R_{eq} \times \Delta I_{ph}$, where $R_{eq} = \frac{\partial V_{DS}}{\partial I_{DS}}$. If we exceed the maximum current that can be supplied by the leakage mechanisms at this bias, the current will drain off of the capacitor. The change in voltage is then given by $\Delta V_{out} = \frac{\Delta I_{ph} \Delta t}{C_{ph}}$.

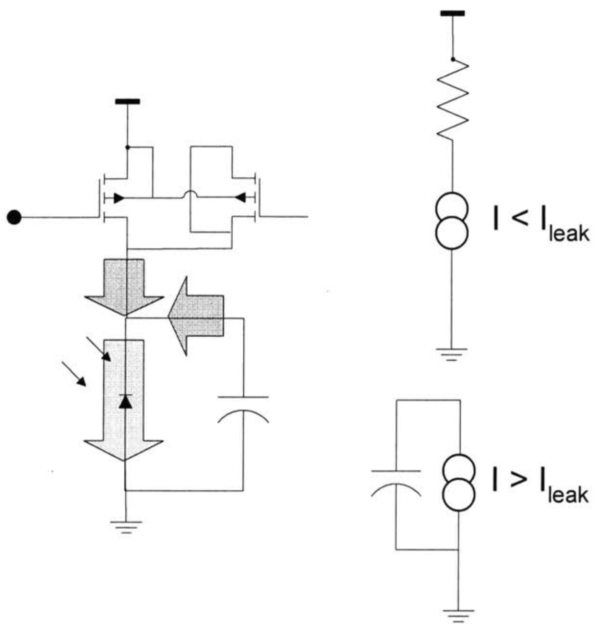

Figure 39: Imaging Modes: Capacitive versus Resistive.

The transition between these two modes of imaging can be seen experimentally when a pixel is given increasing amounts of light, increasing the photodiode current. **Figure 40** shows the digital output (red and blue) of single pixel with increasing voltage applied to an LED (green). The light seen by the photodiode is the light that is scattered from the evanescent illumination via the LED, and so is a low level of light. In this experiment, the transistor was not biased in to accumulation[4]. The red and blue traces represent the digital output from the amplifier, while the green trace represents the voltage applied to an LED, causing an increase in photocurrent. For the dark current and low light levels, the pixel operates in a resistive mode, caused by leakage current equaling the

---

[4] This can result from not completely powering up the chip. This creates only a small difference between the gate and bulk bias voltages on the reset transistor.

dark current and photocurrent. Increasing current causes a greater differential voltage as the dark current on the reference pixel remains constant, but the drain voltage on the light-receiving pixel must decrease to increase the leakage current. When the leakage current can longer match the photocurrent, the pixel enters the capacitive regime (sample 900). As the light intensity continues to increase the pixel resets very rapidly.

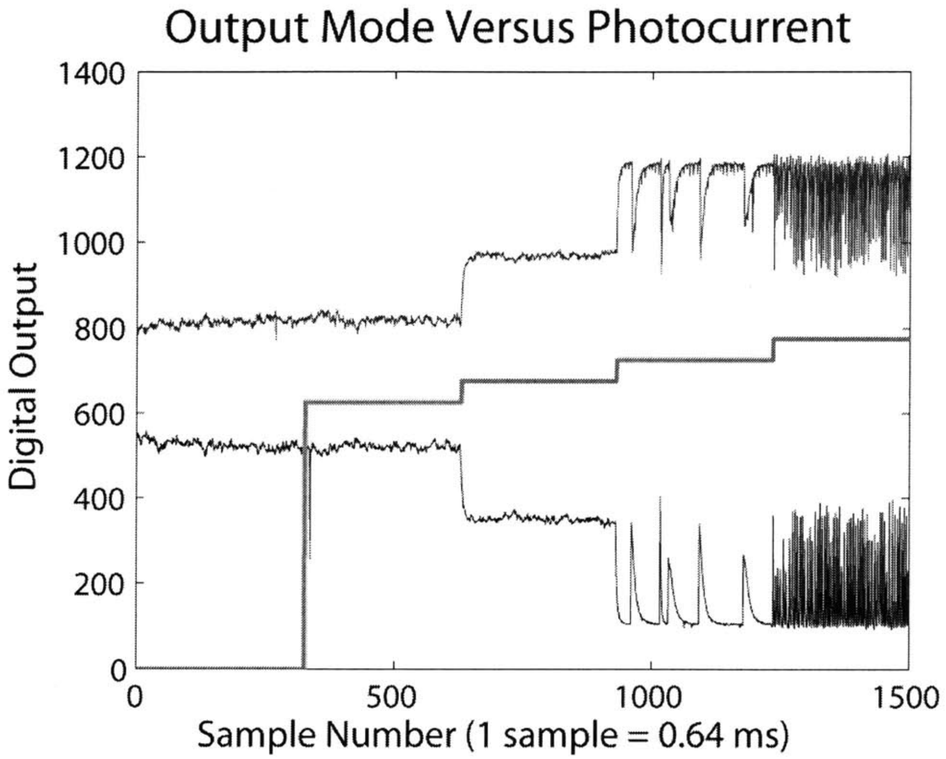

Figure 40: Output Mode versus Photocurrent

The red and blue traces represent the digital output from the amplifier, while the green trace represents the voltage applied to an LED, causing an increase in photocurrent. For the dark current and low light levels, the pixel operates in a resistive mode, caused by leakage current equaling the dark current and photocurrent. Increasing current causes a greater differential voltage as the dark current on the reference pixel remains constant, but the drain voltage on the light-receiving pixel must decrease to increase the leakage current. When the leakage current can longer match the photocurrent, the pixel enters the capacitive regime (sample 900). As the light intensity continues to increase the pixel resets very rapidly.

Data Analysis

Offset

As can be seen in **Figure 40** the pixel / amplifier output has an offset. This offset is in the same direction for every pixel, with varying magnitudes. (The amplifier was tested and the output referred offset is < 50 mV, indicating that the offset is from the pixel). The offset is likely due to the differences in parasitic capacitance on the photodiode, as the reference diode is covered with a metal shield. The circuit has been fabricated with a “FIB-able” offset (a parallel resistor can be removed, increasing the resistance of one leg of the amplifier) is included between the two amplifier stages (**Figure 27**). This will allow us to partially correct for the offset.

Operating Modes

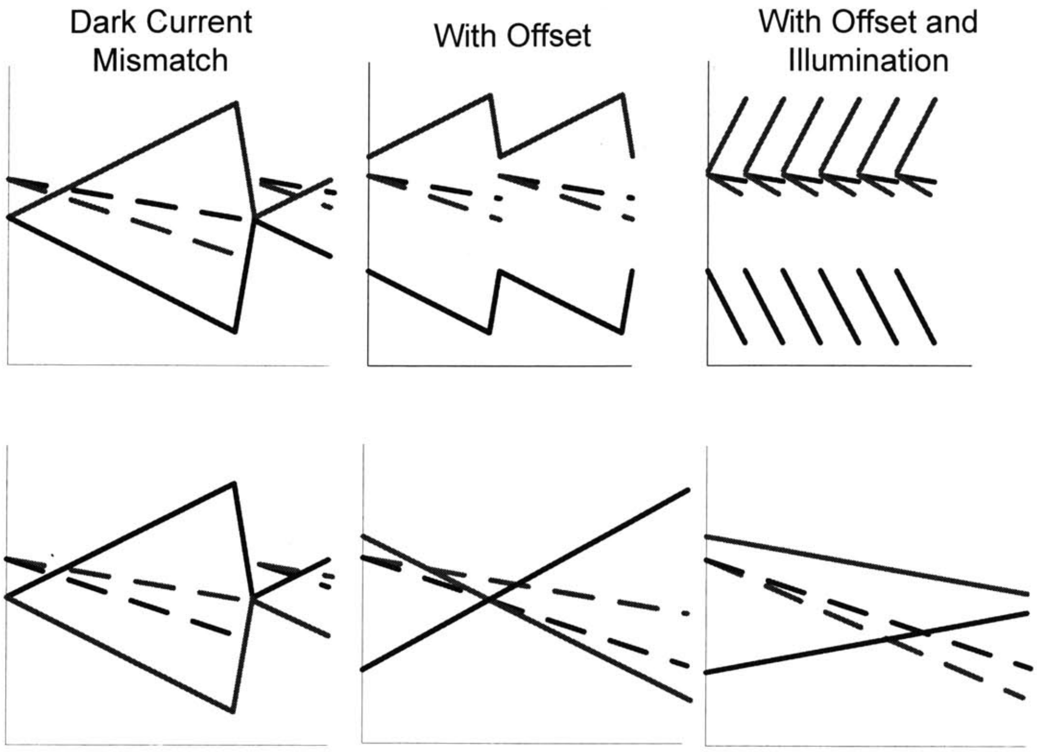

Figure 41: Integrating Schemes

The solid lines represent the amplifier output, and the dashed lines represent the pixel output. The differential outputs may sweep in either direction due to the fact that either photodiode (light sensing or reference) may have a greater dark current than the other. This is illustrated by the top and bottom sets of plots. When pixel offset is added, we can either get a much reduced range of operation, or an increased range of operation, depending on the mismatch of the dark current.

The amplifier will amplify the difference between the dark currents of the sensing and reference photodiode. Therefore, depending on which dark current is larger, the amplifier output with move in a different direction. If the red output increases, we see very little of the dynamic range of the amplifier due to the offset. On the other hand, if it goes the other way, we will see the full range. Currently, this is dependent on the random mismatch of the photodiodes, and cannot be controlled. A schematic illustration of this effect is shown in Figure 41. The solid lines represent the amplifier output, and the dashed lines represent the pixel output. The differential outputs may sweep in either direction due to the fact that either photodiode (light sensing or reference) may have a greater dark current than the other. This is illustrated by the top and bottom sets of plots. When pixel offset is added, we can either get a much reduced range of operation, or an increased range of operation, depending on the mismatch of the dark current.

The different cases are illustrated with the chip output shown in **Figure 42**. The dark current output from three different pixels is shown. The chip is powered by an 8 MHz sinusoidal wave from a function generator. The offset is consistently in the same direction, and likely due to the increased capacitance on the reference pixel as a result of the grounded metal light shield. The difference in dark current between sensing and reference photodiodes, varies in both sign and magnitude as expected. Furthermore, the variation in differential dark current from each pixel causes the amplifier output to sweep in different directions, at different rates. Each pixels output can either be referenced to its own differential dark current, or that of a single reference pixel. These traces illustrate the cases depicted in Figure 41. Furthermore, this illustrates that we can measure the dark current mismatch between the two pixels, which is estimated to be < 5% of 70 fA, or < 3 fA.

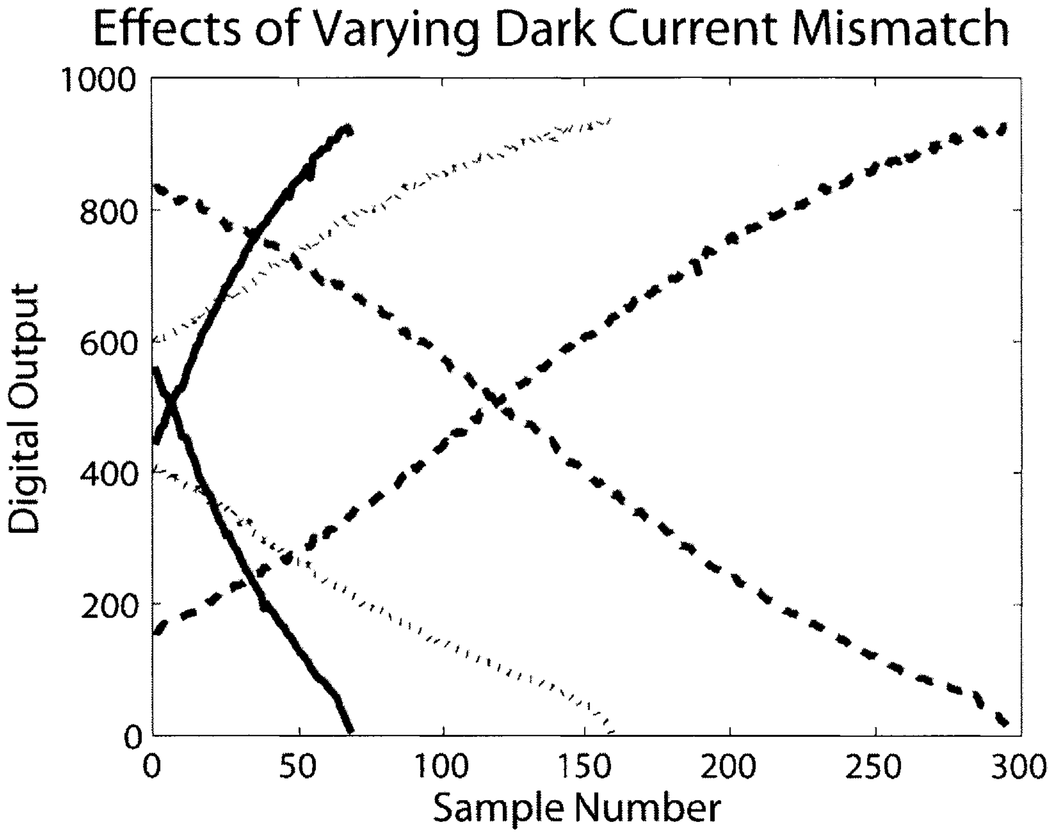

Figure 42: Effects of Dark Current Mismatch

Three different pixels are shown integrating dark current. The chip is powered by an 8 MHz sinusoidal wave from a function generator. Each chip has a slightly different offset, but all in a consistent direction. Furthermore, the variation in differential dark current from each pixel causes the amplifier output to sweep in different directions, at different rates. Each pixels output can either be referenced to its own differential dark current, or that of a single reference pixel. These traces illustrate the cases depicted in Figure 41.

Calibration Routine

Since the amplifier is in an open-loop configuration, the output is non-linear. To factor this out, we utilize a calibration scheme. The differential dark current acts as a constant current source producing a constantly increasing differential voltage. By selecting a pixel in which the differential signal sweeps the entire range of the amplifier and analog to digital converter, we can derive a calibration curve for the amplifier.

For our example, we will use the following data from a pixel in complete darkness. The trace represents the differential dark current. The trace of Pixel 1 for 126s is shown in **Figure 43**. The data is taken with $f_{clk} = 8MHz$, and each sample number corresponds to a time interval of 32 ms. The top trace (black) is the reset signal, which signifies when the pixel resets. The chip is initially subjected to a flash of bright light to reset all of the pixels (samples 30-90).

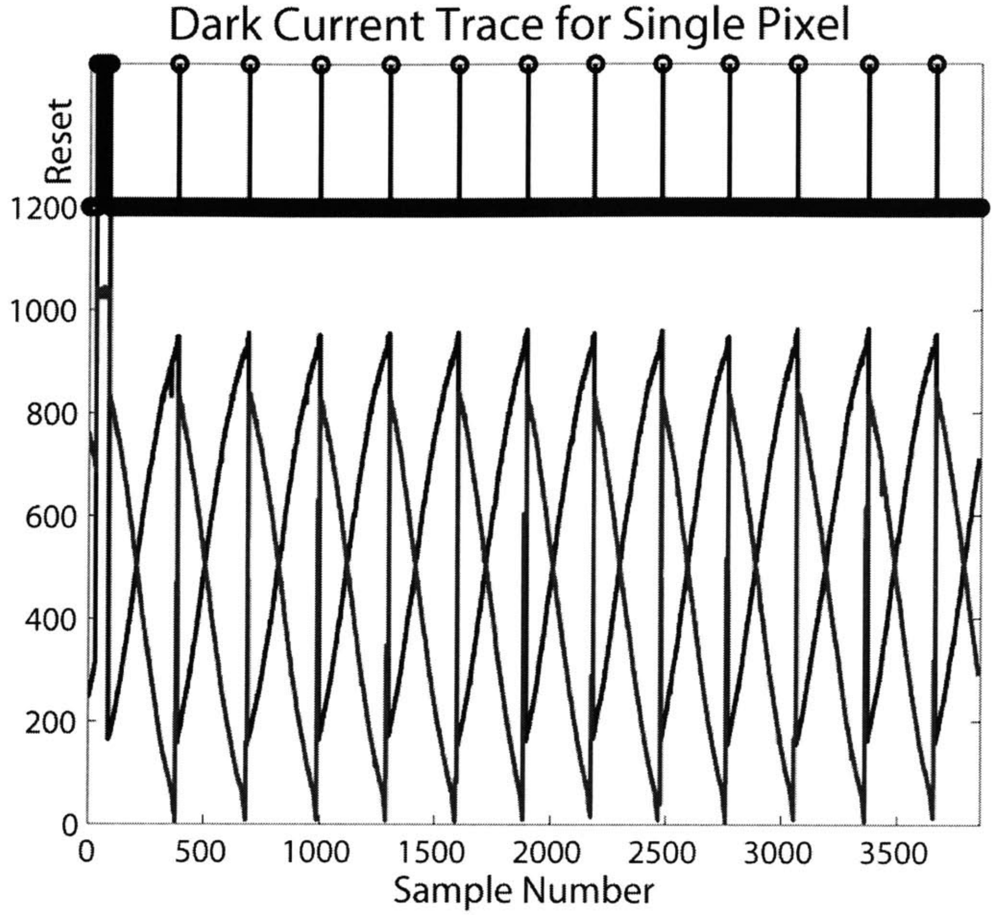

Figure 43: Calibration Routine: Dark Current Trace

The data is taken from the chip powered with a 5 V sine wave at 8 MHz. The output represents the integration of mismatched dark currents for a single pixel. Each sample number represents a 32 ms time interval.

The dark current adds a specific amount of charge per sampling period. By fitting a polynomial to the output trace, we can translate each digital output data point into the corresponding number of sampling periods (*n*), and consequently the amount of charge (*nQ*) that has been integrated on the parasitic capacitor (*C*).

$$\Delta V_{ph1,2} = \frac{nQ_{01,2}}{C_{ph1,2}}$$

The amplifier gain depends on the differential signal $\Delta V_{ph} = \Delta V_{ph1} - \Delta V_{ph2}$, and the output can be written as

$$V_{amp1} - V_{amp2} = A_V\left(\Delta V_{ph}\right) \times \Delta V_{ph}$$

where $A_V\left(v\right)$ is the amplifier gain as a function of input voltage. The differential digital output (*DO*) of the analog to digital converter can be characterized as

$$\Delta DO = f_1\left(\Delta V_{amp}\right) = f_2\left(\Delta V_{ph}\right)$$

where

$$\Delta V_{ph} \propto n$$

The data consists of a set of points $\left(n, \Delta DO_n\right)$, and we can construct a function $\Delta DO = f_3\left(n\right)$. We use a polynomial fit, with the order determined by the finding the order with the minimum least squares error. To prevent over fitting, the error is inversely weighted by the number of y values that correspond to multiple x values. The result is shown in **Figure 44**.

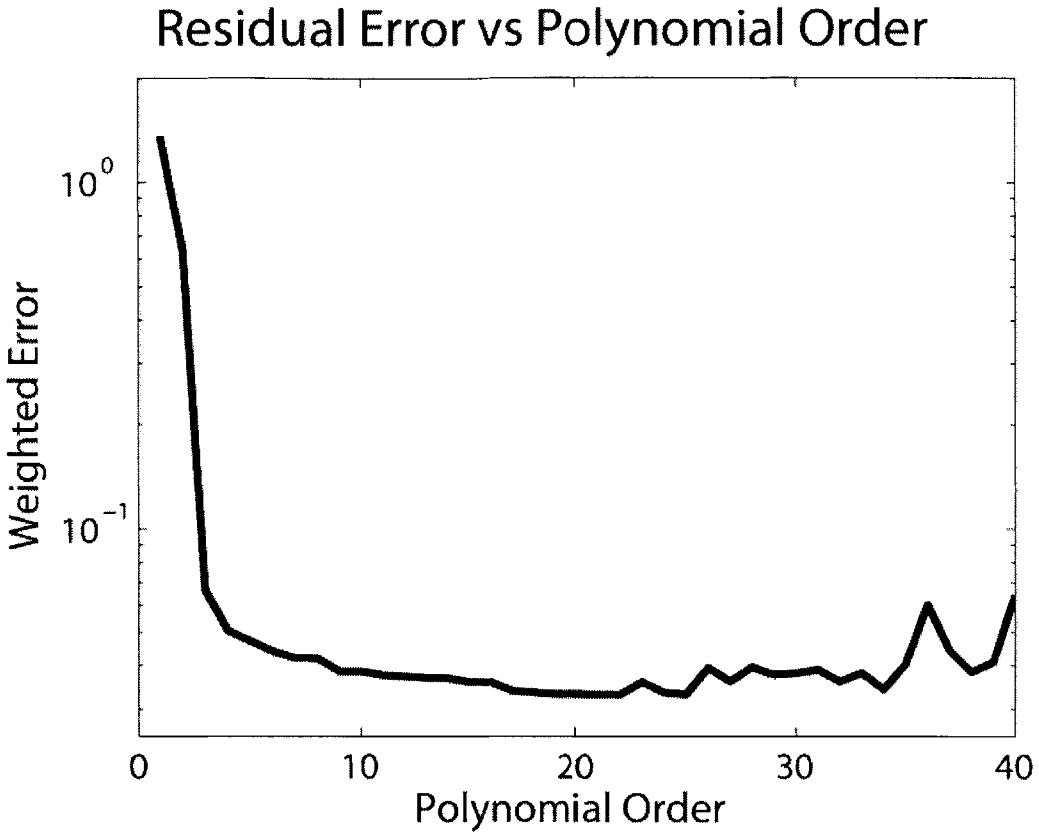

Figure 44: Least Squared Error from Polynomial Fit versus Fit Order

The differential output is fit to a polynomial of increasing order, and the least squares error is determined. The error is weighted by the number of y values that have multiple x values, to prevent over fitting. The order with the least error is used for the fit.

The minimum error for the fit is n=25. The fit with the residuals is shown in **Figure 45**. Once the function is established, any digital output (ΔDO_n) can be solved for the *n* of the reference pixel. Data from other pixel traces $(k, \Delta DO_k)$ can be mapped to the reference curve by solving what value of n on the reference curve gives a value of ΔDO_n equal to ΔDO_k.

$n_k = f_3^{-1}\left(\Delta DO_k\right)$

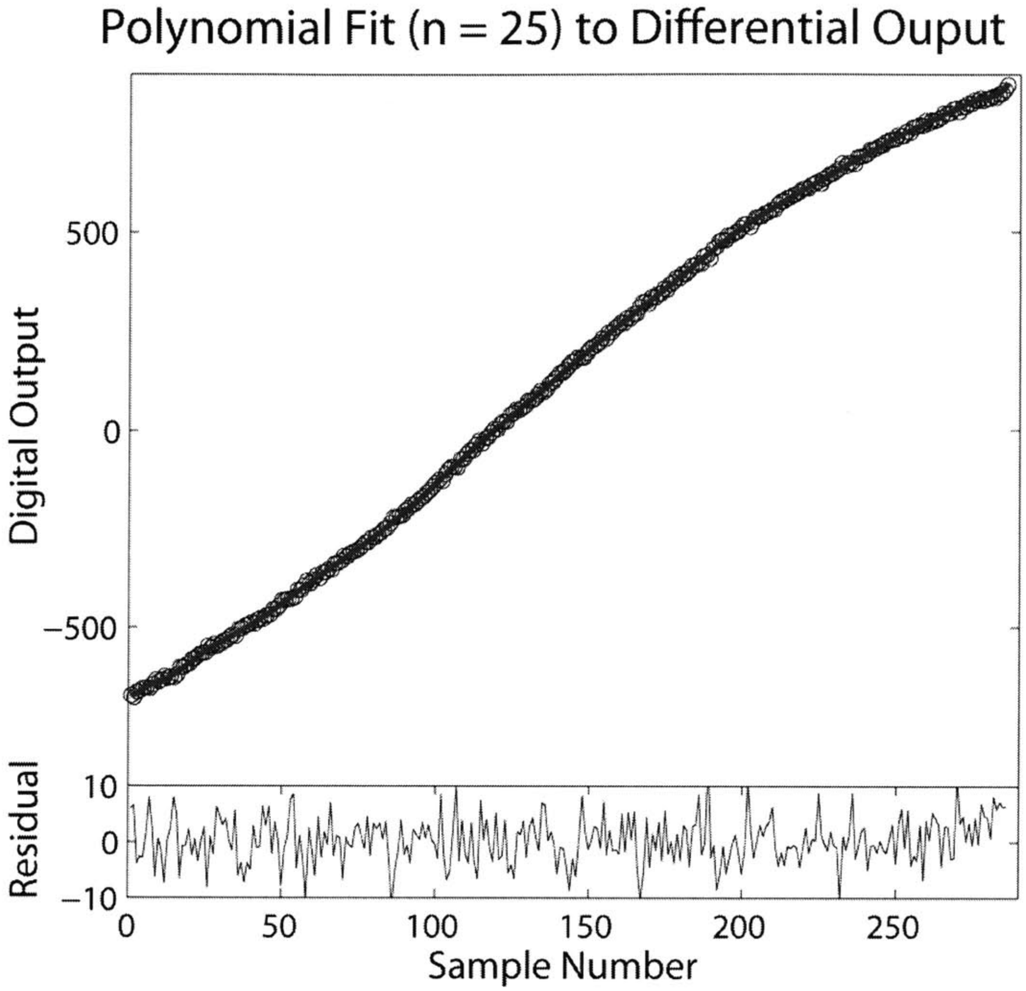

Figure 45: Polynomial Fit to Differential Output and Residuals

A 25th order polynomial is fit to the differential output from the dark current. The residuals are plotted in the lower graph.

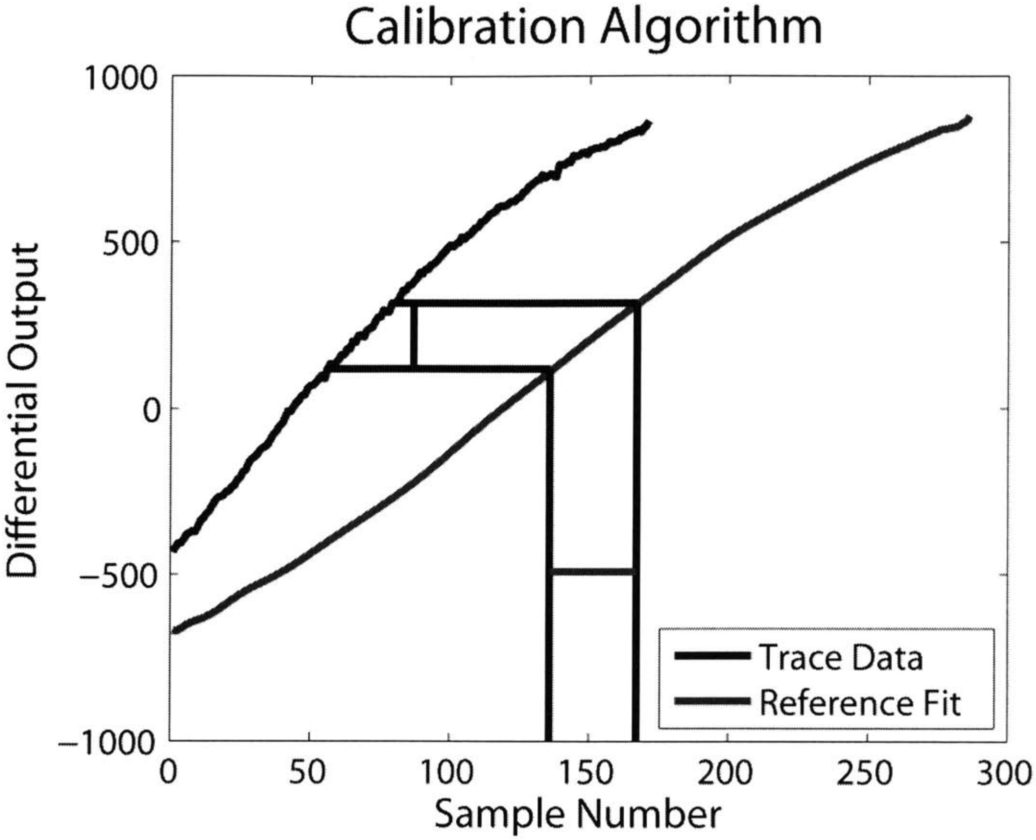

Figure 46: Fitting Trace Data to Reference Fit

The reference trace of the dark current is shown in red, and the trace from a different pixel (dark current) is shown in blue. For each y value on the blue trace, the corresponding x value for the reference trace is found.

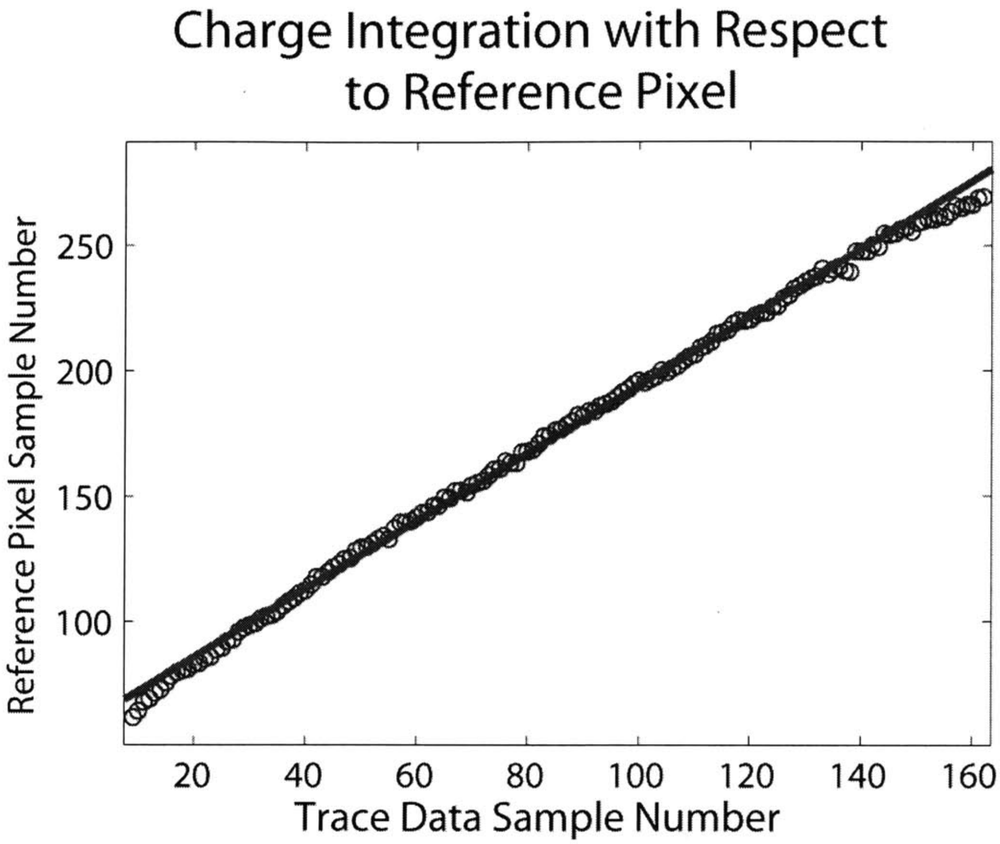

Figure 47: Plot of Sample Trace versus Reference Trace

For each point (x_s, y_s) of the sample curve, the corresponding x value of the reference (blue) trace (x_R) for $y_s = y_R$ is found. The values of the sample versus reference trace (i.e. (x_R, x_s)) are plotted, and the slope is determined.

Using the trace of Pixel 1 as the reference curve, the differential dark current of each pixel can be found (relative to Pixel 1). This is illustrated in **Figure 46**, where the trace from the reference pixel is plotted in red, and the trace from another pixel is plotted in blue. For each point (x_s, y_s) of the sample curve, the corresponding x value of the reference (blue) trace (x_R) for $y_s = y_R$ is found. The values of the sample versus reference trace (i.e. (x_R, x_s)) are plotted, and the slope is determined (**Figure 47**). The slope is 1.356 with a 95% confidence interval of (1.347, 1.346). This means that the differential dark current for Pixel 4 (Sample Trace) is 35% more than the differential dark current of Pixel 1. This process can be repeated for every pixel on the chip, and results (relative to Pixel [1,1]) are shown in **Figure 48**. {Pixel [3,3] is an on chip reference with only the dark current.[5] Consequently it is always saturated, and therefore marked with a value of zero.}

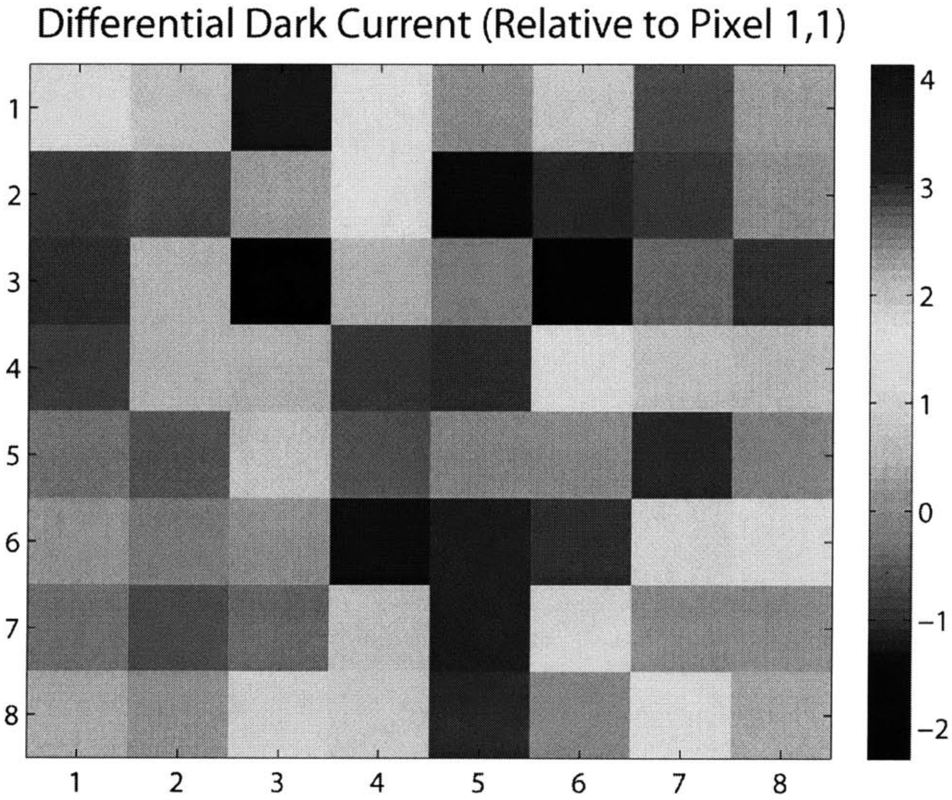

---

[5] This serves as a frame reference to establish the location of each pixel on the chip.

Figure 48: Differential Dark Current

The differential dark current is plotted for each pixel, referenced to pixel [1,1].

By acquiring data over a long period of time, we can use the first traces as a reference and gather statistics on the noise of the system. **Figure 49** shows the repeated values of Pixel 1 differential dark current with respect of the first trace.

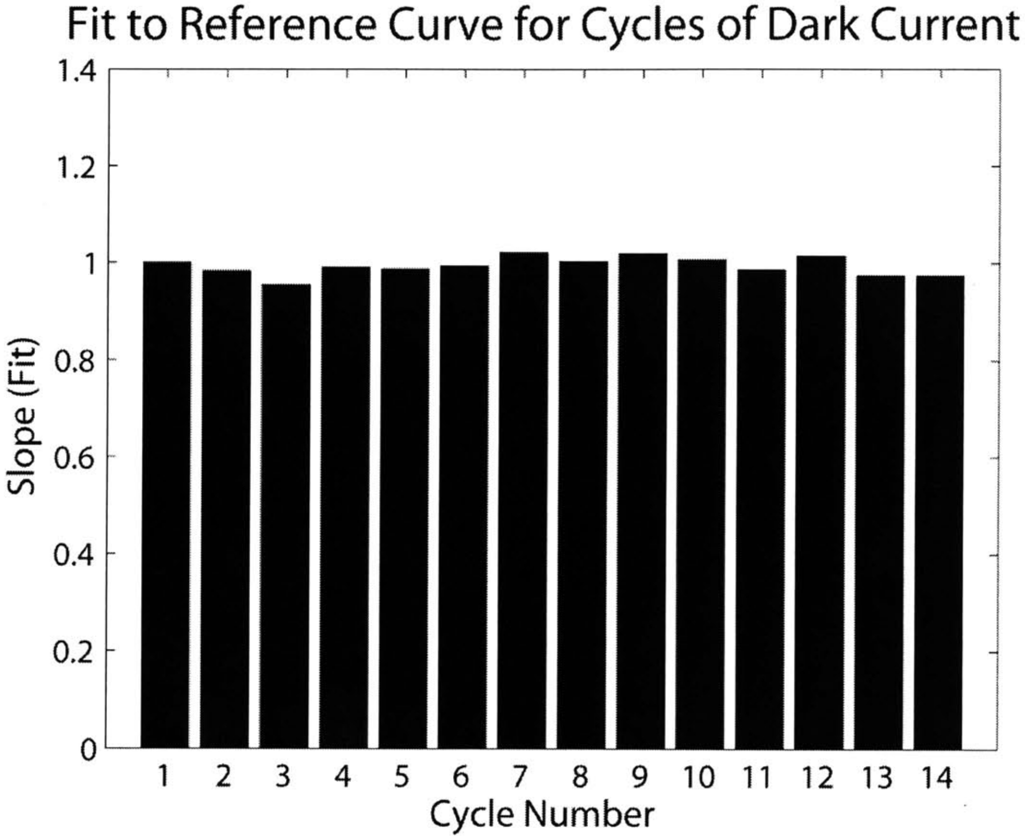

Figure 49: Determining Pixel Error

The dark current trace outputs are fitted to a single trace. The values of the fits are plotted versus cycle (i.e. between each reset) number. By taking the standard deviation we can determine the error.

We can repeat this for the entire chip and plot the standard deviation for each pixel. Since each pixel has a different saturation time, depending on the level of the differential dark current, a valid metric of the noise is the standard deviation of the mean in a set amount of time. In **Figure 48**, each pixel's dark current was repeatedly integrated over a period of two minutes, and compared to the initial dark current trace. The slopes were computed as shown above, and the log of the standard deviation of the mean is shown in Figure 50. Since the mean slope is 1 for each pixel (each pixels trace is referenced to its own dark current calibration trace), the standard deviation of the mean represents a percent error (for a 2 minute total integration). The vast majority of the pixels have an error of less than 1%.

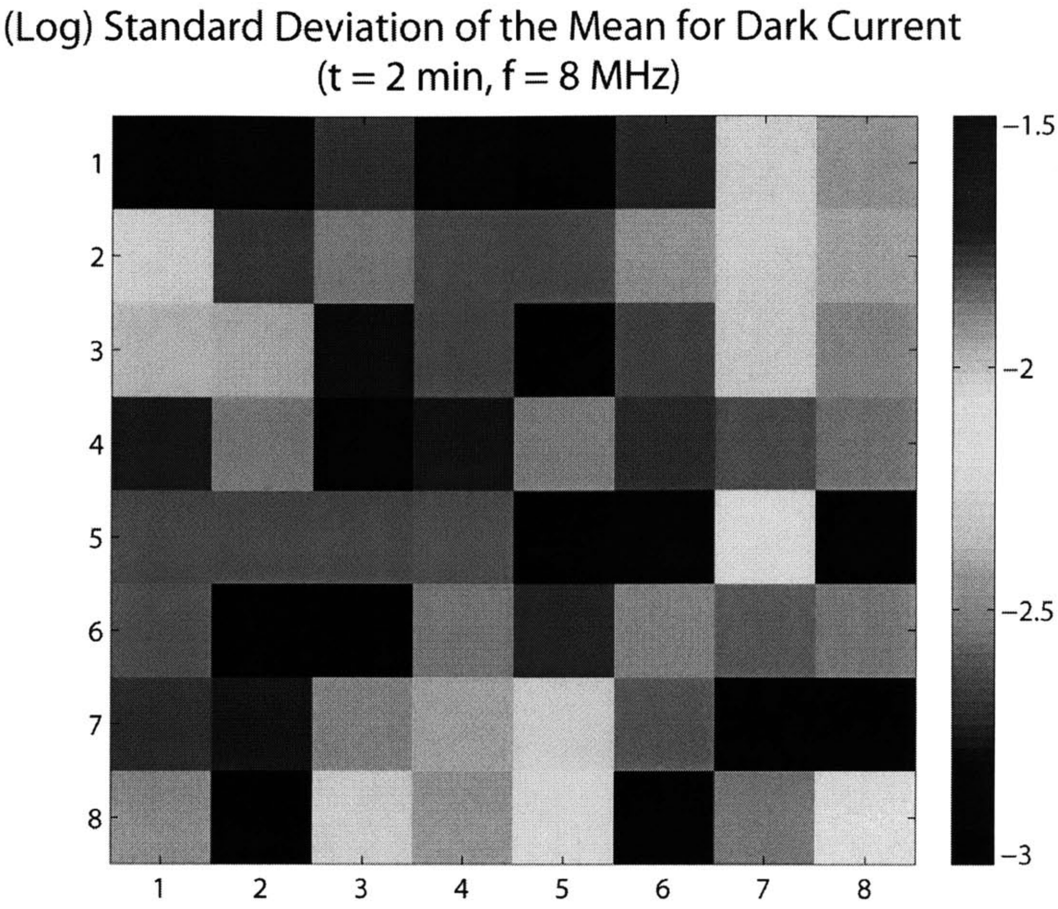

Figure 50: Log Standard Deviation of the Mean for Dark Current for 2 minutes of sampling.

To quantify measurement of light, we use the mismatch dark current as a reference. For the example trace shown (Figure 51), the calibration data is used in the routine, and correspondence a ratio of 0.994 was found. The light was increased and the calibration curve was ratio was 0.9832. The fits are plotted in **Figure 52**. The red trace represents the fit of the dark current to the reference pixel. The blue trace represents the fit of N = 0:100, and the brown trace represents the fit of N = 100:200. The results of the fit are shown in Table 8. Furthermore, the light was changed during the data acquisition and this can be seen as a change in the slope of *n* vs. *m*. At N = 100, the intensity of light was further increased, and measured at 0.84.

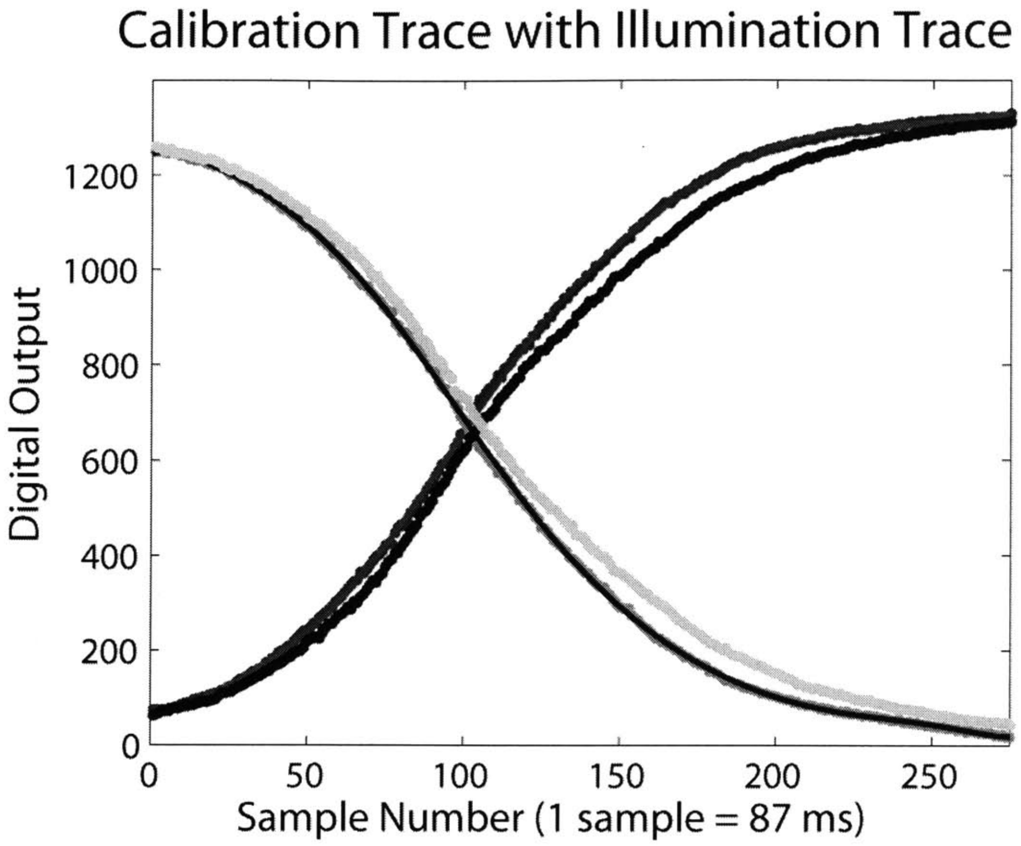

Figure 51: Calibration Trace versus Trace with Illumination

This figure illustrates the effect of illumination on the differential output. The calibration curves (i.e. dark current) are shown in blue and red (one for each output). The aqua and black traces represent the trace during illumination. Illumination increases at ~ Sample Number = 100.

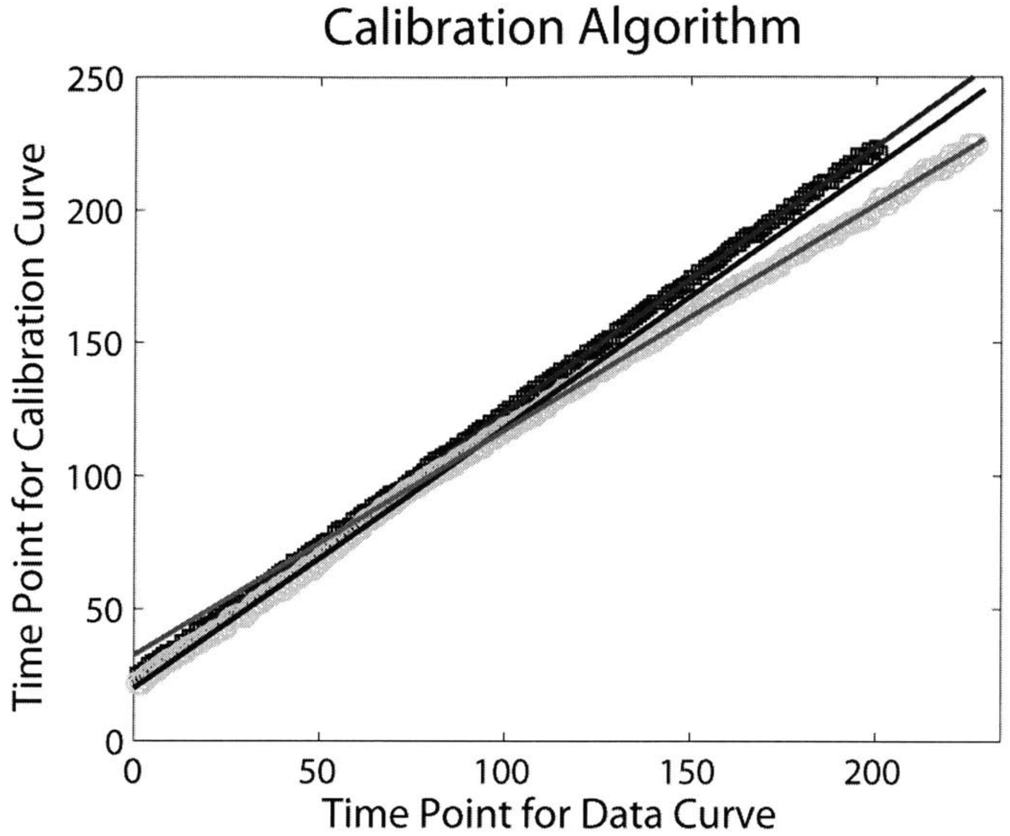

Figure 52: Fits from Calibration Algorithm

The red trace represents the fit of the dark current to the reference pixel. The blue trace represents the fit of N = 0:100, and the brown trace represents the fit of N = 100:200. The results of the fit are shown in Table 8.

Table 8: Fits for Illuminated Traces

	Slope	95% Min	95% Max
Calibration	0.9979	0.994	1.001
Light (Seg 1)	0.9832	0.9706	0.9958
Light (Seg 2)	0.8474	0.8439	0.8509

Detection Levels

The parasitic capacitance of the photodiode is approximately 2 pF, and the dark current is approximately 70 *fA* (from NSC design rules) for a 120 μm x 120 μm pixel. The amplifier is designed to saturate with approximately 10 mV of differential input. By using Pixel 1 as the reference, the amplifier saturated in 286 cycles, which at 8 MHz, corresponds to 9.4 s. Therefore, the differential current is approximately 2 *fA*. The approximation of 2 *fA* is also corroborated by the fact that the differential dark current should be less than 5% of the dark current (i.e. less than 3.5 *fA*)

For a 2 minute integration, the standard deviation of the mean (for most pixels) lies between 1% and 0.1%. Taking the quantum yield to be 0.5, and the detection limit to be 1% of the dark current, the minimum detectable signal (in 2 minutes) is approximately 250 photons / sec. This corresponds to 0.017 photons μm^{-2} s^{-1}.

Conclusion

We have demonstrated the design, fabrication and testing of a CMOS photosensor that operates on a single sinusoidal power supply. Although standard CMOS processes have dark currents that are typically too high (~ 10 $aA/\mu m^2$) for low light detection, the use of a differential pixel topology has allowed us to have an effective dark current on the order of 0.1 $aA/ \mu m^2$. We have demonstrated detection of approximately 0.017 photons μm^{-2} s^{-1} for a 120 µm x 120 µm photodiode. This sensitivity will allow the sensor to be used for µarray applications.

References

Eltoukhy, H. S., K.; Gamal, A.E. (2006). "A 0.18-/spl mu/m CMOS bioluminescence detection lab-on-chip." IEEE Journal of Solid-State Circuits **41**(3): 651-662.

Sarpeshkar, M. O. H. a. R. (2004). "A 10-nW 12-bit Accurate Analog Storage Cell with 10-aA Leakage." Journal of Solid State Circuits **39**(11).

Chapter 5: An Optics-Free CMOS μArray Reader

Abstract

We demonstrate the application of a sensitive, low-light CMOS imager as a μarray reader. With the advent of μarray technology, and its increasing applications in the areas of research and diagnostics, it has become necessary to develop a low cost imager compatible with existing μarray platforms. A simple low cost imager will enable the μarray technology to be used more widely. We implement a CMOS imager in standard 0.18 μm digital process, and apply several strategies to eliminate the need for optics. As a proof of concept, we demonstrate the detection of fluorescently labeled streptavidin without the use of optics (filters and lenses). We detected a 20 nM concentration of streptavidin with a signal to noise ratio of approximately 100. Furthermore, the chip is powered with a single sinusoidal power supply, enabling it to be powered with an appropriate wireless interface.

Background

μArrays represent a high throughput method of analyzing complex biological samples. Applications range from DNA to proteins and small molecules. Currently μarray readers primarily consist of photomultiplier tubes or high intensity CCD cameras due to the sensitivity requirements for detection of low light signals. In typical applications, DNA, proteins or small molecules that bind to specific (known) targets are spotted on a chemically functionalized glass substrate. The sample to be assayed is labeled with a fluorophore and then hybridized to the array. Fluorescence is measured at each spot by excitation with a laser. The fluorophore shifts the excitation light to a longer wavelength, which is gathered by a lens and focused on the imager. The excitation light is filtered out, to reduce the background.

The use of CMOS detectors for DNA detection has been previously reported using a variety of methods. Xu et al (Chen Xu 2005) reported a method using conjugation to opaque metallic nanoparticles (in lieu of a fluorophore) to block light from a photodiode, resulting in DNA detection. This method requires patterning DNA directly onto the CMOS sensor. Eltouky et al (Eltoukhy 2006) reported a CMOS-based imager for DNA detection. The design made use of a specialized CMOS process designed for low dark current applications, and was capable of detecting 0.004 photons/μm^2/s. Other approaches include conjugation of DNA to an enzyme, which results in an oxidation/reduction reaction, generating local charge (Hofmann 2002; Thewes 2002; Claudio Stagni 2007). Barbaro et al (Barbaro 2006) used the intrinsic properties of DNA (negative charge) to make a charge sensitive DNA detector. Additional methods utilize magnetic particles (D. Baselt 1998; P-A. Besse 2002; Turgut Aytur 2006) as labels for DNA and/or protein. These strategies allow for detection of DNA and protein by directly patterning the array on the CMOS substrate. Although optimal for small arrays and single-ligand assays, the size of the array that can be patterned on a CMOS substrate can be limited due to the size of the chip and the need to dispose of the chip after use. Additionally, to further expand the utility of CMOS sensors to µarrays, compatibility with existing protocols (i.e. patterning of arrays on glass slides) must be incorporated.

To address this, CMOS imagers have been incorporated into traditional optical setups (Figure 57) . This approach still requires precise optics (filters, lenses), which increase the size, cost and complexity of the µarray readers. Here we present the design, fabrication and testing of a CMOS image sensor fabricated in a standard digital process capable of interfacing with standard microarrays without the use of optics. The design eliminates the use of optics (filters and lenses) by using ultraviolet, evanescent wave illumination, in conjugation with quantum dots to provide a long Stoke's shift. By placing the sensor close to the array, we can establish an effective numerical aperture, realizing a low-cost method of interfacing with existing µarray technology. The sensor is capable of detecting ~ 0.02 photons/μm^2/s using a single sinusoidal power supply. The implementation of a sinusoidal power supply enables the possibility of a wireless power interface.

Experimental

(The design details are detailed in the previous chapter, and will not be repeated here.) Standard µarrays operate by patterning biological molecules (DNA, proteins, small molecules, etc) on an array. The sample is labeled with a fluorescent marker and is hybridized to the array. To establish the proof of concept for an optics-free µarray reader, we will pattern biotinylated-bovine serum albumin (BSA) and standard (non-biotinylated) BSA and detect the presence of labeled-streptavidin. We incorporate several strategies to eliminate the need for optics. In standard µarray readers (Figure 53), an excitation beam (typically a laser) illuminates the array, and is absorbed by the fluorescent label. The fluorescent label re-emits light at a slightly (typically 10-30 nm) longer wavelength, which is then focused and filtered before being imaged by a CCD or PMT.

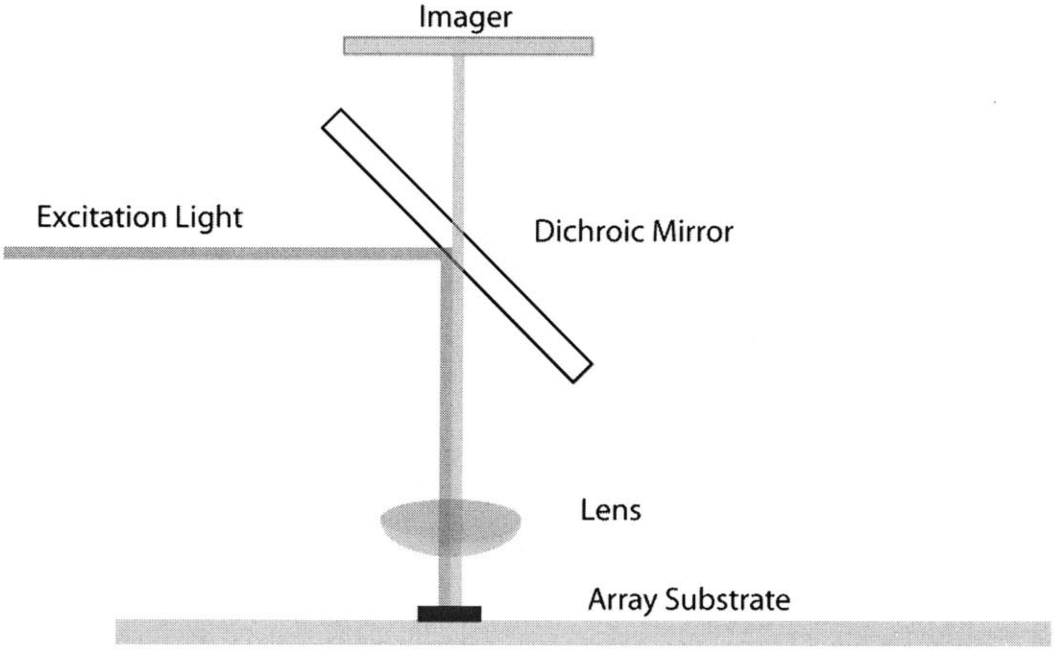

Figure 53: Standard µarray reader.

µArray readers operate by illuminating the sample with an excitation beam, and the fluorescent label on the hybridized sample re-emits light at a longer wavelength (lower energy). This light is focused and filtered, before being detected by either an intensified (and cooled) CCD, or a photomultiplier tube (PMT).

In order to eliminate the need for optics we must eliminate both the lens and filters. The filters are eliminated by taking advantage of the inherent wavelength sensitivities of silicon. As shown in Figure 54, silicon absorbs short wavelengths (i.e. ultraviolet) extremely close to the surface. Furthermore, the photodiode is most responsive when light is absorbed in the depletion region. For the Nwell/Psub photodiode, this is about 1 μm below the surface, and very little ultraviolet light penetrates this far. Therefore, if ultraviolet light is used as the excitation light, the inherent absorption properties of the silicon will act as a filter. (This strategy will not completely filter out the excitation light because of the long diffusion length of the generated carriers.[6])

The next challenge is to find a fluorophore with a large enough Stoke's shift to be illuminated with ultraviolet light, and emit light in the visible or near-infrared spectrum. Additionally, most organic fluorophore bleach when exposed to ultraviolet light. To avoid these shortcomings of traditional fluorophore we use quantum dots. Quantum dots emit light at a wavelength defined by their physical

---

[6] A more effective strategy (for future consideration) would be to have an shallow junction diode that gathered all of the carriers form the UV excitation light, and the deeper junction diode would only detect the longer wavelength emitted light.

dimensions. Furthermore, they absorb at any energy higher than their emission energy. The absorption and emission curves are shown in Figure 55.

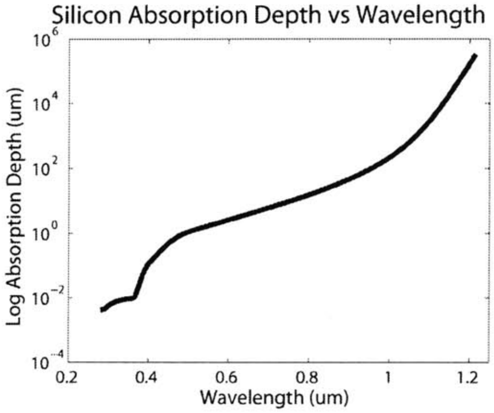

Figure 54: Silicon Absorption Coefficient as a Function of Wavelength.

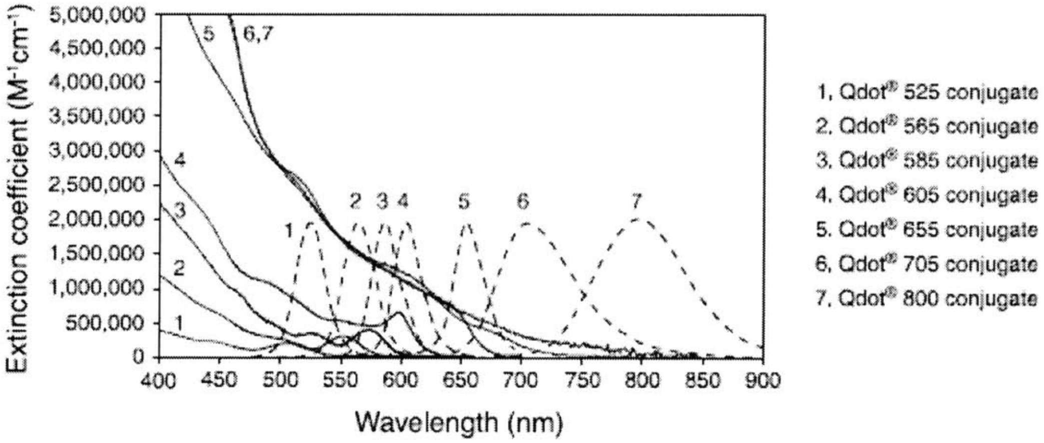

Figure 55: Quantum Dot Absorption and Emission Spectra[7].

---

[7] www.invitrogen.com

To conduct the assay we functionalize a quartz cover slip[8] (Electron Microscopy Sciences) with aminopropyltriethoxysilane (ATPS, Sigma) by boiling cover slips in ultra-pure water for 10 minutes and sonicating for 10 minutes. The glass surface was activated by incubation in 1 M NaOH for 10 minutes. The coverslips were functionalized in 95% ethanol, 2% glacial acetic acid (pH 5), and 2% APTS for 5 minutes. The coverslips were rinsed in ethanol and water before being spun dry.

Biotinylated BSA (Sigma) was diluted to 1 mg/ml in phosphate buffer saline (PSB) and spotted on the coverslip. After drying, the coverslip was submerged in a solution of 5% w/v BSA (Sigma) in PBS for 3 hours at room temperature. The coverslip was washed three times in PBS and spun dry. 50 µl of a 20 nM solution of 594 quantum dots (Invitrogen) (in 1 mg/ml of BSA) was spotted on a slide and the coverslip was inverted and placed over the solution. The coverslip was incubated at room temperature for 1 hour in a humid chamber. The coverslip was then washed three times in PBS and spun dry. The single spot "array" is visualized on the GenePix Axon 4000B scanner, and shown in Figure 56.

---

[8] Quartz coverslips are used to allow UV light to be efficiently transmitted through the glass.

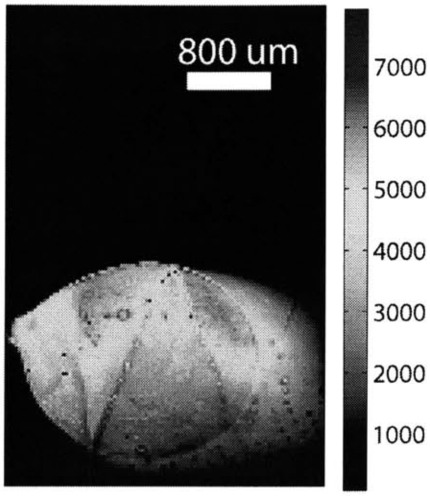

Figure 56: Biotin BSA and Control on Quartz Cover Slip
Biotin BSA and BSA are spotted on the functionalized quartz coverslip, and incubated with 565 Streptavidin Qdots. The coverslip is scanned in the Genepix Axon 4000B µarray scanner.

The coverslip is placed on a prism made from fused silica. The prism is a custom dove prism with 70 degree sidewalls (Redoptronics). The prism is first cleaned with methanol, ethanol, and water. Glycerol is used as the immersion oil. A 280 nm ultraviolet LED (Sensor Electronics) is focused to totally internally reflect off of the prism. This results in evanescent wave illumination of the array, further reducing background. The chip and package is placed approximately 3 mm above the coverslip surface. The optical diagram is shown in Figure 57.

The chip is powered by an 8.7 V_{pp} sine wave (DC = 0) at 3 MHz via a function generator (Agilent). Since the on-chip amplifier is implemented in an open-loop configuration, a calibration scheme is required to correct for the non-linear output. The "dark" output results from a constant, mismatched, differential photodiode current, and generates a constant change in input voltage (to the amplifier) per unit time. Since the input to the amplifier is linear with time, we can calibrate the amplifier output. Pixel 2 is selected as the reference pixel, and the differential output is fit to a polynomial (Figure 58). All subsequent outputs are referenced to this curve.

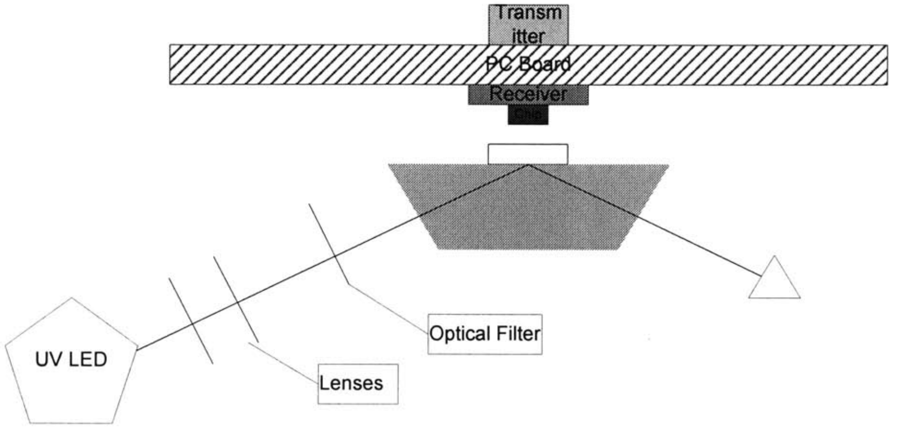

Figure 57: Optical Setup

The LED is focused to make a collimated beam, and filtered such that only 280 nm light is emitted. The optical chip is placed as close to the surface as possible.

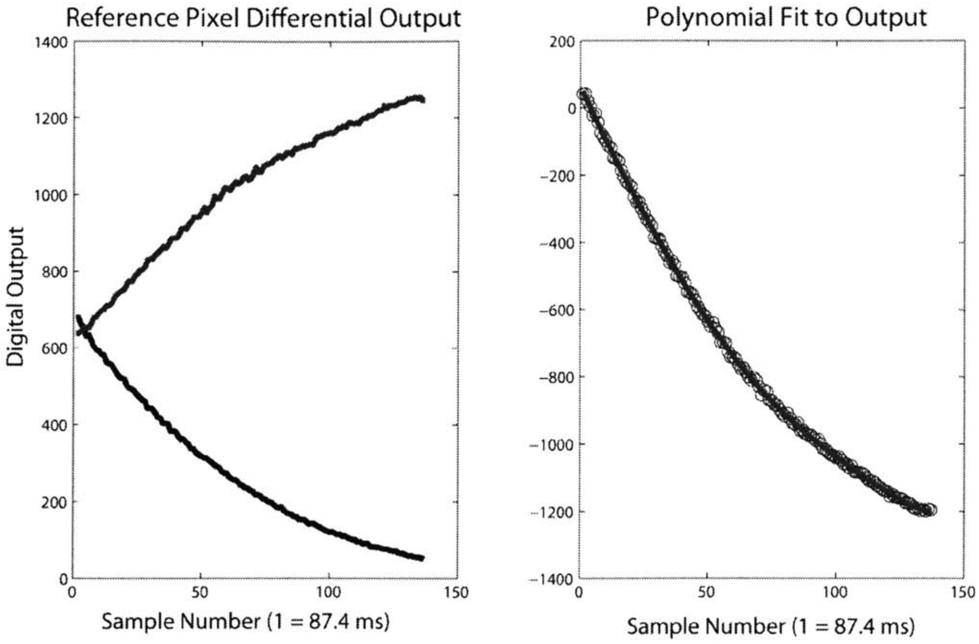

Figure 58: Reference Pixel Output

The reference pixel dark current, with polynomial fit (n = 20). Please see the previous chapter for details on the calibration routine.

The LED is activated and the area where the biotinylated BSA is spotted is imaged. The coverslip is then moved by a motorized stage (Thor Labs), and an area of BSA is imaged. The raw data and representative traces for the different regions (dark current, BSA, and Biotin BSA) are shown in Figure 59. The data is analyzed for each pixel by dividing the continuous data trace into individual traces (separated by resets), and fitting them to the reference trace (as outlined in the previous chapter). The results are shown in Figure 60. The dark current values exhibit a wide variation due to the random nature of the mismatch in the photodiode dark currents. The values increase when the BSA is evanescently illuminated by the ultraviolet LED. This is largely due to the scattering of the LED light at the prism and slide surface. This background signal could be eliminated by filtering, but we aim here to demonstrate the sensing platform without the use of optics on the detector. As an alternative, a polymer or spin-on glass with strong ultraviolet absorption could be easily added to the sensor surface. One pixel serves as a frame reference and has only a single photodiode, and the output is therefore the dark current (as opposed to the differential dark current). This consistently saturates the detector, and is easily identifiable. This pixel is Pixel 61 in Figure 60. Pixel 28 (Figure 60) operates in the resistive mode, likely due to higher leakage of the reset transistors, and is therefore excluded from the analysis.

Since each pixel (and each regime, dark current, BSA, Biotin BSA) has a different integration time, we define the error by the standard deviation of the mean within a certain acquisition time. The data for each regime is taken over approximately 3 minutes. The net signal and standard deviation for both the BSA and Biotin BSA signal are shown in Figure 61. The net signal is the Biotin BSA signal with the background BSA signal subtracted. The standard deviation of the mean is also given for both the positive signal and the background (negative control). For the most intense pixels, the signal to noise (defined by the net signal to standard deviation) is ~ 100. The variation in pixel intensity is due to the non-uniformity of illumination as well as of the distribution of Biotin BSA on the coverslip.

Using the framing pixel, we can recreate a spatial image of the data, where each pixel's data corresponds to its physical location on chip. The results are shown in Figure 62. The pixel data for background, BSA and Biotin BSA is mapped to the correct spatial location using the framing pixel. The dark current intensity is random, as is expected from nature of the photodiode mismatch. The BSA (negative) control intensity is several times the differential dark current intensity. Additionally, a region of higher intensity is seen at the lower part of the array, likely due to variations in illumination intensity from the LED. The Biotin BSA spot clearly has an increased intensity over the background BSA. The net signal is the biotin BSA with the BSA background subtracted, divided by the illumination intensity. The illumination intensity is defined as the BSA background minus the dark current. An area brighter than the surrounding area can be seen on the right side of the array. This is likely due to the non-uniformity (see Figure 56) of the spot and the difficulty in aligning the sensor with the center of the microarray spot.

Conclusion

There is a need for low cost readers compatible with existing µarrays. CMOS-based sensors offer an excellent approach because they can designed as an “intelligent substrate”, with the ability to integrate sensors with signal processing electronics. The majority of CMOS implementations involve directly patterning the array on the sensing device. While this is an optimal solution for small µarrays, larger µarrays require a disposable substrate, and traditional protocols are optimized for functionalized glass substrates.

The work presented here demonstrates the utility of an optics-free μarray reader. Filters are eliminated by the use of ultraviolet illumination, quantum dots for a large Stoke's shift, and the inherent absorption properties of silicon to filter the illumination light. Furthermore, an evanescent wave illumination scheme is used to reduce background. Lenses can be obviated by placing the sensor as close to the surface as possible.

The sensor is designed in a standard digital process, and can detect down to 0.02 photons/μm^2/s while powered by a single sinusoidal wave. This makes it compatible with a wireless power interface. To the best of the author's knowledge, this is the first array-based optical sensor capable of functioning with a single sinusoidal power input. Future efforts will be directed towards integrating a suitable receiver for wireless power transfer.

The majority of μarrays are based on the principle of spotting a biological ligand, complementary to what is to be detected, on a functionalized surface. The sample is then labeled, and hybridized to the array. We generalize this principle by patterning an array of biotinylated protein, and detecting labeled streptavidin. We successfully detected a 20 nM Streptavidin solution with a (maximum) signal to noise ratio of 100.

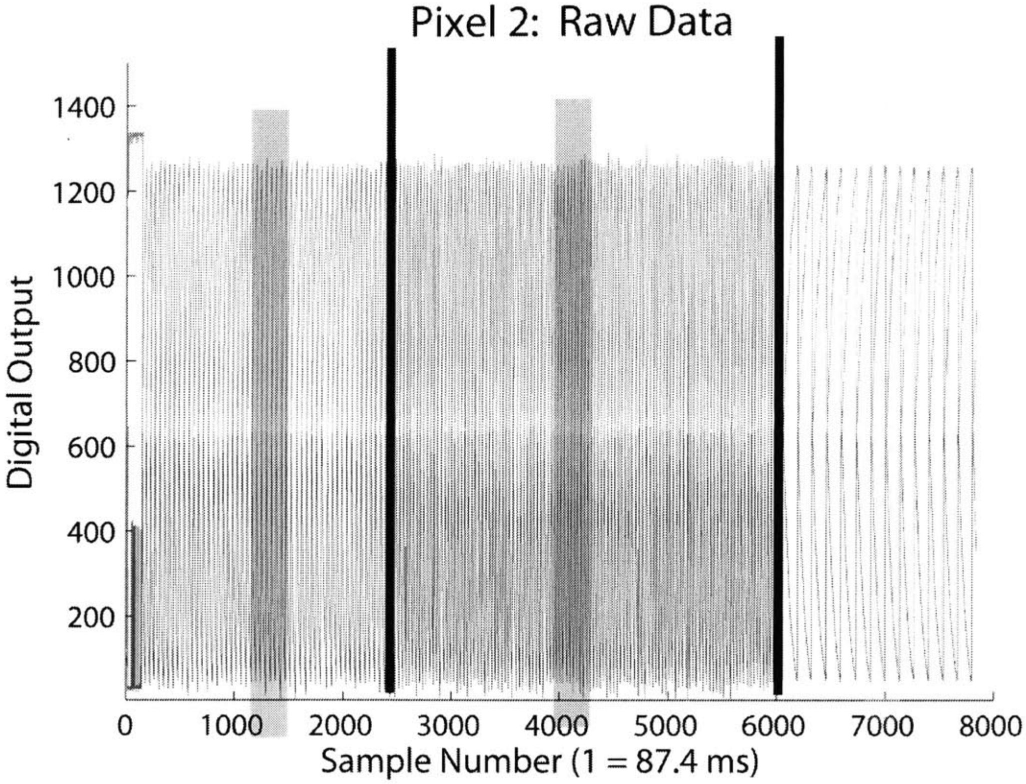
Pixel 2: Raw Data
Digital Output
1400
1200
1000
800
600
400
200
0
1000
2000
3000
4000
5000
6000
7000
8000
Sample Number (1 = 87.4 ms)

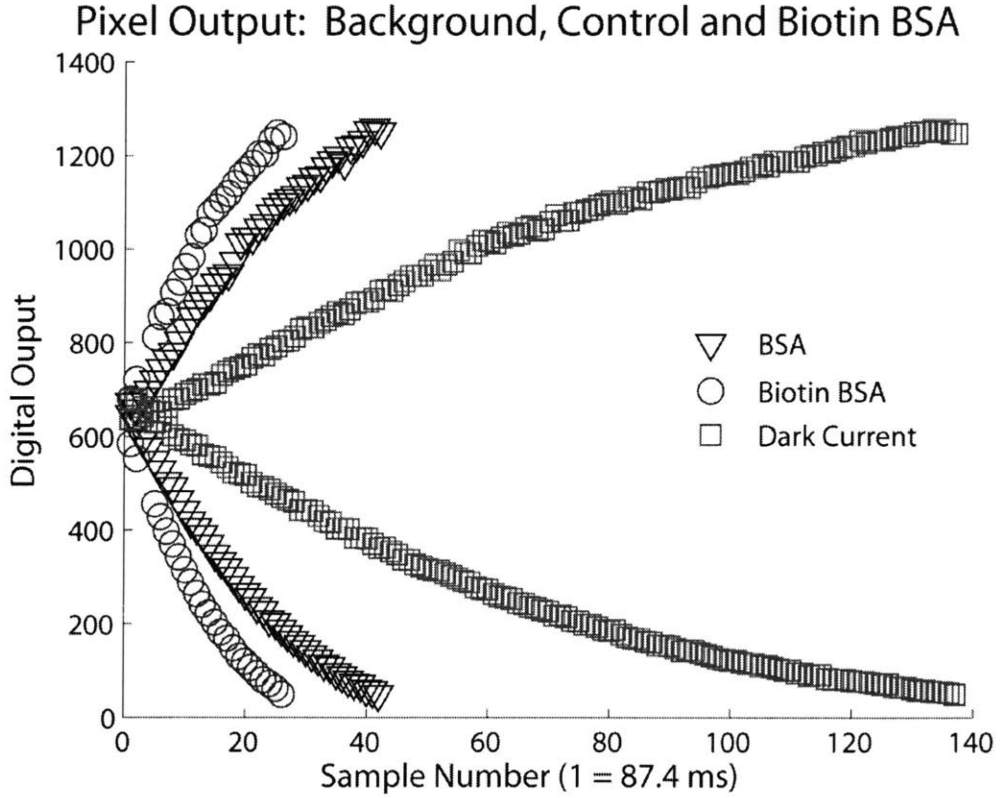
Pixel Output: Background, Control and Biotin BSA
Digital Ouput
1400
1200
1000
800
600
400
200
0
20
40
60
80
100
120
140
Sample Number (1 = 87.4 ms)
▽ BSA
○ Biotin BSA
□ Dark Current

Figure 59: Raw Data and Representative Traces

The upper pane shows the continuous raw data trace for the pixel output, and the lower pane shows representative samples from each region. The differential current is the least in the dark current region (6000-8000, gray) and the slope of the output versus sample number is the lowest. The BSA region (100-2500, Blue) contains the background light and any scattering due to the proteins themselves. The Biotin BSA region (2500-6000, red) has the steepest slope, indicating the greatest amount of light is received by the sensor. This light includes the background from the scattering, as well as the fluorescence from the evanescently illuminated quantum dots.

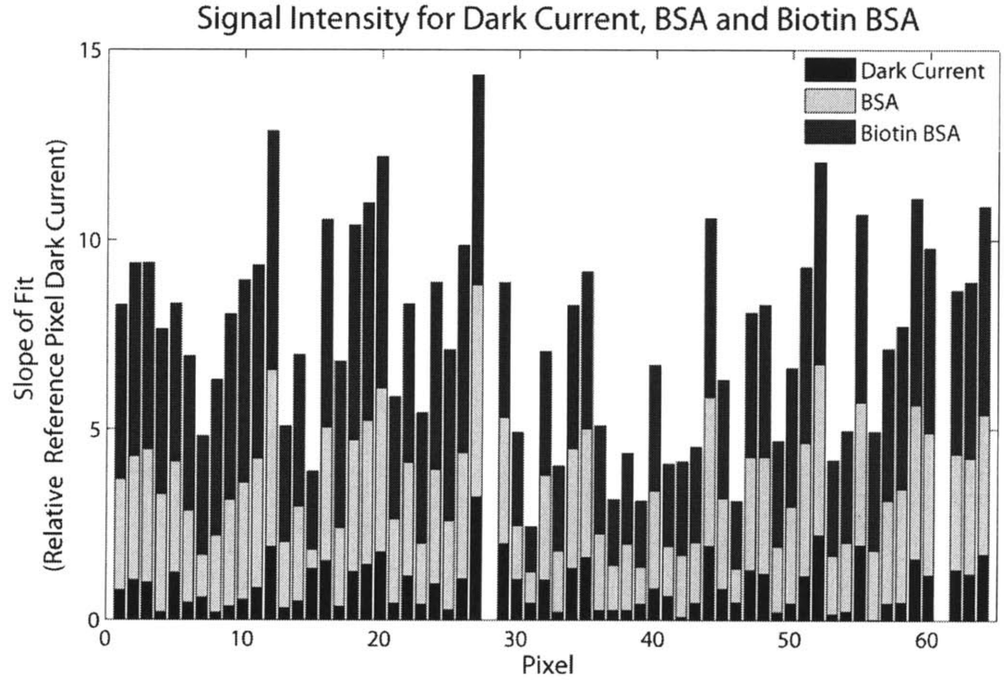

Figure 60: Relative Signal Intensity for All Pixels

The relative signal intensity for each pixel, for each region is shown. The dark current has the lowest value (absolute values plotted), while the BSA has increased intensity due to the scattering of the LED light. The Biotin BSA has the greatest signal, and includes the background scattering as well as the fluorescence from the quantum dots.

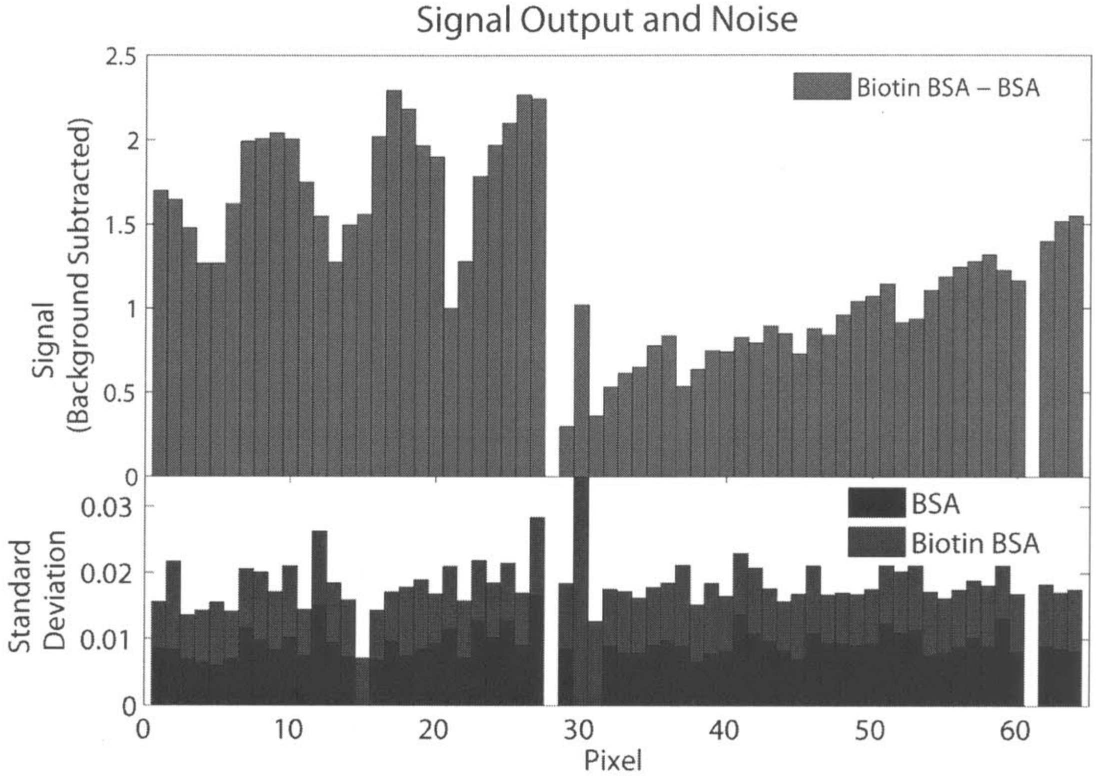

Figure 61: Net Signal and Standard Deviation of the Mean

The net signal is the Biotin BSA signal with the background BSA signal subtracted. The standard deviation of the mean is also give for both the positive signal and the background (negative control). For the most intense pixels, the signal to noise is ~ 100. The variation in pixel intensity is due to the non-uniformity of illumination as well as of the distribution of Biotin BSA on the coverslip.

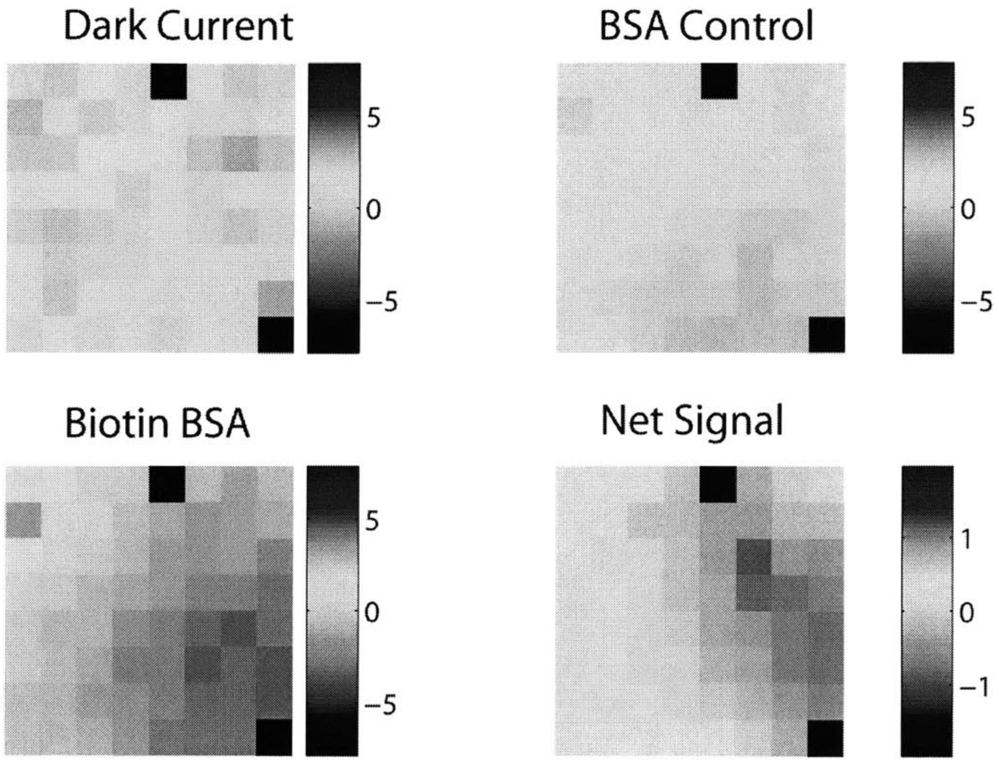

Figure 62: Pixel Data Mapped to Array Locations

The pixel data for background, BSA and Biotin BSA is mapped to the correct spatial location using the framing pixel. The dark current intensity is random, as is expected from nature of the photodiode mismatch. The BSA (negative) control intensity is several times the differential dark current intensity. Additionally, a region of higher intensity is seen at the lower part of the array, likely due to variations in illumination intensity from the LED. The Biotin BSA spot has an increased intensity over the background BSA. The net signal is the biotin BSA with the BSA background subtracted, divided by the illumination intensity. Note the net signal image is color scaled differently from the other arrays.

References

Ando, T., N. Kodera, et al. (2003). "A high-speed atomic force microscope for studying biological macromolecules in action." Chemphyschem **4**(11): 1196-202.

Ando, T., N. Kodera, et al. (2001). "A high-speed atomic force microscope for studying biological macromolecules." Proc Natl Acad Sci U S A **98**(22): 12468-72.

Barbaro, M. B., A.; Raffo, L.; (2006). A charge-modulated FET for detection of biomolecular processes: conception, modeling, and simulation. IEEE Transactions on Electron Devices.

Binnig, G., C. F. Quate, et al. (1986). "Atomic force microscope." Phys. Rev. Letts. **56**: 930-933.

Chen Xu, J. L., Yijin Wang, Lu Cheng, Zuhong Lu, M. Chan (2005). "A CMOS-compatible DNA microarray using optical detection together with a highly sensitive nanometallic particle protocol." IEEE Electron Device Letters **26**(4): 240-242.

Claudio Stagni, C. G., Luca Benini, Bruno Ricco, Sandro Carrara, Christian Paulus, Meinrad Schienle, Roland Thewes (2007). " A Fully Electronic Label-Free DNA Sensor Chip." IEEE Sensors Journal **7**(4): 577-585.

D. Baselt, G. U. L., M. Natesan, S.W. Metzger, P.E. Sheehan and R.J. Colton (1998). "A biosensor based on magnetoresistance technology." Biosensors and Biotechnology **13**: 731.

Eltoukhy, H. S., K.; Gamal, A.E. (2006). "A 0.18-/spl mu/m CMOS bioluminescence detection lab-on-chip." IEEE Journal of Solid-State Circuits **41**(3): 651-662.

G. Manning, D. B. W., R. Martinez, T. Hunter, S. Sudarsanam (2002). "The Protein Kinase Complement of the Human Genome." **298**: 1912-1934.

Goldsbury, C., J. Kistler, et al. (1999). "Watching amyloid fibrils grow by time-lapse atomic force microscopy." J Mol Biol **285**: 33-39.

Guthold, M., M. Bezanilla, et al. (1994). "Following the assembly of RNA polymerase-DNA complexes in aqueous solutions with the scanning force microscope." Proc Natl Acad Sci USA **91**: 12927-12931.

Gygi SP, R. B., Gerber SA, Turecek F, Gelb MH, Aebersold R (1999). "Quantitative analysis of complex protein mixtures using isotope-coded affinity tags." Nature Biotechnology **17**(10): 994-999.

H. Zhu, M. B., R. Bangham, D. Hall, A. Casamayor, P.Bertone, N. Lan, R. Jansen, S. Bidlingmaier, T. Houfek, T. Mitchell, P. Miller, R. A. Dean, M. Gerstein, M. Snyder (2001). "Global Analysis of Protein Activities Using Proteome Chips." Science **293**(5537): 2101-2105.

Haga, H., M. Nagayamam, et al. (2000). "Time-lapse viscoelastic imaging of living fibroblasts using force modulation mode in AFM." J Electron Microsc **49**: 473-481.

Hofmann, F. F., A.; Holzapfl, B.; Schienle, M.; Paulus, C.; Schindler-Bauer, P.; Kuhlmeier, D.; Krause, J.; Hintsche, R.; Nebling, E.; Albers, J.; Gumbrecht, W.; Plehnert, K.; Eckstein, G.; Thewes, R.; (2002). Fully electronic DNA detection on a CMOS chip: device and process issues. Electronic Devices Meeting, IEDM.

J. Olsen, B. B., F. Gnad, B. Macek, C. Kumar, P. Mortensen, M. Mann (2004). "Global, In Vivo, and Site-Specific Phosphorylation Dynamics in Signaling Networks." Cell **127**(3): 635-648.

Jensen, M. M. O. N. (2003). "Proteomic analysis of post-translational modifications." Nature Biotechnology **21**: 251-261.

Junmin Peng, D. S., Joshua E Elias, Carson C Thoreen, Dongmei Cheng, Gerald Marsischky, Jeroen Roelofs, Daniel Finley, & Steven P Gygi (2003). "A proteomics approach to understanding protein ubiquitination." Nature Biotechnology **21**: 921-926.

Malkin, A. J., Y. G. Kuznetsov, et al. (1996). "Incorporation of microcrystals by growing protein and virus crystals." Proteins **24**: 247-252.

Mann M, O. S., Grønborg M, Steen H, Jensen ON, Pandey A. (2002). "Analysis of protein phosphorylation using mass spectrometry: deciphering the phosphoproteome." Trends Biotechnology **20**(6): 261-268.

Mann, S.-E. O. a. M. (2007). "A practical recipe for stable isotope labeling by amino acids in cell culture (SILAC)." Nature Protocols **1**: 2650-2660.

Niroshan Ramachandran, E. H., Bhupinder Bhullar, Samuel Eisenstein, Benjamin Rosen, Albert Y. Lau, Johannes C. Walter, Joshua LaBaer (2004). "Self-Assembling Protein Microarrays." Science **305**(5690): 86-90.

Ong SE, B. B., Kratchmarova I, Kristensen DB, Steen H, Pandey A, Mann M. (2002). "Stable isotope labeling by amino acids in cell culture, SILAC, as a simple and accurate approach to expression proteomics." Molecular and Cellular Proteomics **1**: 376-386.

P-A. Besse, G. B., M. Demierre, V. Pott and R.S. Popovic (2002). "Detection of a single magnetic microbead using a miniaturized silicon Hall sensor." Applied Physics Letters **80**: 4199.

Radmacher, M., M. Fritz, et al. (1994). "Direct observation of enzyme activity with the atomic force microscope." Science **265**(5178): 1577-9.

Richard B. Jones, A. G., Jordan A. Krall and Gavin MacBeath (2006). "A quantitative protein interaction network for the ErbB receptors using protein microarrays." Nature **439**: 168-174.

Ron Bose, H. M., A. Scott Patterson, John K. Bitok, Balamurugan Periaswamy, Joel S. Bader,, Akhilesh Pandey, and Philip A. Cole (2006). "Phosphoproteomic analysis of Her2/neu signaling and inhibition." PNAS **103**(26): 9773-9778.

Ross PL, H. Y., Marchese JN, (2004). "Multiplexed protein quantitation in Saccharomyces cerevisiae using aminereactive
isobaric tagging reagents." Molecular and Cellular Proteomics **3**: 1154-1169.

Rousso, I., E. Khachatryan, et al. (1997). "Microsecond atomic force sensing of protein conformational dynamics: implications for the primary light-induced events in bacteriorhodopsin." Proc Natl Acad Sci U S A **94**: 7937-7341.

Rousso, I., E. Khatchatryan, et al. (1997). "Atomic Force Sensing of Light-Induced Protein Dynamics with Microsecond Time Resolution in Bacteriorhodopsin and Photosynthetic Reaction Centers." J Struct Biol **119**: 158-164.

Rousso, M. A. a. I. (2005). "Atomic force microscopy with time resolution of microseconds." Applied Physics Letters **86**(014101).

S. P. Gygi, Y. R., B. R. Franza, R. Aebersold (1999). "Correlation between protein and mRNA Abundance in Yeast." Molecular and Cellular Biology **19**(3): 1720-1730.

Sarpeshkar, M. O. H. a. R. (2004). "A 10-nW 12-bit Accurate Analog Storage Cell with 10-aA Leakage." Journal of Solid State Circuits **39**(11).

Schoenenberger, C. A. and J. H. Hoh (1994). "Slow cellular dynamics in MDCK and R5 cells monitored by time-lapse atomic force microscopy." Biophys. J. **67**: 929-936.

Schreiber, G. M. a. S. L. (2000). "Printing Proteins as Microarrays for High-Throughput Function Determination." Science **289**(5485): 1760-1763.

Scofield, B. T. K. a. R. H. (1997). "Western Blotting." J. Immunol. Method **205**: 91-94.

Scofield, B. T. K. a. R. H. (2006). "Western Blotting." Methods **38**(4): 283-293.

Scott B. Ficarro, M. L. M., P. Todd Stukenberg, Daniel J. Burke, Mark M. Ross, Jeffrey Shabanowitz, Donald F. Hunt, & Forest M. White (2002). "Phosphoproteome analysis by mass spectrometry and its application to Saccharomyces cerevisiae." Nature Biotechnology **20**: 301-305.

Stoffler, D., K. N. Goldie, et al. (1999). "Calcium-mediated structural changes of native nuclear pore complexes monitored by time-lapse atomic force microscopy." J Mol Biol **287**: 741-752.

Stolz, M., Stofflerm D, et al. (2000). "Monitoring biomolecular interactions by time-lapse atomic force microscopy." J Struct Biol **131**: 171-180.

Thewes, R. H., F.; Frey, A.; Holzapfl, B.; Schienle, M.; Paulus, C.; Schindler, P.; Eckstein, G.; Kassel, C.; Stanzel, M.; Hintsche, R.; Nebling, E.; Albers, J.;

Hassman, J.; Schulein, J.; Goemann, W.; Gumbrecht, W.; (2002). Sensor arrays for fully-electronic DNA detection on CMOS. IEEE International Solid-State Circuits Conference, San Francisco.

Turgut Aytur, J. F., Mekhail Anwar, Bernhard Boser, Eva Harris and P. Robert Beatty (2006). "A novel magnetic bead bioassay platform using a microchip-based sensor for infectious disease diagnosis." Journal Of Immunological Methods **314**(1-2): 21-29.

Ushiki, T., J. Hitomi, et al. (1999). "Imaging of living cultured cells of an epithelial nature by atomic force microscopy." Arch Histol Cytol **62**: 47-55.

Walsh, C. (2006). Posttranslational Modification of Proteins: Expanding Nature's Inventory, Roberts and Co. Publishers.

Chapter 6: Wireless Interface

The circuit described in the previous chapters is designed to be powered via a wireless interface. Here we demonstrate the ability to transmit power and data wirelessly to and from the device, respectively.

The transmitter circuitry (Figure 63) is a series R-L-C, with the resistance being the output resistance of the amplifier plus the series resistance of the inductor. If a core is used, the real component of the permeability also contributes to the (real) resistance.

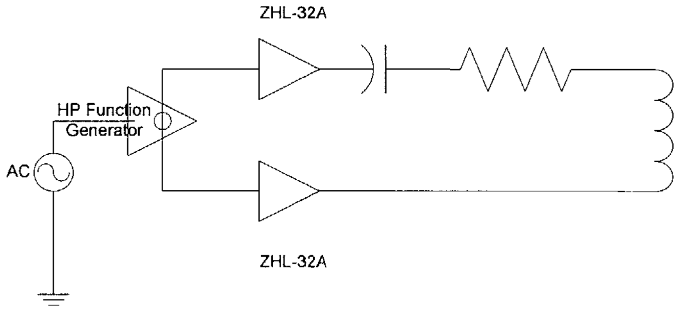

Figure 63: Transmitter Schematic

Admittance as a function of frequency can be written as

$$Y(s)=\frac{s}{L\left(s^2+2\delta s+w_0^2\right)}$$

where $\omega_0=\frac{1}{\sqrt{LC}}$,and $\delta=\frac{2R}{L}$. When the circuit is excited at resonance, $s=j\omega_0$, is has the minimum impedance, and therefore the maximum current flows for a given excitation voltage. The current flowing through the inductor generates a magnetic field. The magnetic field generated from an inductor (on the symmetric axis) with *N* turns can be written as can be written as

$$B_z(z)=\frac{\mu_0 N I r^2}{2\left(r^2+z^2\right)^{3/2}}$$

where *r* is the radius of the coil, *I* is the current through the loop, and *z* is the distance from the center of the loop (along the symmetric axis).

Power is transmitted to the receiver coil by generating a voltage on the coil. Lenz's law states that a changing magnetic field will be opposed by an induced current, which is created by the induced voltage and pushed through the resistance of the coil.

$$V_{emf}=I_{ind}R_{coil}$$

If we return to the diagram of the coil, we can see that the resistance of the coil should also include the resistance of the circuit. Furthermore, the voltage delivered to the circuit (or load resistance) is resistively divided between the series resistance of the coil and the effective resistance of the circuit.

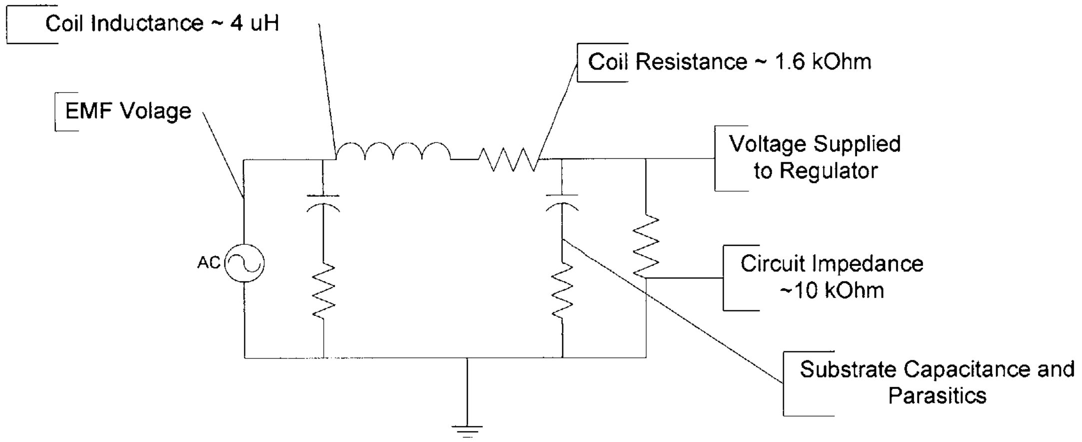

Figure 64: Receiver Coil Schematic

Wireless Power Transmission

Voltage is generated on the inductor by the inductor acting to oppose changes in flux. Current generates a magnetic field, and so induced current can generate a field that acts to oppose the change in magnetic field. Therefore, alternating field can induce a voltage. The voltage induced is

$$V = -\frac{\partial \Phi}{\partial t}$$

$$\Phi = LI$$

Where Φ is the flux, *L* is the inductance, and *I* is the current. For a coupled set of inductors (*P* denoting the primary, and *S* denoting the secondary),

$$\Phi_S = MI_P$$

Referring to Figure 64, the *pi* model for an inductor gives (V_c is the voltage induced on the chip, M is the mutual inductance, I_p is the current in the primary/transmitter coil, I_s is the current in the secondary/chip, and R is the resistance of the secondary inductor coil, R_L is the resistance of the chip, and C_s is the substrate capacitance.)

$$V_C = M\omega I_P - L_S\omega I_S - I_S R = \frac{I_S R_L}{1+\omega R_L C_S}$$

$$V_C = \frac{I_S R_L}{1+\omega R_L C_S} = \frac{M\omega I_P\left(\dfrac{R_L}{1+\omega R_L C}\right)}{\omega L_S + R_S + \dfrac{R_L}{1+\omega R_L C}}$$

$$V_C = \frac{M\omega I_P R_L}{R_L + R_S + \omega L_S + \omega R_S R_L C + \omega^2 R_L C L_S}$$

$$V_C = \frac{M\omega I_P}{1+\dfrac{R_S}{R_L} + \omega R_s C\left(1+\omega\dfrac{L_S}{R_S}\right)}$$

$$V_C = \frac{M\omega I_P}{1.5+\omega R_s C} \cong \frac{2M\omega I_P}{3}$$

Using ASITIC, the inductor parameters were identified. The parameters are included below. The inductor is made of m3, m4 and m5. The properties are listed below. The total capacitance is approximately 20 pF. The DC inductance is 4.6 μH, and the calculated resistance is 1.24 kOhm.

Table 9: IC Material Properties

Layer	Distance to Poly	Cap (aF/um^2)	Sheet Res mOhm/s	Thickness (nm)	Width (um)	Length (um)	Area	Capacita (pF) (effective)
M3	2693 nm	13.2	72	471	1.6	3470	1.066e6	14
M4	3764	9.4	72	471	4	3470	1.11e6	6.26
M5	4836	7.3	36	860	4	3470	1.11e6	0

Table 10: Ascitic Simulation Results

Freq	Turns	Width	Spacing	Metal	Dimension	Rs	Cs	L	R	Resonance
1M	20	5	1	M3/M5	3.5 mm	195	28p	18u	1.3k	7M
8M	20	5	1	M3/M5	3.5 mm	195	13p	10u	1.2k	13.8M
10M	20	4	1	M3/M5	3.5mm	181	8.3p	8u	1.1k	19.5M

Data Transmission

The transmission of digital data from the chip to the receiver utilizes a modulated data stream sent out via the RF coil. The data is modulated by $\frac{f_{clk}}{2}$ and this signal causes 100 μA to be pulled from the RF coil. The data bandwidth is $\frac{f_{clk}}{2^6}$, and when modulated the data moves to a $\frac{f_{clk}}{2} \pm \frac{f_{clk}}{2^6}$. In Figure 65, the red signal indicates the data, while the green indicates the RF excitation signal. When the signal is multiplied by $\frac{f_{clk}}{2}$, the data moves to DC, and can be recovered by low-pass filtering.

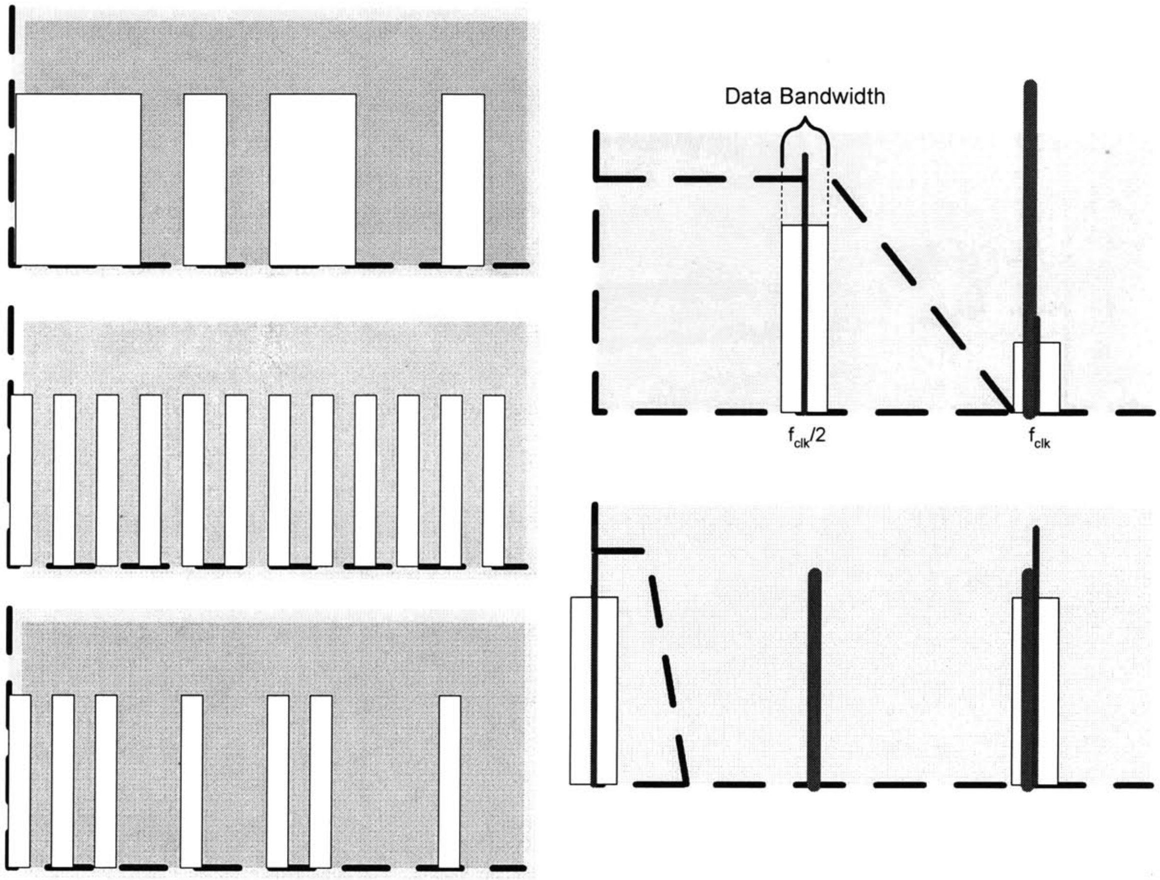

Figure 65: Data Modulation

The time domain is depicted on the left, and the frequency domain on the right. Raw data is shown in the top pane, and is multiplied by a signal that is at ½ of the clock (RF excitation) frequency. The resulting signal is shown in the bottom pane. It is this signal that is output on the inductor coil. The frequency domain diagrams also illustrate this. The data signal is located at $f_{clk}/2$, with a bandwidth of $f_{clk}/2^6$.. The signal detected on the receiver coil has this signal (i.e. the data) and the RF excitation signal. The signal is filtered, and multiplied by a sine wave at $f_{clk}/2$, moving the signal to DC, where is it again filtered and read by a data acquisition card.

Test Setup

The test setup uses a HP function generator to power two Minicircuits ZHL-32A (each 180 out of phase with the other), which are connected to a wire-wound inductor (gauge 28 magnet wire, 1 ft length) in series with a capacitor. The receiver consists of a Coilcraft 100 µH inductor in parallel with a capacitor. The resonant frequency of the receiver is set to f/2 to receive the modulated output. The differential output is then connected to a differential to single ended amplifier (MAX4145, $A_v = 2$). The amplifier output is low pass filtered and then amplified to further remove the excitation RF signal. The signal is then multiplied by f/2 to move the signal to DC where is it low pass filtered again.

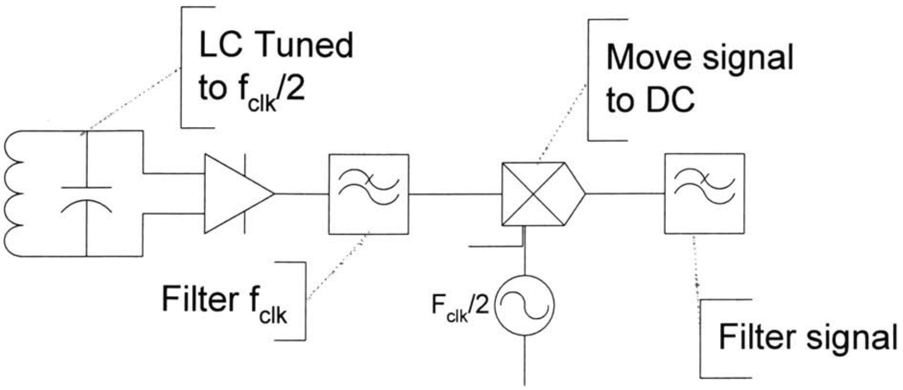

Figure 66: Receiver Schematic

An example of the receiver operation (using the on-chip inductor) is shown below. The data (blue) is shown after multiplication with $\frac{f_{clk}}{2}$. The subsequent figure shows the filtered (via MATLAB) trace. The green is the digital signal recorded directly from the chip.

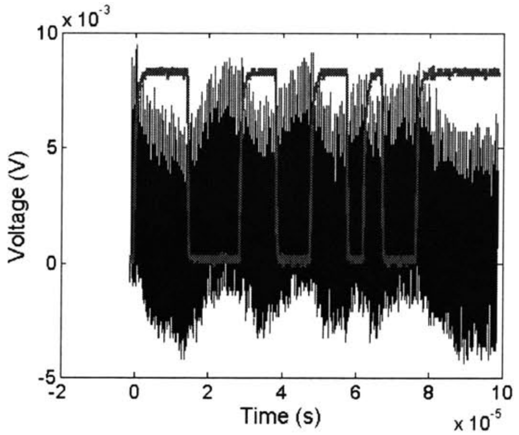

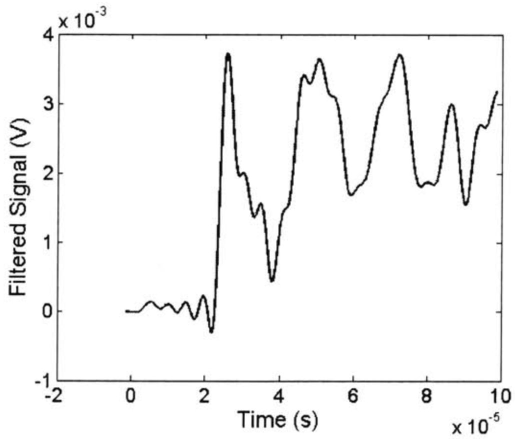

Modified Antenna

There was difficulty in supplying sufficient power to the chip, and an external coil (antenna) was added in parallel to the on-chip inductor by soldering a coil made of 28 gauge magnet wire onto the chip package. Using this external coil, wireless power and data transmission was achieved. Data reception is shown in Figure 67. The data output measuring dark current for a representative pixel is shown in Figure 68.

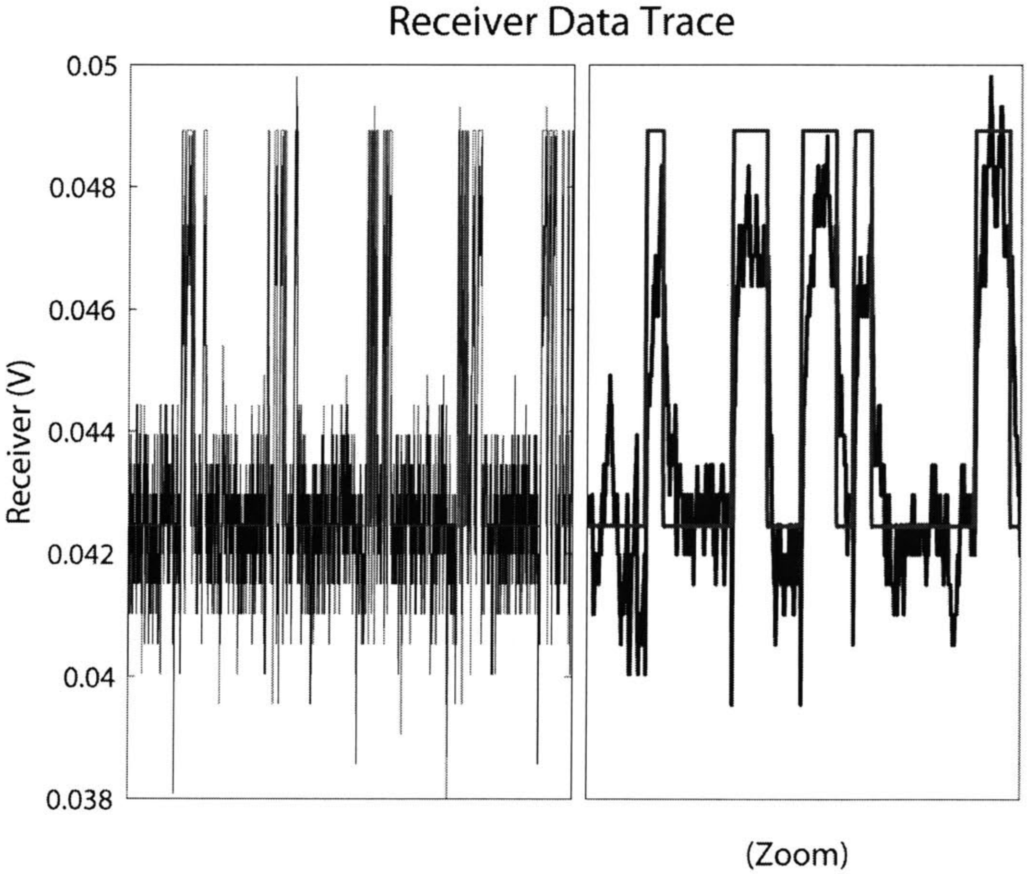

Figure 67: Receiver Data Trace

The RF excitation is filtered and the remaining signal is amplified. The signal is multiplied by a sine wave at ½ the excitation frequency (the data modulation frequency), and output to a high speed data acquisition card. Shown here is the data trace recorded directly from the chip (red) and the RF signal received (blue).

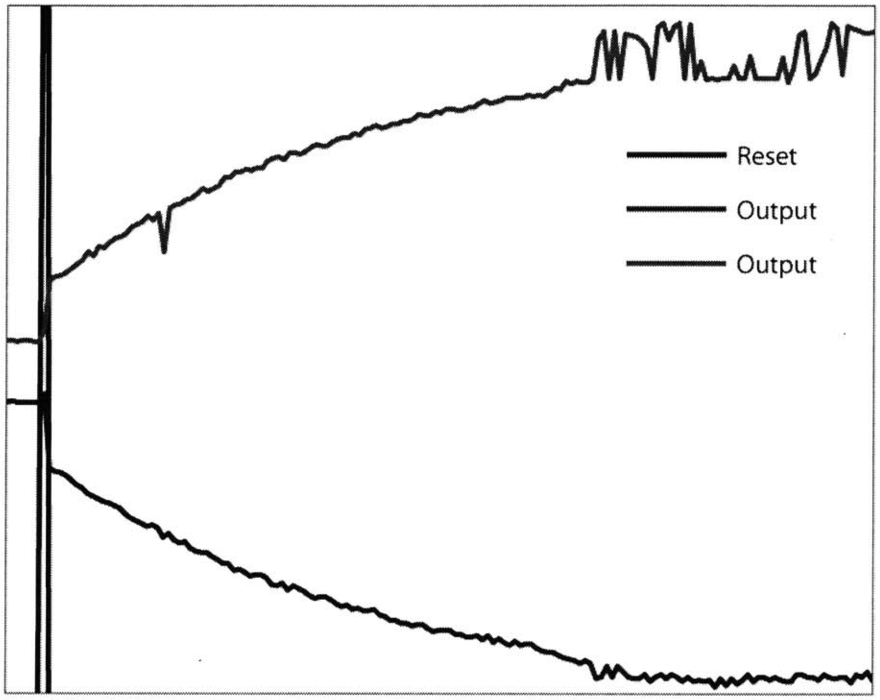

Figure 68: Wireless Data Output

Conclusion

We have demonstrated wireless power transfer and data transmission from the optical µarray. The on-chip coil is not sufficient (in terms of resistance, capacitance, Q) to power the circuit and an external inductor was required. This inductor consists of a simple coil (~ 20 turns) of a 28 gauge magnet wire, attached to the package. The on-chip coil is in parallel with this coil. The on-chip coil can be disconnected via FIB or laser cutter if necessary.

Summary

The study of biological systems can no longer be limited to single pathways, or single components. Biological systems are complex interconnected networks, and understanding how each component responds, regulates or is governed by its environment is crucial to understanding biological processes. This thesis has developed tools to allow some of these questions to be answered.

Atomic force microscopy provides unparalleled images in terms of spatial resolution, but is traditionally limited to static images. The movement of biological processes, such as proteins or more complex systems such as the tectorial membrane, exhibit angstrom level motion. To bridge this gap, we present a technique to enable atomic force microscopy imaging with microsecond time resolution, and demonstrate this on an AFM calibration grid.

As proteins move, they interact with their environment, often consisting of other proteins and small molecules. We develop a high throughput method to screen for these interactions by patterning proteome-scale microarrays. Protein µarrays have been limited in use due to the need to clone and purify thousands of individual proteins. By utilizing a cellular lysate, we leverage an existing source of synthesized proteins, containing all potential interaction partners for a selected target. Additionally, protein post-translational modifications are crucial to protein (and consequently cellular) function, making them important to integrate with µarray patterning. We further integrate the protein µarrays with quantitative

mass spectrometry, enabling identification and measurement of differential protein expression. We demonstrate this technique by examining the Erb1 and Erb2 receptors in response to EGF and Heregulin, respectively. We monitor the time course of internal signaling by visualizing the phosphoproteome, and probe for multiple post-translational modifications using our μarray format integrated with mass spectrometry.

Finally, we introduce a method to image standard μarrays (with optical labels) without the use of filters or lenses. By implementing an optics-free μarray reader in CMOS technology, the cost of the reader can be significantly reduced. This will allow μarray technology to be widely adopted, enabling screening and diagnostic applications to be developed and used in a wide variety of settings. We have demonstrated the reader with a prototype "array", imaging 20 nM fluorescently labeled streptavidin binding to biotin. Furthermore, the chip is powered via sine wave, enabling remote, wireless operation.

Taken together, this thesis develops a set of tools to investigate the protein dynamics, interaction and identification. It is the hope of the author that these techniques will assist others in their quest to understand biological systems.

Appendix 1: Microsecond Time-resolved Atomic Force Sensing Mapping

This work was done in collaboration with Itay Rousso (Weizmann Institute, Dept. of Structural Biology). Portions of this work have been previously published (Rousso 2005).

Abstract

Imaging dynamic processes, as they occur in real-time, is a powerful avenue in microscopy that helps us understand their mechanism. The atomic force microscope (AFM) can acquire high resolution images under non-destructive conditions but with very poor temporal resolution. This work presents a novel atomic force sensing mapping technique for imaging rapid processes with nanometer spatial resolution and microsecond time-resolution using a commercial microscope. Two methods are described: the stroboscopic and the continuous time resolved AFM. Both techniques require a system whose motion is periodic, and utilize that fact by imaging the full cycle of motion of each point, before moving on to the next point. The AFM probe steps along a virtual grid overlaying the specimen. The motion of the entire sample is then reconstructed by arraying together the motion traces from each point. Vertical resolution is obtained by averaging over many cycles (stroboscopic mode) or filtering out-of-

band noise (continuous mode). Time resolution is only limited by the resonant frequency of the cantilever, and is independent of the area of interest size. Application of these techniques is demonstrated for imaging very rapid cyclic changes in the position of a microfabricated grid mounted. Motion was resolved with 10 nm spatial resolution and 3 μsec and 40 μsec using the stroboscopic and continuous mode respectively. In summary a new tool is described for monitoring dynamics of materials with wide applicability to fundamental and applied science.

Background

The atomic force microscope (AFM) (Binnig, Quate et al. 1986) is probably the most versatile member of the scanning probe microscopes family. It can acquire images at a resolutions range achieved by the electron microscope, but under physiological non-destructive conditions. The AFM has therefore, the potential to image biological systems in real time, under natural conditions, with molecular resolution. Unfortunately, the temporal resolution of the AFM imaging is limited to the lateral scanning speed and therefore extremely poor (tens of seconds). Several studies have demonstrated that the AFM can be used to image slow dynamical processes in living cells (Schoenenberger and Hoh 1994; Ushiki, Hitomi et al. 1999; Haga, Nagayamam et al. 2000) and other biological systems (Guthold, Bezanilla et al. 1994; Malkin, Kuznetsov et al. 1996; Goldsbury, Kistler et al. 1999; Stoffler, Goldie et al. 1999; Stolz, Stofflerm D et al. 2000) with time resolutions ranging from minutes to hours. Recently a custom made, high-speed scanner was developed that is capable to capture a 100 x 100 pixel image within

80 msec (Ando, Kodera et al. 2001; Ando, Kodera et al. 2003). Much higher time resolutions are obtained when the AFM is used in the force sensing mode to detect vertical displacements from a single site. In this mode, the temporal resolution was initially ~1 msec, (Radmacher, Fritz et al. 1994) which was later improved to few microseconds (Rousso, Khachatryan et al. 1997; Rousso, Khatchatryan et al. 1997).

Here we present a novel methodology to obtain time-resolved AFM imaging based on the step-scan technique. In this method, an array of individual force sensing measurements is used to reconstruct topographic images. Similarly to the force sensing mode, the temporal resolution is limited only by the cantilever resonance frequency, the data acquisition electronics, and is independent of the scanned area. With this technique we have successfully imaged the surface of a calibration grid which was mounted on a piezo-crystal during fast oscillatory motion. Two methods are described for data acquisition and analysis: (1) the stroboscopic and (2) continuous mode step-scan time-resolved AFM, denoted as STR-FM and CTR-FM respectively. Both modes can be employed to image only periodic processes. However, in contrast to STR-FM, CTR-FM does not require synchronization between the data acquisition hardware and the sample motion, and therefore can be applied on a wider range of systems. With the stroboscopic mode, motions of the grid oscillating at 5 KHz frequency were resolved with 10 nm spatial and 5 μsec temporal resolutions. Oscillations at 1 KHz frequency were resolved at 10 nm and 25 μsec resolutions with the continuous mode.

Our achievements open up the possibility of imaging, in real time rapid structure dynamics in high resolution. Time-resolved AFM imaging has the potential to shed new light on the study of rapid dynamical processes occurring particularly but not limited in biology.

Experimental

Schematic representation of the apparatus used to develop time-resolved atomic force sensing mapping technique is shown in Figure 69. In this work we image the surface of a calibration grid (150-1D) made of aluminum lines etched on glass separated (see Figure 69 lower panel) by 150 nm distance (Advanced Surface Microscopy, Indianapolis, IN). The grid was mounted on a piezo-electronic actuator controlled by a piezo driver (ThorLabs, Newton NJ; Model MDT694), and a function generator (Agilent, Palo Alto, CA; Model 33120A).

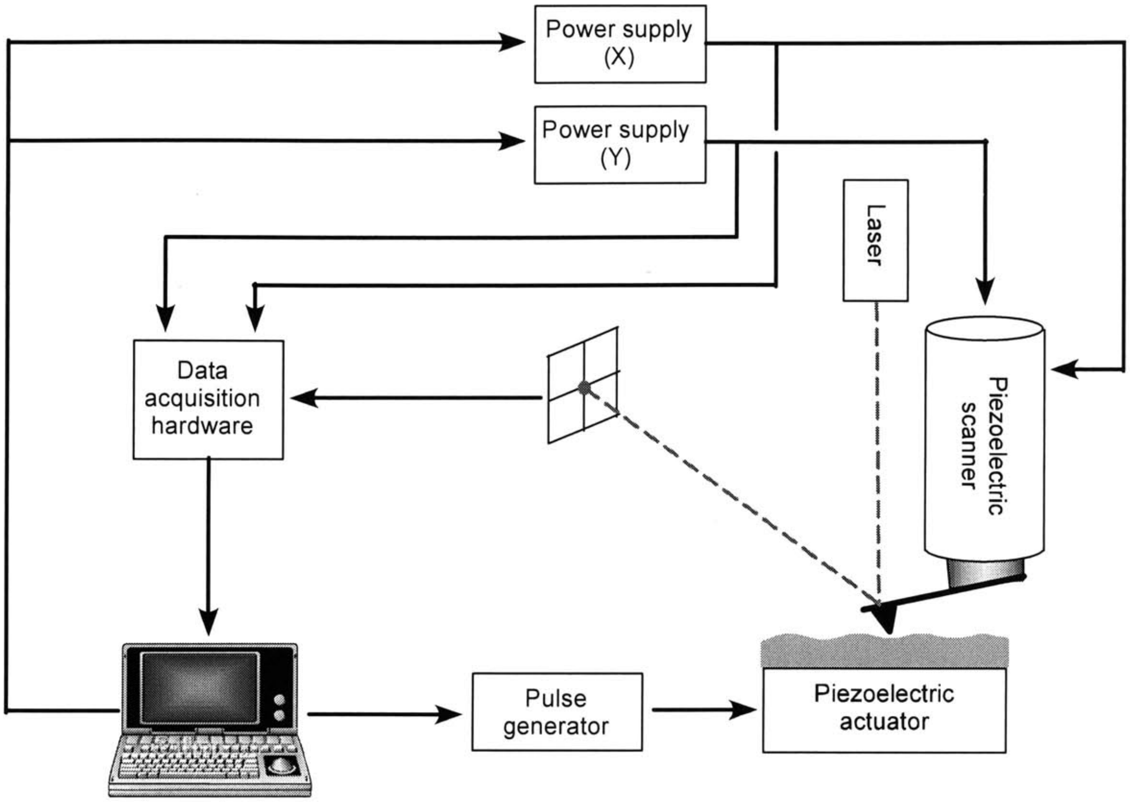
Power supply
(X)
Power supply
(Y)
Laser
Data acquisition hardware
Piezoelectric scanner
Pulse generator
Piezoelectric actuator

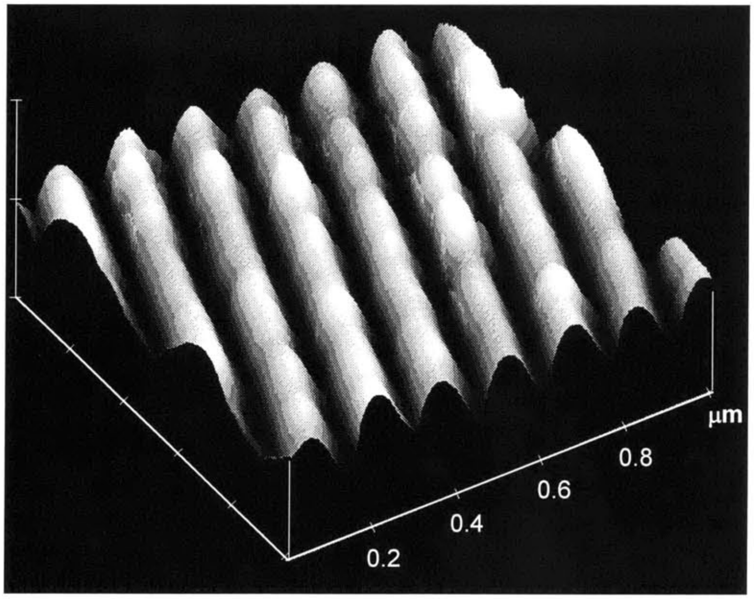
μm
0.8
0.6
0.4
0.2

Figure 69: Time Resolved AFM Experiment Setup and Calibration Grid

Schematic drawing of the experimental setup (upper panel). The microscope's piezo-scanner is driven in a step-wise fashion by either computer controlled power supplies or the Nanolithography software. Deflection of the cantilever is measured from the PSD using a digitizing oscilloscope or a data acquisition card. The sample (etched calibration grid) is mounted on external piezoelectric actuator. Motion is introduced by oscillating the piezo using a function generator. A 1 × 1 μm^2 AFM image of the calibration grid is shown in the lower panel.

In our experiments we used a commercial force microscope (Veeco, Santa-Barbara, CA; Model Bioscope). To drive the cantilever in a step-wise manner, DC voltage offset was applied to either the X or Y piezo scanner. In the stroboscopic method this was achieved by two external power supplies (Agilent, Palo Alto, CA; Model 3645A), while in the continuous mode, a closed-loop scanner controlled by the Nanolithography software (Veeco, Santa-barbara, Version 5.12) was used. Motion was introduced by application of a sine wave by the function generator to the piezo actuator which supports the sample.

To measure the vertical displacement of the sample, a commercially available silicone-nitride force tip (Veeco, Santa-barbara, CA) was brought in contact with the sample surface. Similarly to the atomic force sensing experiments (Rousso, Khachatryan et al. 1997; Rousso, Khatchatryan et al. 1997), the vertical motion was detected by directly monitoring the voltage alterations in the position sensitive detector (PSD) caused by cantilever deflections. These time alterations in the PSD were recorded using a digital oscilloscope (Agilent, Palo Alto, CA; Model 54624A) and a data acquisition card (National Instruments, Austin, TX) in the stroboscopic and the continuous mode respectively. The entire experimental setup was controlled by a computer running the LabView software (National Instruments, Austin, TX). Data processing, data analysis, image reconstruction, and time-lapse movie rendering were done using Matlab software (Mathworks, Natick, MA).

Methods and Results

We introduce two methods to achieve micro-second time-resolved imaging with a standard commercial AFM: the Stroboscopic Time-Resolved AFM, and the Continuous Time-Resolved AFM. Both methods are based on imaging periodic processes, with the ability to obtain the motion of each point on the sample individually. The movement of the entire sample is reconstructed by arraying the time-lapse images of each point together according to their spatial location. The differences in the two methods lie primarily with regards to the characteristics of the sample motion: if each cycle of the motion can be externally triggered, the stroboscopic method is the appropriate method to use, otherwise the continuous time method should be used.

Stroboscopic time-resolved AFM

In the strobososcopic method, the Piezo and PSD data are collected directly from the AFM. Initially, the AFM cantilever is moved in a stepwise fashion along a virtual matrix overlaying the sample, while it is at rest. The voltage data from the Z-Piezo (termed the DC value) is taken at each point, and a stationary topographic image, denoted as the DC image, is reconstructed. Next, the motion of the sample is continuously triggered (i.e. strobed) by an external source, and the cantilever is stepped backwards over the same virtual grid. In our experimental setup, an electrostatically actuated piezo, with attached calibration grid, is oscillated at 5 kHz via a function generator. At each point, the vertical motion is recorded directly from the PSD while the cantilever is at rest for a duration set by the required signal to noise ratio. With this setup, a duration of ~15 msec was required to acquire 64 cycles. The PSD data is fed into the oscilloscope which averages the data using the same triggering signal that actuates the Piezo/Calibration grid sample. By averaging, noise can be eliminated allowing very small motion to be imaged. The averaged trace for the pixel is stored, the cantilever moves to the next pixel, and the process repeats. At the conclusion of the scan, a trace of the AC motion of each pixel is obtained. In the stroboscopic method, the system returns to its resting state before the probe is moved to the following pixel, ensuring that each pixels motion trace begins from the resting state. The DC value of each pixel (obtained from the DC image) is then combined with its AC motion to reconstruct a complete time lapse image of the sample, including both motion and surface features. With the motion of each pixel recorded and the knowledge that all pixels are in phase with each other, it is a simple matter to array all of the time-lapse images together and reconstruct an image of the motion of the entire sample. Figure 70 shows a snapshots taken from the time-lapse movie showing the surface topographic image after 500 microseconds.

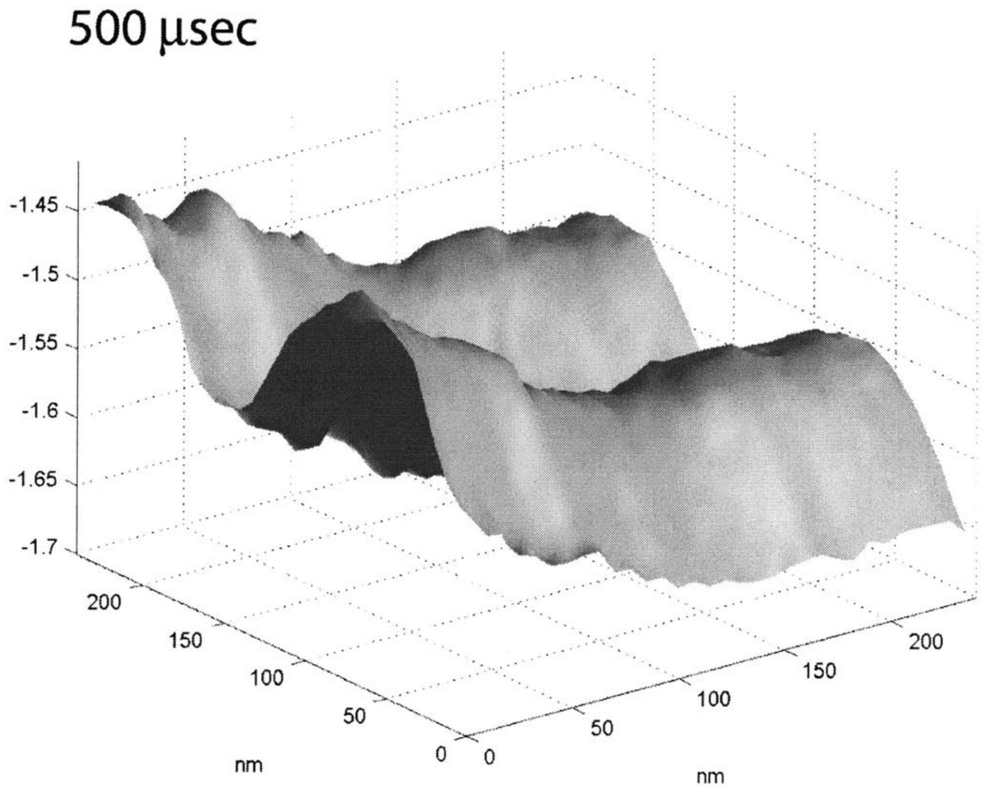

Figure 70: AFM Time Lapse Movie of Calibration Grid

A representative frame from the time-lapse movie of the sample motion measured with the stroboscopic time-resolved AFM method. The image is reconstructed from 484 pixels (22 × 22) which are 10 nm apart. Overall the image covers an area of 220 × 220 nm^2.

Continuous time-resolved AFM

Although the motion of many interesting systems can be repetitively triggered after each cycle, for others it is technically challenging or impossible. In order to extend time-resolved AFM to a wider variety of systems, we present a continuous time-resolved AFM methodology. In this method, data is continuously gathered and the requirement for resetting the system after each cycle (i.e. strobing) is eliminated. As in the stroboscopic method, the DC image is obtained by stepping through a virtual grid overlaying the sample while the sample is at rest. Sample motion is then initiated, and the cantilever is stepped backwards along the same virtual grid. Unlike the stroboscopic method, the sample undergoes a continuous cyclical motion as the AFM cantilever records the movement and steps from point to point. A 4 second window from the data stream is shown in Figure 71. The data stream consists of four channels: the lateral coordinates of the cantilever's position (Figure 71 A and B), the Z-Piezo and PSD signals (Figure 71 C and D). Each data point is recorded with the time of acquisition. The data represents a continuous trace of the samples movement, with each pixels motion concatenated with the next.

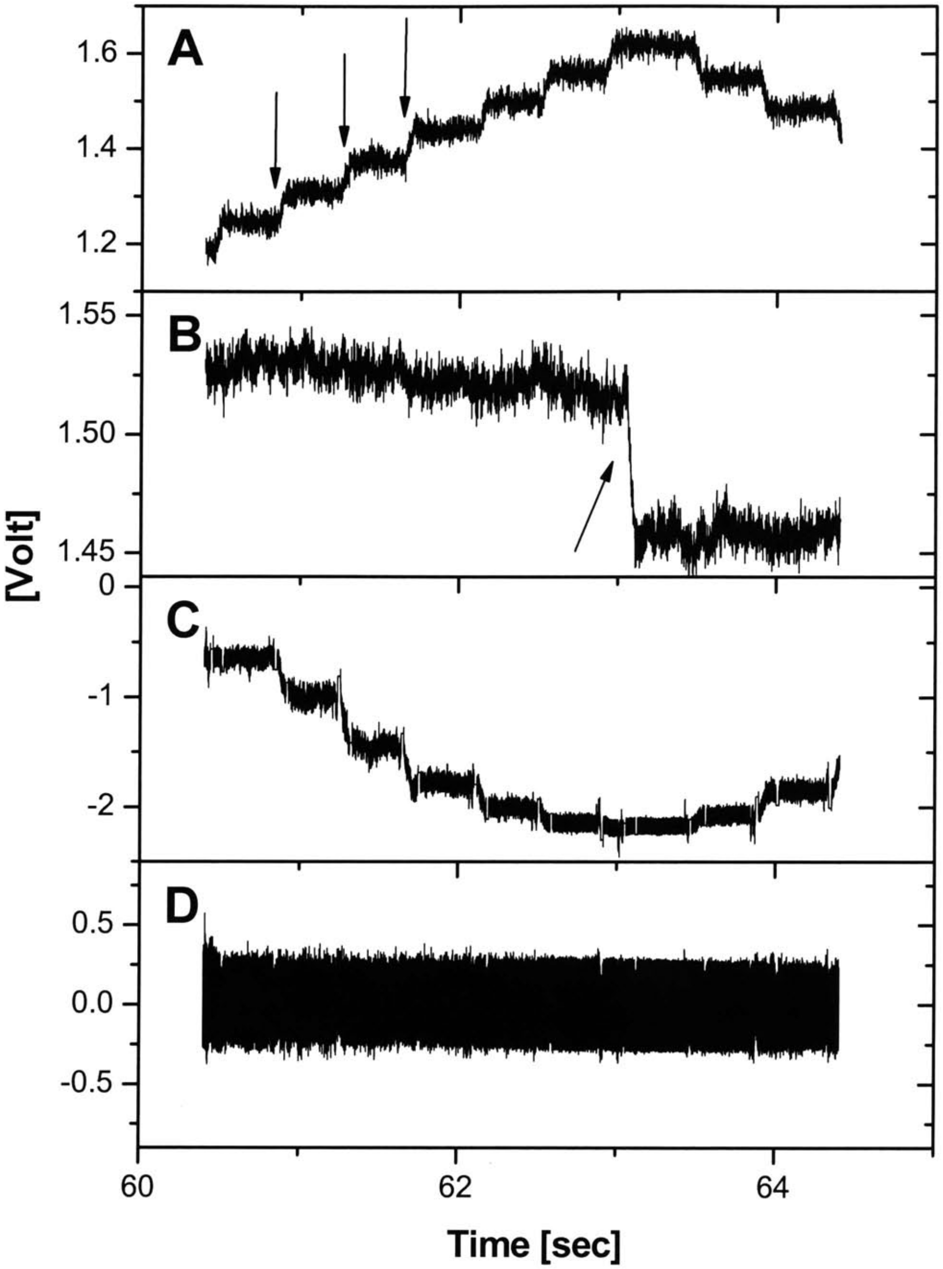
A
B
C
D
1.6
1.4
1.2
1.55
1.50
1.45
0
-1
-2
0.5
0.0
-0.5
[Volt]
60
62
64
Time [sec]

Figure 71: Raw Data for Continuous Time AFM

Four seconds representative sample of the data stream recorded in the continuous mode. (A) and (B) show the voltages corresponding to the x-position and y-position of the cantilever, respectively. Each voltage step corresponds to 10 nm, and location on the grid can be determined from the voltage levels of the A and B traces. The Z-Piezo and PSD signal are shown in (C) and (D), respectively. All four channels of time-stamped data are streamed continuously and stored, as the cantilever moves over a virtual grid overlaying the sample. At each transition (marked by arrows), the entire data stream is cut and each segment of data corresponds to the motion of a particular point on the sample. The Z-Piezo records slow motions and the DC characteristics of the sample, while the PSD shows the rapid motions.

In order to reconstruct images of the surface motion from the complete stream of data, three tasks must be performed: (1) fragmentation of the data into individual pixels, (2) noise filtering, and (3) phase alignment of each pixels motion. The first task, separation of pixels, is accomplished by noting the time point at which the cantilever is moved to a new position, and separating the data stream at those points (Fig. 3 A and B, Arrows). Each fragment of the original data stream represents the data recorded for an individual pixels motion.

The second task, noise filtering, was accomplished in the stroboscopic method by averaging the sample motion over many cycles using the triggering signal. In the continuous time method, we make use of the property that any periodic signal can be represented by a linear combination of sines and cosines whose frequencies are at the harmonics of the fundamental frequency.

$$s_{x,y}(t)=a_{0_{x,y}}+\sum_{k=1}^{\infty}b_{k_{x,y}}\cos(k2\pi f_0 t)+\sum_{k=1}^{\infty}c_{k_{x,y}}\sin(k2\pi f_0 t)$$

where $a_{0_{x,y}}$ is a DC offset, and $b_{k_{x,y}}$ and $c_{k_{x,y}}$ are coefficients for each harmonic of each pixel. In frequency space, this means that all the information regarding the motion lies at the harmonics of the fundamental frequency. The remainder of the signal constitutes noise, and should be filtered out.

In order to filter the noise in frequency space, the fundamental frequency must be determined by performing FFT on each pixels data (Figure 72 A). The result is then filtered using a Weiner filter *F(s)*:

$$F(s)=\frac{D(s)}{D(s)+N(s)}\times D(s)$$

where *D(s)* is the FFT of the pixel data, *N(s)* is the noise spectra of the system and *F(s)* is the FFT of the filtered data. $N(s)$ is the FFT of the signal recorded when the cantilever is in contact with the resting sample. A peak with the lowest frequency and amplitude greater than a preset threshold (set at roughly twice the value of the noise) is chosen from each pixel's filtered data. The frequency of those peaks was found to be identical (1 KHz) and therefore determined as the fundamental frequency, f_0 (Figure 72 A inset). Now that the fundamental frequency is known a more precise set of noise-eliminating filters can be constructed. A series of Remez filters is created around each harmonic allowing the information relevant to the samples motion to be retained, and the noise eliminated. In theory, the motion could be represented by an infinite number of harmonics. In actuality, the signal is bandwidth limited by the cantilever, and the data acquisition hardware. If components of the samples motion are faster than one-half the data-acquisition sampling rate(f_S), aliasing of the data will occur. To prevent this, the data acquisition hardware must sample at greater than twice the resonant frequency of the cantilever, ensuring that high frequency components are low-pass filtered by the cantilever. In our case, we use a 1 KHz sine wave, which does not introduce components above the Nyquist frequency(N_Q), which is equal to $\frac{f_S}{2}$. Taken together, these requirements set an upper frequency limit on the data such that the highest harmonic cannot be greater than the Nyquist frequency. Within this frequency limitation, there are a finite number of points in frequency space that are located at $\left\{f_0, 2f_0, 3f_0 \ldots \operatorname{mod}\left(\frac{N_Q}{f_0}\right) f_0\right\}$ where the information pertaining to the pixels motion resides. Each pixels data stream is filtered by each of the $\operatorname{mod}\left(\frac{N_Q}{f_0}\right)$ Remez filters, and the results are summed together (Figure 72 C). The data is then transformed back into the time domain, resulting in a noise-filtered motion trace of the pixel (Figure 72 D).

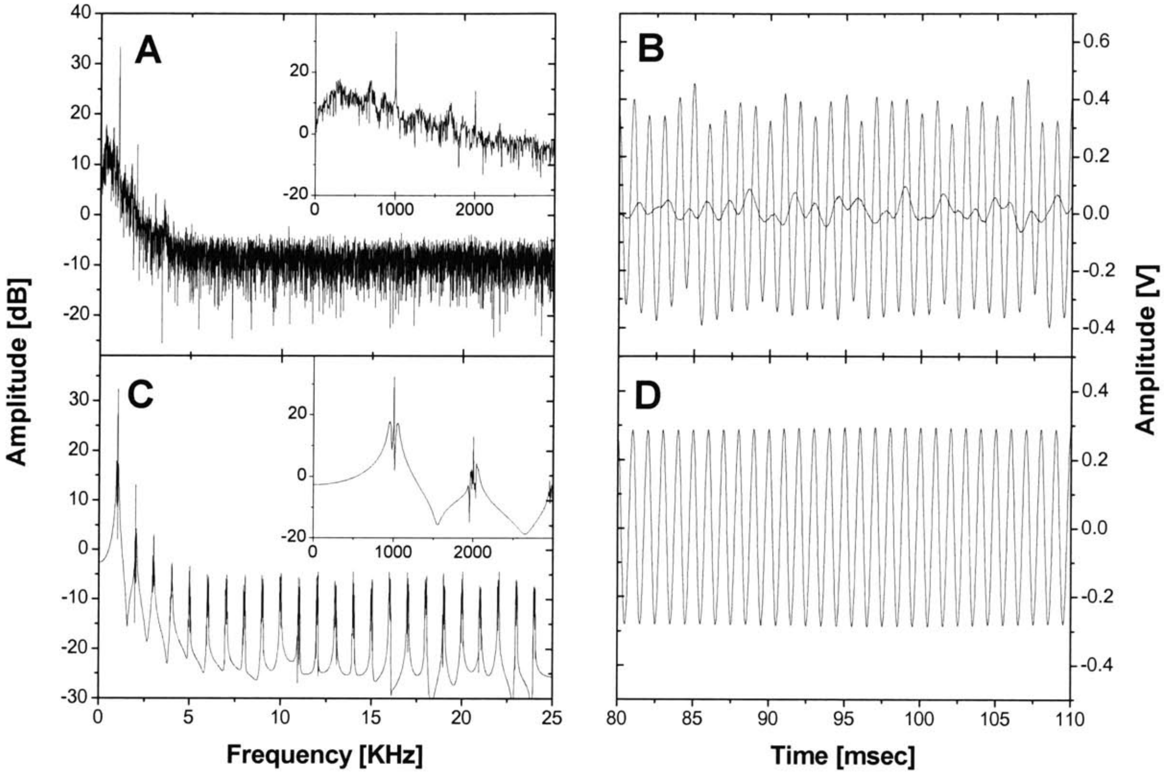

Figure 72: AFM Position Sensitive Diode: Signal Processing

The PSD signal from a single pixel in the frequency domain (A, C) and in the time domain (B, D). In our experimental setup, we are imaging a surface with a sinusoidal oscillation at 1 KHz. (A) The Fourier Transform of the raw signal. The fundamental frequency (1 KHz peak) and its first harmonics (2 KHz peaks) as well as peaks associated with noise can be clearly seen in the expanded graph (A insert). (B) The corresponding raw signal in the time domain showing the 1 KHz oscillation on top of the noise. Dashed line represents the background noise level. (C) The processed data following application of a Weiner filter and a Remez filters in the frequency domain. Since the motion information resided only at multiples of the fundamental frequency, any signal not at those frequencies is filtered out. (D) The corresponding time domain trace shows the elimination of the noise from the signal.

The third task is phase alignment of the pixels' motion. In the stroboscopic method, the system is reset before the cantilever is moved to a new position. This ensures that the motion of every pixel is in phase with one another. The key advantage of the continuous method is that no such reset is required. As a result, the motion of the pixels is completely out of phase (Figure 73 A), and a method to phase align the motion traces during post processing is necessary. The alignment of the pixels' motion traces is carried out in two stages: (a) a coarse alignment followed by (b) a refinement process. In the first stage, we utilize the knowledge that in a periodic system, any data points separated in time by an integral number of fundamental periods are in phase with each other. We therefore identify the earliest time point in each pixel trace which is separated from the first pixel's start time by an integral number of fundamental periods. The start of each pixels trace is shifted to those time points. This procedure may not always be possible because the sampling of data only occurs at discrete time points which may not coincide with an integral number of fundamental periods. To address this problem, the motion of each pixel is described as an equation consisting of a linear combination of sines and cosines. The parameters of the motion equations are generated by using a least-squares curve fit to the data of each pixel. With these parameters the pixels motion can be described at any time point, and the initial phase alignment procedure can be completed.

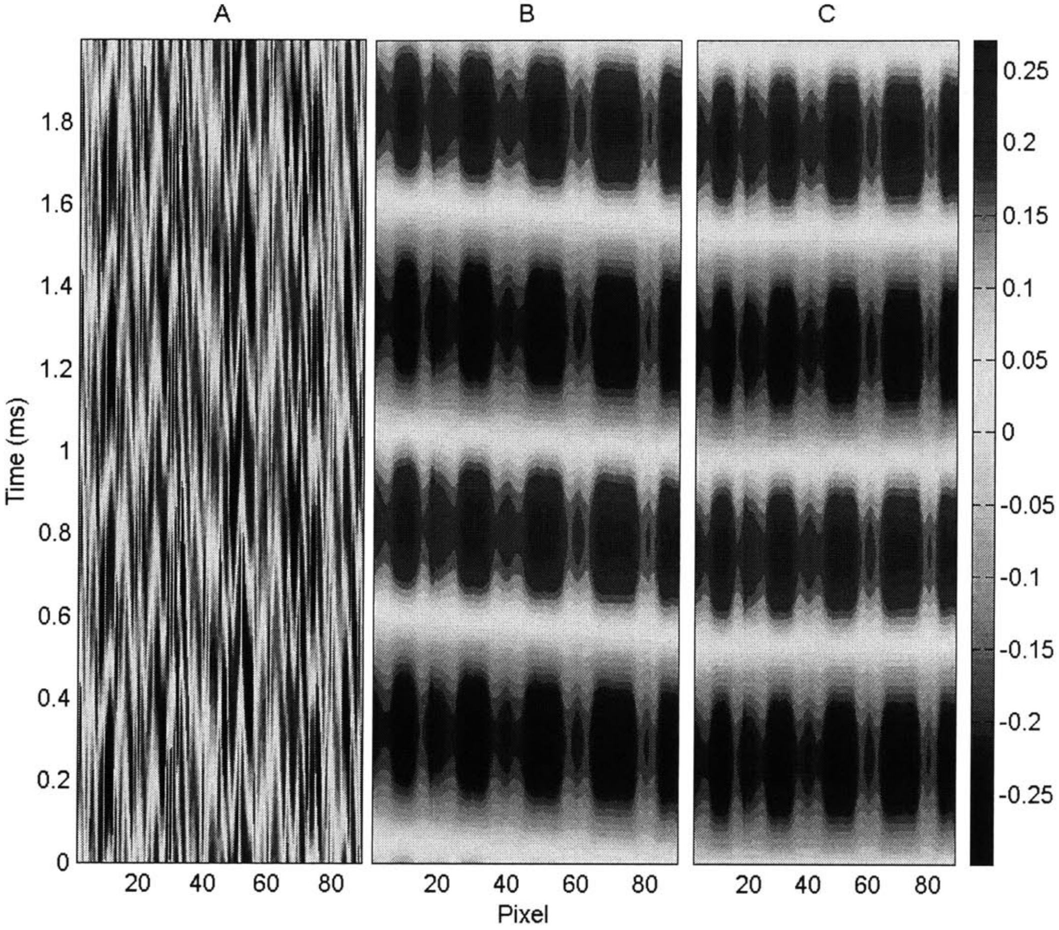

Figure 73: Phase Alignment of Data

The motion traces of all pixels plotted in contour maps. Two cycles of motion, spanning 4 milliseconds are shown. (A) Traces before phase alignment. (B) Traces after the course alignment process. A phase error that is linear with acquisition time remains. The maximum phase error occurs at the last pixel and is 5.5%. (C) Traces after application of the frame matching algorithm during the refinement process. The phase error is largely eliminated and the remaining error has an RMS value of 0.19%.

The first stage of the phase alignment described above highly depends on the accuracy of determining the fundamental frequency (and consequently the fundamental period). An error in the fundamental frequency (Δf_0) causes an error in phase proportional to the elapsed time $\left(\frac{\Delta f_0}{f_0} \times t_e\right)$, where t_e is the elapsed data acquisition time. This phase error becomes significant for large numbers of pixels (Figure 73 B), and appears as a traveling wave artifact superimposed over the motion of the sample.

The phase error is eliminated in the refinement stage of the alignment process (Figure 73 C). The goal is to select the frame in the reconstructed motion that corresponds to the DC image, and then introduce a complementary phase shift (proportional to t_e) to each pixel such that the selected frame matches with the DC image. The frame is selected by matching the first few pixels, which are not subject to large phase errors. The phase shift is introduced, and the least-squares difference between the selected frame and DC frame is computed. This process is repeated for various values of the phase shift, and the one with the smallest least-squared is selected. To evaluate this frame matching algorithm the phase error is calculated by comparing the time difference between the peak amplitude in each pixels sinusoidal motion with that of the first pixel. Following the rough alignment step, the phase shift grows linearly with time. Approximately 0.14% phase error per second, consequently producing a 5.5% phase error in the last pixel (data not shown). After the refinement process, the linear trend in the phase error is eliminated, and the RMS phase error is 0.19% (data not shown). With the phase error known, each pixels motion trace can be appropriately adjusted, and a 3-D matrix representing the samples motion as a function of time is constructed as in the stroboscopic method.

Conclusion

Atomic force microscopy is probably the only imaging tool that allows for visualization of topographical features in magnification range achieved by EM, but under physiological non-destructive conditions. Traditionally AFM imaging has been mostly restricted to topological features due to poor temporal resolution. However, if the resolution of AFM could be coupled with sufficiently high time resolution, this would present an important advance for imaging rapid structure dynamics in high resolution. Previous effort to image motion with AFM has focused on rastering the cantilever over the sample as rapidly as possible. The time resolution of this rapid-scan technique is limited by the scanning speed and area of the AFM. Presently, the time resolution of the rapid scan is on the order of few tens of milliseconds at best.

In this work we have presented step-scan time resolved AFM, a novel technique for micro-second imaging of periodic motion using commercial AFM operating in contact mode. By imaging periodic motion, the complete vertical motion of the sample at each point was recorded, and the movement of the entire sample surface was reconstructed by arraying together the individual motion traces. To illustrate this, we have imaged the motion of microfabricated calibration grid at 10 nm lateral resolution and microsecond temporal resolution. Two variations of step-scan time resolved AFM were presented: (1) the stroboscopic method which requires a sample whose motion is periodic and can be externally triggered, and (2) the continuous method which only requires a sample whose motion is periodic. The time resolution of the step-scan time resolved AFM is limited by the resonance frequency of the AFM probe and the data acquisition electronics. When the data acquisition setup can sample the data at a sufficient rate (at least double the resonance frequency of the probe) the latter can be eliminated. For this study a cantilever with resonance frequency of ~300 KHz and ~80 KHz were used to image the motion of the grid using the stroboscopic and continuous modes respectively. With this setup a time resolutions of ~3 and 40 μsec were achieved in the stroboscopic and continuous methods respectively. (Note that the time resolution of the continuous method was limited by our relatively slow acquisition card and could be reduced to ~3 μsec by using a higher speed data acquisition card.) Lateral resolution is determined primarily by the step size as well as the sample properties. One of the strength of this technique is its extremely high vertical resolution. By imaging the motion of the sample over many cycles, noise can be removed, allowing detection at the threshold of vertical motion with sub-angstrom amplitude.

The step-scan time resolved AFM opens the door for imaging rapid periodic motion of various systems. We demonstrated that the technique can visualize motions of micro-electromechanical systems (MEMS). In addition, future progress in nanotechnology is likely to produce nano-motor devices. Imaging these nano-motor structures performances will be possible with this novel technique. We anticipate, however, that step-scan time resolved AFM will have the most significant impact on the study of biological systems. We have for the first time the potential to image rapid biological processes as they occur in real time under physiological conditions with an unprecedented combination of lateral and temporal resolutions. We realize however, that some biological samples could be damaged by the contact time with the AFM probe. This contact time is significantly longer in the step-scan method than regular contact mode scanning. To reduce the possibility for sample damage, our current efforts are focused on the implementation of tapping mode AFM into our step-scan time-resolved technique.

References

Ando, T., N. Kodera, et al. (2003). "A high-speed atomic force microscope for studying biological macromolecules in action." Chem Phys Chem 4(11): 1196-202.

Ando, T., N. Kodera, et al. (2001). "A high-speed atomic force microscope for studying biological macromolecules." Proc Natl Acad Sci U S A 98(22): 12468-72.

Binnig, G., C. F. Quate, et al. (1986). "Atomic force microscope." Phys. Rev. Letts. 56: 930-933.

Goldsbury, C., J. Kistler, et al. (1999). "Watching amyloid fibrils grow by time-lapse atomic force microscopy." J Mol Biol 285: 33-39.

Guthold, M., M. Bezanilla, et al. (1994). "Following the assembly of RNA polymerase-DNA complexes in aqueous solutions with the scanning force microscope." Proc Natl Acad Sci USA 91: 12927-12931.

Haga, H., M. Nagayamam, et al. (2000). "Time-lapse viscoelastic imaging of living fibroblasts using force modulation mode in AFM." J Electron Microsc 49: 473-481.

Malkin, A. J., Y. G. Kuznetsov, et al. (1996). "Incorporation of microcrystals by growing protein and virus crystals." Proteins 24: 247-252.

Radmacher, M., M. Fritz, et al. (1994). "Direct observation of enzyme activity with the atomic force microscope." Science 265(5178): 1577-9.

Rousso, I., E. Khachatryan, et al. (1997). "Microsecond atomic force sensing of protein conformational dynamics: implications for the primary light-induced events in bacteriorhodopsin." Proc Natl Acad Sci U S A 94: 7937-7341.

Rousso, I., E. Khatchatryan, et al. (1997). "Atomic Force Sensing of Light-Induced Protein Dynamics with Microsecond Time Resolution in Bacteriorhodopsin and Photosynthetic Reaction Centers." J Struct Biol 119: 158-164.

Rousso, M. A. a. I. (2005). "Atomic force microscopy with time resolution of microseconds." Applied Physics Letters 86.

Schoenenberger, C. A. and J. H. Hoh (1994). "Slow cellular dynamics in MDCK and R5 cells monitored by time-lapse atomic force microscopy." Biophys. J. 67: 929-936.

Stoffler, D., K. N. Goldie, et al. (1999). "Calcium-mediated structural changes of native nuclear pore complexes monitored by time-lapse atomic force microscopy." J Mol Biol 287: 741-752.

Stolz, M., Stofflerm D, et al. (2000). "Monitoring biomolecular interactions by time-lapse atomic force microscopy." J Struct Biol 131: 171-180.

Ushiki, T., J. Hitomi, et al. (1999). "Imaging of living cultured cells of an epithelial nature by atomic force microscopy." Arch Histol Cytol 62: 47-55.